NASA Technical Memorandum 101531

WIND TUNNEL PRESSURE STUDY AND EULER CODE VALIDATION OF A MISSILE CONFIGURATION WITH 77° SWEPT DELTA WINGS AT SUPERSONIC SPEEDS

PATSY S. FULTON

NOVEMBER 1988

National Aeronautics and Space Administration

Langley Research Center
Hampton, Virginia 23665

ABSTRACT

An investigation has been conducted in the Unitary Plan Wind Tunnel at NASA Langley Research Center to gather experimental data for use in analyzing the different experimental wing-body effects and assessing the computational accuracy of the Zonal Euler Solver (ZEUS) code. The wind tunnel study was initiated to provide pressure and flow visualization data to be used in the analysis. The model is a simple, ogive cylinder body/fin configuration with three physical sets of interchangeable fins. These fins can be mounted in a high, mid, or low monoplanar arrangement, as well as in a "v" arrangement.

The model is equipped with pressure orifices at three constant longitudinal stations to match the output format of the ZEUS code. Each station has orifices completely around the body and on both upper and lower surfaces of the fins. Internally mounted pressure transducers are used to reduce lag-time problems in the data acquisition process. The tests were conducted at Mach numbers from 1.70 to 2.86 and angles-of-attack from -4^{o} to 24^{o} in increments of 4^{o}. Vapor screen photographs were taken to observe the effect of the different wing-body combinations on the vortex structure.

The ZEUS code is a supersonic space-marching Euler code with relaxed geometry restrictions compared to earlier codes and is used to predict the aerodynamics of supersonic missile configurations. The relaxed geometry restrictions allow solutions for missiles on which the fins do not extend radially from the body centerline. The experimental data and the comparison between the wind tunnel data and the computational data are examined and discussed.

TABLE OF CONTENTS

TABLE OF CONTENTS (cont.)

LIST OF FIGURES

Page

List of Symbols

C_0 - zero coefficient, psf

C_1 - sensitivity coefficient, psf/volt

C_2 - nonlinearity coefficient, psf/volt^2

C_p - coefficient of pressure

$\tilde{E},\tilde{F},\tilde{G},\tilde{U}$ - flux vectors

h - enthalpy

M - Mach number

p - pressure, psf

q - dynamic pressure, psf

S - wing semispan at the trailing edge, inches

u, v, w - velocity components, non-dimensional

V - gage output for a certain channel, volt

Y - spanwise location on the wing, inches

Subscripts

o - stagnation

∞ - free-stream

Greek Symbols

α - angle-of-attack, degrees

β - roll angle, degrees

ρ - density, slugs/ft^3

Θ - circumferential angle around the body, degrees

s, v, τ - physical coordinates

ε, η, ζ - computational coordinates

CHAPTER I

INTRODUCTION

Recent advances in computational fluid dynamics (CFD) have led to the development of computer codes which have been specialized to predict the aerodynamics of supersonic missile configurations. The Naval Surface Weapons Center has developed two such codes, the Supersonic Wing Inlet Tail (SWINT) code and the Zonal Euler Solver (ZEUS) code, which solve the Euler equations for tactical missile configurations at supersonic speeds.

SWINT was developed in 1981 and can be used only with missiles having fins which extend radially from the body centerline, i.e., the plane of the fins must lie on the body centerline. Yet, many of today's actual missiles have fins which do not extend from the body axis. Although the SWINT code provides fairly accurate solutions, the code is difficult to run, especially at the low supersonic Mach numbers. Experience with SWINT over the past seven years has shown that the code has two major weaknesses: lack of robustness and restrictive geometry (Refs. 1 and 2).

ZEUS was developed to provide more relaxed geometry restrictions and more robustness to overcome the weaknesses of SWINT. ZEUS is capable of solving the flowfields about missiles with fins which can lie either on or off the body axis. Since the ZEUS code has just recently become available, experimental verification is needed.

A motivation for the current experimental and computational study came from an earlier study which involved comparisons between experimental pressure data and SWINT calculations (Ref. 3). In this reference a D-shaped body concept, with two low mounted wings and two high mounted tails, is introduced. The tail fins extended along radial lines from the body center, but the wings did not. Therefore, modifications had to be made in the

body geometry before the SWINT program could be run. This initiated the realization that a code with less restrictive geometry was needed.

A wind tunnel study was initiated and conducted to provide experimental surface pressure and flow visualization data in order to assess the computational accuracy of these codes. The basic geometry of the model used in the study is similar to a previously tested force model (Ref. 4). The model was also designed so that the experimental data would be in a form which is easily comparable with the computational results. The model is a simple, ogive cylinder body with three sets of interchangeable fins. The three sets of fins can be used to produce seven different configurations: the high-, intermediate high-, mid-, intermediate low-, and the low-wing orientations, as well as a "v" arrangement which, when rolled 180^{o}, produces the seventh configuration. These last two configurations are hereafter referred to as the bent-wing and the inverted bent-wing configurations, respectively. Cross section sketches of these configurations are shown in Figure 1. A body-alone configuration (i.e., one with no fins mounted on the body) was also tested. All eight missile configurations which were tested are shown in Figure 2. The model contains approximately 110 pressure orifices, depending on the configuration, which are located at three constant longitudinal stations both around the body and on the upper and lower fin surfaces. The tests were conducted at Mach numbers from 1.70 to 2.86 at angles-of-attack from -4^{o} to 24^{o} in increments of 4^{o}. The mid-wing configuration was rolled $+30^{o}$, $+60^{o}$, $+90^{o}$, $+180^{o}$, -30^{o}, -60^{o}, and -90^{o}. Flow visualization by the vapor screen method was used in this study in order to better analyze the pressure data.

The theoretical investigation involved obtaining pressure calculations from the SWINT and ZEUS codes. The SWINT code was used to predict the flowfield for the mid-, bent-, and inverted bent-wing configurations (on-axis

configurations). The ZEUS code was used to predict the flowfield for the intermediate low-, low-, intermediate high-, and high-wing configurations (off-axis configurations). The two codes were run for Mach numbers of 1.70, 2.16, 2.40, and 2.86 and for angles-of-attack of 0^{o}, 8^{o}, 16^{o}, and 20^{o}. Only the ZEUS results are discussed in this report since the off-axis configurations are of the main interest for the experimental/theoretical comparisons.

The next two sections of this text explain the experimental and computational procedures which were applied for this investigation. The experimental procedures section gives a description of the model, the instrumentation, and the general test techniques used for the wind tunnel test. The computational procedures section briefly discusses the two codes, SWINT and ZEUS.

The analysis of the data in this investigation is presented in three phases. First, the wind tunnel data are analyzed to investigate the effects of wing location on the experimental surface pressure distributions. Second, the vapor screen photographs are analyzed and various flow phenomena are discussed. Finally, comparisons are made between the pressures from the SWINT and ZEUS codes and the experimental data to investigate the computational accuracy of the codes.

CHAPTER II

EXPERIMENTAL TECHNIQUES

1. Wind Tunnel

The experimental tests were conducted in the low Mach number test section of the Langley Unitary Plan Wind Tunnel (UPWT). The facility originated from a Congress-approved plan, the Unitary Wind Tunnel Plan Act of 1949. The purpose of this plan was to provide funding for various facilities around the country in order to develop advanced airplanes and missiles (Ref. 5). A historical perspective on this tunnel can be found in Reference 6.

The tunnel is a variable-pressure, continuous-flow facility with axisymmetric sliding-block nozzles leading to one of two test sections which have a range of Mach numbers from 1.47 to 4.63. The low speed test section has a Mach number variation from 1.47 to 2.90. The test section is 4 ft by 4 ft by 7 ft and is formed by the downstream section of the nozzle. Figure 3 shows a diagram of the facility and Reference 5 provides a more detailed description of the tunnel. Table I gives more details on the tunnel operating parameters for this test.

2. Model

The model consists of a circular cylindrical fuselage with an ogive nose and with 77^{o} delta wings which can be mounted in various locations on the fuselage. The model is 33.8 in. long with a wing span of 9.64 in. and a body radius of 1.3 in. A complete view of the missile dimensions is shown in Figure 4. This pressure model was designed to be complimentary to the force and moment model tested in Reference 4, and therefore had the same basic dimensions as the aforementioned force model. Also, the Mach numbers and angles-of-attack were duplicated, as much as possible, from the previously tested force model. In this manner, both pressure and force data would be

available for the same geometry and flow conditions. The tail fins which were used in the force tests are eliminated from the pressure model since they are not needed for the pressure test objectives. Other major differences between the force model and the pressure model are the wing locations. The force model was designed so that its wings were always in the mid-wing position (as defined in Fig. 1), but the wings could be positioned forward and aft of this center position. The pressure model was designed so that its wings could be mounted both on and off the body axis, but only in the center position.

The pressure model is made mostly of stainless steel.with the nose and some of the minor filler plates constructed from aluminum. The stainless steel adaptor and sting are specially designed so the model can be stably mounted and supported in the test section.

As can be seen in Figure 1, the high-, intermediate high-, low-, and intermediate low-wing configurations consist of wings which do not extend radially to the body centerline, while the mid-, bent-, and inverted bent-wing, configurations have wings which do lie on the body axis. The low-, intermediate low-, and inverted bent-wing conditions are achieved by a 180^{o} roll of the high-, intermediate high-, and bent-wing configurations, respectively. Only three different physical wings are used to achieve all seven configurations.

The bent-wing configuration contains 106 pressure orifices, the mid-, and low-wing configurations contain 114 orifices, the high-wing configuration contains 110 orifices, and the body alone contains 72 orifices. Note that the respective roll cases of these configurations will also have the same number of orifices. The various plates and wings used for the configurations are shown in Figure 5.

The large number of pressure orifices and the small radius of the body created numerous problems. The pressure transducers, which are discussed in greater detail in the following section, were mounted inside the model. The plastic tubing connecting the pressure orifices to the transducers was especially susceptible to getting cut or pinched off due mainly to the large number of tubes which had to be connected. To help alleviate this problem, the tubing was cut as short as possible. The mid-wing configuration was especially difficult to assemble because the wing is mounted directly above the pressure modules, leaving little room for the tubing. Even after the tubing was shortened, the wing did not fit and part of the inner base of the fuselage was machined off to add more room.

The drilled pressure orifices are 0.026 in. diameter and the stainless steel tube connections are 0.042 in. diameter. As mentioned before, the model has pressure orifices at three longitudinal stations. These stations are situated 18.2 in., 23.4 in., and 27.56 in. from the tip of the nose (Fig. 4). These locations are referred to as either forward, middle, and aft, or stations 1, 2, 3, respectively. The orifice stations are located at approximately 50%, 75%, and 95% of the maximum hypothetical wing root chord that is obtained by extending the delta wing leading and trailing edges to the body centerline (Fig. 6). Only the maximum hypothetical root chord is shown in this previous figure because the root chord changes from configuration to configuration. The body pressure orifices are spaced every 15^{o} around the model, and are normal to and flush with the surface of the model.

The orifices on the wing are flush with the wing surface and are aligned in such a manner that they lie along constant rays going from the forward to the aft position. These orifice locations and the slope of the rays are given in Table II and illustrated in Figure 7. With the model at 0^{o} roll and

looking downstream, pressure orifices are located on the upper surface of the right wing and the lower surface of the left wing. This placement of the orifices allows for full coverage of both the windward and leeward side pressures on the wings.

The wing is beveled so that the leading edge wedge angle is 10^{o}, as shown in the diagram below. The bevel is on the side of the wing opposite to the pressure orifices. The wing is flat on the side with the orifices in order to simulate a thin wing. The purpose of the bevel is to create a sharp leading edge, to provide strength to the structure, and also to add some thickness to allow room for the pressure tubing. Plastic tubing, 0.040 in. diameter, connects the pressure transducers to the metal tube connectors on the model.

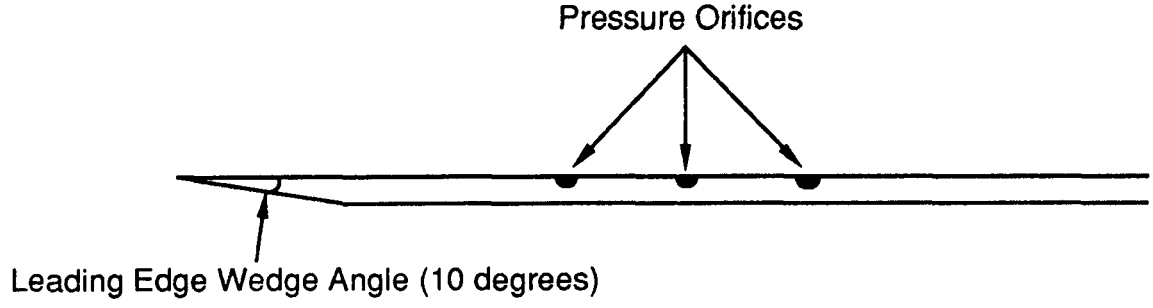

3. Instrumentation

Pressure Transducers

Three 48-port electronically scanned pressure (ESP) modules were internally mounted and were used to obtain the pressure readings. Normally, the pressure gages are located outside the test section, but the internally mounted gages were used here to reduce the lag time. The slimline version of the transducer was used for this test because of the crucial need for more space, especially for the plastic tubing. The dimensions for this rectangularly

shaped scanner are 2.70 in. long, 1.15 in. wide, and with a height of 1.20 in. The height of the regular scanner is 1.45 in., whereas the other dimensions are the same as the slimline scanner. The pressure range is $\pm$5.00 psid. The operating temperature range is from 0^{o} F to 175^{o} F. Since the tunnel temperature was held at 125^{o} F for the entire wind tunnel pressure experiment, the transducers were always well within their operating range. The static error band for the module is $\pm$0.15% FS, where FS is the full-scale value of the gage. Thus, since a $\pm$5 psid gage is used, the static error band is $\pm$0.008 psi.

To acquire the data, the voltage is electronically scanned and the pressure is calculated by the following equation:

$$p = C_0 + C_1 V + C_2 V^2 \qquad (1)$$

where C_0 = zero coefficient

C_1 = sensitivity coefficient

C_2 = nonlinearity coefficient

V = gage output voltage for a certain channel

The accuracy of these pressure modules is maintained through periodic on-line calibrations. Calibrations consist of pneumatically switching the sensor calibrate head into the calibrate position and then applying three or more calibrate pressures while measuring the electrical response of each transducer within the sensor module.

The frequency of calibration depends on ambient temperature changes and electrical drift of the transducers. For this test, calibrations were made for every run, where each run consisted of a particular configuration at one Mach number and the range of angles-of-attack from -4^{o} to 24^{o}.

Angle-of-Attack Sensor

A Qflex accelerometer was used to measure the angle-of-attack for the model. The angle-of-attack sensor has a cylindrical shape with a base diameter of 1.188 in. and a length of 1.625 in. The sensor consists of a 9 pin connector with a 5 in. long cable (Fig. 8). The angle-of-attack system was mounted on an aluminum plate and placed in the nose of the model.

The Qflex accelerometer is based on a mass deflection system where the mass is deflected a certain amount dependent on the angle-of-attack. The sensor responds almost instantaneously (within milliseconds) to a change in the angle-of-attack.

The accuracy of the system under reasonable tunnel conditions is within a few hundredths of a degree. Two major causes of error are sting whip and tunnel vibration. Whenever sting whip occurs, the inertial effects are sensed by the accelerometer and faulty readings can occur. The occurrence of tunnel vibration is hard to predict because it is an intermittent problem and varies in severity from one tunnel to another. When the tunnel vibrates at certain frequencies, a DC offset occurs in the accelerometer which in turn causes the accelerometer to give false readings. Neither of the two problems are residual; in other words, once normal flow conditions are achieved or once the vibrational frequency changes, the accelerometer should give the correct reading again. Tunnel vibration was never a problem during this test. Furthermore, the UPWT does not have a history of tunnel vibration. The sting whip problem occurred a few times when the tunnel unstarted (i.e., the flow changed from supersonic to subsonic), but the angle-of-attack was never read until normal flow conditions were achieved.

4. Test Procedures

The angle-of-attack sensor and the pressure transducers were installed inside the fuselage. An electric circuit board connecting the ESP gages and the accelerometer to the data acquisition system was inserted in the model with cables running through the sting and out the test section. This is how the data were electronically transmitted from the pressure transducers to the computer and finally, to the terminal screens in the data acquisition room.

Once the pressure tubing was connected from the transducer to the model, a leak check was performed. This consisted of applying a vacuum to each orifice to determine if the tubing was pinched off or leaking. If the orifice was able to maintain a vacuum for several seconds, the orifice was considered to be a good one. If the orifice did not read a vacuum, it was considered to be plugged; and if the orifice went to vacuum but then increased at rates greater than about 2-3 psf/second, the orifice was leaking and was considered to be unusable. After a satisfactory leak check was obtained (i.e., if no more than 5% of the orifices were plugged and/or leaking), the model sections were bolted together.

Transition strips were used in order to trip the boundary layer from laminar to turbulent flow. These transition strips consisted of No. 50 sand grains (0.0128 in,) sprinkled in acrylic plastic. These strips were 0.062 in. wide and were located 1.20 in. aft of the nose and 0.40 in. aft of the leading edges measured streamwise on both sides of the wing surfaces. The location and size of the grit was determined from References 4 and 7. For more details on boundary layer transition, References 8-10 are available.

After the transition strip was applied, the ESP gages were calibrated. Three pressure ports on each of the 48-port modules were chosen to measure three known pressures which were measured using precision mercury

manometers and recorded for every data point. Thus, the gages could be checked on every data scan. Vacuum pumps are used to pull the reference side of the ESP's down to a hard vacuum (<2 psfa). In this manner, the differential pressure transducers can be operated as absolute pressure gages since the reference pressure has been set at zero. After this low reference pressure is set, the ESP modules are calibrated.

Before each run, the tunnel pressure was set for at least two low pressures (i.e., 700 psfa and 300 psfa) and a data point was recorded in order to allow a check for every port. With the wind on, the three known ports were checked to verify that the transducers were working properly.

For the angle-of-attack sensor, angles are set at -15^{o}, -10^{o}, -5^{o}, 0^{o}, 5^{o}, 10^{o}, 15^{o}, 20^{o}, 25^{o}, and 30^{o} using a large inclinometer, and then raw microvolt readings are made. The sensitivity, bias, and zero values are calculated using a least-square curve fit and these values are used to solve for the angle-of-attack which is denoted by Angle in the following equation:

$$\text{Angle(deg)} = \text{Arcsin}((\text{Reading}(\mu v) - \text{Bias}(\mu v))/\text{Sens.}(\mu v/g)) - \text{Zero(deg)} \quad (2)$$

where deg = degree

μv = microvolt

g = acceleration due to gravity

Reading = the value read by the accelerometer

The heart of the data acquisition system is the MODCOMP 32/85 central processing unit (CPU). This unit has 2 megabytes (MB) of memory and 256 MB of disk storage. When internally mounted ESP gages are used, the system is capable of making 10 samples/second. The system can display up to four 48-port ESP modules (192 raw microvolts (μv) or 192 psfa) and refresh the pressure values about every second. The data are scanned and displayed continuously both as microvolts and also in engineering units. The system

computes the pressures (psfa) from raw counts. The data are stored on magnetic tape and also on disk. Both the microvolt and the engineering unit data are listed on a 1200 line-per-minute printer for every point taken, where a point consists of one configuration at a specific Mach number and a specific angle-of-attack. The free-stream quantities (Mach number, static pressure, dynamic pressure, stagnation temperature, and Reynolds number/ft) are computed and the coefficient of pressure, C_p, is found, where:

$$C_p = (p - p_\infty) / q_\infty \qquad (3)$$

where p = pressure reading at each port

p_∞ = free-stream static pressure

q_∞ = free-stream dynamic pressure

The angle-of-attack is computed also and all of these values are listed and stored on magnetic tape.

After running through the range of Mach numbers and angles-of-attack, a configuration change was made while leaving the model in the test section. Thus, the fuselage did not have to be remounted on the sting for every change. The test procedures were then repeated.

Based upon calibrations and repeatability of data, an estimation of the accuracy of the various measured quantities within the following limits is given below:

α to within ± 0.10 deg

M to within ± 0.015

Also, based on repeatability of data and taking into account the accuracy of the quantities above, the estimated accuracy for the ±5 psia ESP gages is 2-3 psfa. Table III shows the range of accuracy for the coefficients of pressure at the different Mach numbers.

5. Flow Visualization by the Vapor Screen Method

Flow visualization data were obtained by a vapor screen method as described in Reference 11. The vapor screen photographs were used to acquire information about the flowfield mainly on the leeside of the wing. The basic principles involved in the vapor screen techniques are as follows. Initially, water is injected into the tunnel flow. This water condenses and possibly develops ice crystals to form a uniform fog. The fog is then illuminated by a narrow band of light which is projected perpendicular to the free-stream flow. The presence of the model changes the distribution of the uniform fog, and thus, the light scattering pattern is altered. As a result of a combination of centrifugal forces, thermodynamic effects, and density variations, a pattern of flow characteristics such as shocks and vortices can be observed. Regions where the ice particles have either melted or been cast aside will be dark on the vapor screen photograph.

In order to obtain the intense beam of light of narrow width (about a quarter of an inch) necessary for good vapor screens, two 1,000-W mercury vapor lamps were used. Also, a 1.5 in. diameter parallax lens and a knife edge were used to help achieve the proper width and intensity of the light.

A remote controlled 70 mm camera with automatic advance and an 80 mm lens was mounted inside the test section above and behind the model. This allowed for a view of the flow pattern in a plane normal to the free-stream flow. The camera could have been mounted outside the test section for a view of the overall flowfield, but the inside-mounted camera was chosen to obtain more accurate measurements of the vortices and shocks. The camera contains enough film for about 70 photographs. A schematic drawing of the vapor screen set-up is shown in Figure 9 and a vapor screen photograph is shown in Figure 10.

The vapor screen tests were conducted in a similar manner as the other wind tunnel tests previously discussed, except that water was added downstream of the test section to produce the vapor. The vapor screen tests are performed separately from the pressure tests because the condensation effects tend to reduce the stagnation pressure by about 5%, increase the static pressure by 4%, and reduce the Mach number by about 0.05. These changes in free-stream conditions affect the pressure data, but should not affect the interpretation of the vapor screen photographs. The location of the water injection system is shown in Figure 3. All of the instrumentation inside the model was removed, except for the angle-of-attack sensor. This was done since the pressure tests had been completed and the instrumentation was no longer needed. Also, removing the instrumentation prevented unnecessary exposure to moisture. The model was painted with a flat black acrylic paint in order to reduce the glare from the model, and white dots were painted on the three longitudinal stations where the pressure orifices were located to provide a reference point for alignment. Grit was added in the same manner as discussed before in order to insure transition from a laminar to a turbulent boundary layer. These tests were conducted at Mach numbers of 1.70, 2.16, 2.40, and 2.86 and angles-of-attack of 12^{o} and 20^{o} for each of the seven configurations, plus the body-alone configuration (i.e., the body with no fins). The mid-wing configuration was also rolled -60^{o}, -30^{o}, $+30^{o}$, and $+60^{o}$ and tested at the Mach numbers and angles-of-attack listed above. Photographs were taken at the three longitudinal stations where the pressure orifices were located, except for the body-alone configuration in which data were taken only at the forward and aft stations.

Chapter III

COMPUTATIONAL PROCEDURES

The computational data was acquired through the use of two different Euler codes, the Supersonic Wing Inlet Tail (SWINT) code and the Zonal Euler Solver (ZEUS) code. One of the purposes of this thesis project was to obtain experimental data to investigate the validity of the ZEUS code using configurations with off-axis fins. For this missile study, the SWINT code was run using the geometry for the configurations with fins which were on the body axis (i.e., the mid-, bent-, and inverted bent-wing configurations). Since calculations from the SWINT and ZEUS codes on missile geometries with the more traditional on-axis fins already exists (Refs. 2, 3, and 12), only the calculations from the ZEUS code using the off-axis missile geometries are presented in this paper. Thus, the reasons for even using the SWINT code in this paper were to obtain data for the on-axis fins, to explain briefly some of the differences between SWINT and the newer ZEUS code, and to see how these differences affect the geometry restrictions and robustness of ZEUS.

As mentioned previously, the geometry restrictions inherent in the SWINT code do not allow the code to test missile cases whose fins do not lie on the body axis. Also, experimental data with off-axis fins for the purpose of code validation did not exist. With the wind tunnel data from the experimental investigation of this project and the calculations generated by ZEUS, a means of comparison between experimental and theoretical pressure data for off-axis fins now exists. The next few sections of this chapter briefly describe the SWINT and ZEUS codes and explain how they were applied in this investigation.

1. The SWINT Code

The SWINT code was developed to calculate the aerodynamics of tactical missile configurations at supersonic speeds. Most of the following discussion

is taken from Reference 13. SWINT is a space-marching Euler code which uses the body and bow shock as boundaries. The flow quantities in the region between the body and the shock are solved using the Euler equations written in non-conservation form as follows:

$$\frac{\delta \tilde{U}}{\delta \tau} + \frac{\delta \tilde{F}}{\delta s} + \frac{\delta \tilde{G}}{\delta \upsilon} = \tilde{E} \tag{4}$$

$$\begin{aligned} \tilde{U} &= r^1(\rho w, p+\rho w^2, \rho uw, \rho vw) \\ \tilde{F} &= r^1(\rho u, \rho uw, p+\rho u^2, \rho uv) \\ \tilde{G} &= (\rho v, \rho vw, \rho vu, p+\rho v^2) \\ \tilde{E} &= 1\,(0, 0, p+\rho v^2, -\rho uv) \end{aligned} \tag{5}$$

where: $\left.\begin{matrix} \tau = z \\ s = r \\ \upsilon = \phi \end{matrix}\right\}$ cylindrical coordinates

Also, the energy equation for steady, inviscid flow is given by:

$$h + \frac{1}{2}(u^2 + v^2 + w^2) = h_\infty + \frac{1}{2}(u_\infty^2 + v_\infty^2 + w_\infty^2) = \text{const.} = H_o \tag{6}$$

These equations are transformed from physical coordinates (s,υ,τ) to computational coordinates (X, Y, Z). SWINT uses a single conformal transformation to map the crossflow plane onto the computational domain (Fig. 11). The body and the fin geometries are treated separately so the need for complicated transformations is eliminated. The cylindrical coordinate

system is shown in Figure 12. After the transformations, the Euler equations are then solved and advanced by integrating the MacCormack predictor-corrector scheme which is shown below:

$$U^{*}_{n,m} = -\left(\frac{F^{k}_{n+I,m} - F^{k}_{n+I-1,m}}{\Delta x}\right)\Delta z - \left(\frac{G^{k}_{n,m+J} - G^{k}_{n,m+J-1}}{\Delta y}\right)\Delta z + E^{k}_{n,m}\Delta z + U^{k}_{n,m} \qquad (7)$$

$$U^{k+1}_{n,m} = \frac{1}{2}\left[U^{k}_{n,m} + U^{*}_{n,m} - \left(\frac{F^{*}_{n+1-I,m} - F^{*}_{n-I,m}}{\Delta x}\right)\Delta z - \left(\frac{G^{*}_{n,m+1-J} - G^{*}_{n,m-J}}{\Delta y}\right)\Delta z + E^{*}_{n,m}\Delta z\right] \qquad (8)$$

The MacCormack scheme uses finite-differencing to solve for the flow quantities and generate the grid. The shock location is found by solving the Rankine-Hugoniot equations.

The code has various restrictions placed on the configuration geometries (Ref. 13). These include:

1. The body alone must be single-valued in Θ.
2. Fins must be fairly thin and lie on constant Θ planes. (This requirement forces the fins to lie radially on the body centerline.)
3. Only fins with sharp edges can be used, and the fin location must be either single or double valued in z.
4. The fins cannot extend through the bow shock.

Another limitation of the code is that the flowfield must remain supersonic throughout the entire calculation.

The user must supply a description of the geometry and an initial flowfield near the missile's nose tip. For each configuration, a calculation was attempted for Mach numbers of 1.70, 2.16, 2.40 and 2.86 and at angles-of-attack of 0^{o}, 8^{o}, 16^{o}, and 20^{o}. Marching codes, such as SWINT and ZEUS, must have an initial flowfield prescribed to begin marching in space. A separate starting flowfield was included in the SWINT user manual (Ref. 13), but was not part of the SWINT code itself. This procedure made conical flow approximations at some initial z location near the nose tip. The inputs needed for the starting case include: the number of mesh points in the radial direction, the number of mesh points in the circumferential direction, the Mach number, the angle-of-attack, and the maximum circumferential distance around the body. Other variable quantities (ZS, ZC, B(1)) which must be specified by the user are illustrated below:

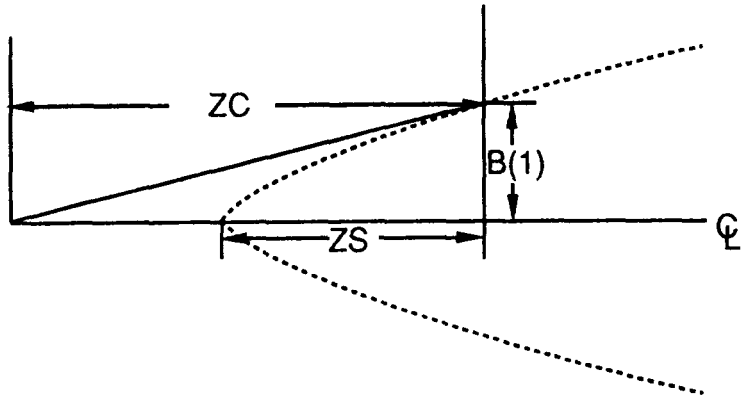

The output from the starting case can then be used as the initial flowfield to calculate the rest of the body using the SWINT code. Some of the important inputs which the user must specify include: z location where a run

terminates, CFL safety factor, new number of radial mesh points, new number of circumferential mesh points, number of fins, location of fin planes (in degrees) and the storage for differencing options for points adjacent to the wing tips.

The SWINT calculations were carried out in several stages after the starting solution was obtained. The first stage was fairly simple and merely involved ending the calculation just upstream of the fin. The other stages of the calculation varied in difficulty depending on the Mach number and the angle-of-attack of the run. These other stages covered the body downstream of the end of the first stage and the fin surfaces. For the first stage, the inputs in the previous paragraph were specified. These inputs remained the same for every run, where runs were made for all of the angles-of-attack and the Mach numbers. The following stages were more complex because the fins had to be taken into account. The appropriate fin geometry (either mid-, bent-, or inverted bent-wing geometry) was inserted in the code and initially the inputs were changed so the run was made to the end of the body. The angular location of the fins around the body was determined and specified for the mid-, bent-, or inverted bent-wing configurations, respectively. This angular fin location did not need to be specified in the first stage because there were no fins located in the region being calculated. If the code was unable to run to the end of the body, the number of radial mesh points was reduced and another run was attempted. The step size and the storage inputs were also varied. Often the code would march several inches down the body and then terminate. When this premature termination occurred, the flowfield plane just before termination would be saved. Then the inputs were systematically varied and another run was attempted. This procedure was repeated until the end of the missile body was reached.

The SWINT code had difficulty for configurations at the lower Mach numbers (1.70 and 2.16) at the higher angles-of-attack (16^{o} and 20^{o}). The code was encountering subsonic flow usually at the leading or trailing edges of the fins. The code uses special procedures (Ref. 14) at the fin edges which may induce artificial viscosity. From these SWINT runs, the limitations in the robustness of the code were readily experienced. Reference 13 gives more information on the procedure for running the code, and Reference 14 describes in greater detail the numerical techniques used in the code.

2. The ZEUS Code

The ZEUS code, like the SWINT code, is used to calculate the flowfield about tactical missile configurations at supersonic speeds. The discussion used here is taken primarily from Reference 15. The solutions are found by using the Godunov scheme to integrate the Euler equations given on page 16. The Godunov method is a finite volume scheme which is based on the Riemann problem for steady, supersonic flow. Before the Godunov scheme is applied, the code takes the physical crossflow plane (s, υ, τ) and maps it onto a computational plane (ε, η, ζ) as shown in Figure 13.

The Riemann problem is represented by the intersection of two, two-dimensional supersonic streams as shown in Figure 14. When the streams intersect, they are both turned in a common direction through shock waves or expansion fans. The appropriate direction is the one which produces the same pressure in both streams. The Riemann problem is solved iteratively. The Godunov scheme evaluates fluxes using computed properties on the edges of control volumes shown in Figure 15. Some of the required computed properties are from the Riemann problem, while other required properties come from the initial conditions, the oblique shock relations, or the isentropic relations, depending on the region being solved (Ref. 12).

The ZEUS code uses a multiple zone procedure to generate the computational grid. This procedure involves dividing the crossflow plane into several zones. The zone edges must lie along the body, wing, and shock surfaces. For this computational investigation, the zones were defined for only half of the body. Symmetry was assumed for the other half of the body. These symmetry assumptions were made in order to save time during the runs and also to save storage space. An example of the one- and two-zone procedure used for this investigation's ZEUS runs is shown in Figure 16. This figure shows some of the restrictions which are required by the code, such as:

1. The body must define Edge 1, the shock must define Edge 3, and the wing surfaces (if any are present) must define Edge 2 or Edge 4.
2. Edge 2 and 4 must abut each other for adjacent zones.
3. The edges are numbered counterclockwise beginning with Edge 1.

As with the SWINT code, the ZEUS code requires that the flow be supersonic throughout the entire calculation.

The ZEUS code also requires a separate starting procedure to generate a starting flowfield. The starting procedure used was the one which came with the ZEUS code (Ref. 15). The starting case used the following inputs: number of radial cells, number of circumferential cells, angle-of-attack, Mach number, z location where the computation is initiated, body radius at the initial z location, and the body slope at the initial z location. These inputs are similar to the SWINT starting case inputs.

This starting case provides an estimate of a conical flowfield, which is only exact for a circular cone at zero incidence. This starting case was run not only for an angle of attack of 0^{o}, but also for angles-of-attack of 8^{o}, 16^{o}, and

20^{o} so an inexact, but very good approximation was obtained for the starting plane at the latter angles.

The output flowfield plane from the starting case is then used in the ZEUS code. ZEUS requires only the following user inputs: z location at which the run is terminated and the maximum step number. Additional inputs which specified instructions regarding plotting and printing were also specified. A one-zone technique (Fig. 16a) was used to march down the body to a z location just upstream of the fin. A two-zone procedure (Fig. 16b) was needed to calculate the flowfield over the fin region to the end of the body.

The grid size used for the one-zone procedure was 18 x 36, where the first number specifies the number of radial grid cells and the second number specifies the number of circumferential grid cells. For two-zone cases, the grid size for each zone was 18 x18. These grid sizes were determined based on previous ZEUS runs for similar configurations and on the sample cases from the ZEUS manual. For both zone cases, the cells were equally spaced from the body to the shock since no cell clustering was used. A few sample cases were obtained using grid sizes of 11 x 22 and 25 x 50 with no clustering used in either case. The 11 x 22 grid was not refined enough and yielded poor results. The 25 x 50 grid gave more accurate calculations than the 18 x 36 grid, but the run time was about nine times slower (4500 CPU seconds) for the larger grid. Better results from the ZEUS code may be possible by changing the grid size and/or by clustering the cells.

The ZEUS code was run for angles-of-attack of 0^{o}, 8^{o}, 16^{o}, and 20^{o} and for Mach numbers of 1.70, 2.16, 2.40, and 2.86. Since the code was encountering subsonic flow in certain cases, not all of the calculations were obtained for the entire body. Table IV lists the configurations, Mach numbers,

and angles-of-attack for which ZEUS was able to obtain calculations for the entire body.

Computed velocity crossflow plots were generated from ZEUS crossflow planes. Basically, the computer program which was used to obtain these plots uses the computed flowfield information at a specified longitudinal location. The vectors are plotted so that the velocity magnitude is directly proportional to the length of the plotted arrow. The original intent of using this program was to compare the crossflow plots to the vapor screens. Yet, the reproduction of regions of vorticity is beyond the scope of an Euler code, such as ZEUS. Thus, since the vortices are one of the main features on the vapor screens, a comparison of these vapor screens with the ZEUS-generated velocity vectors would tend to be somewhat unqualitative. Euler codes should be able to show rotational velocities, on the leeside leading edge of a wing, due to the discontinuity of the wing. These computed velocities could represent a vortex although these velocities are not turning due to vorticity, but rather due to the discontinuity mentioned previously. For the grid size and other conditions specified in this theoretical study, the ZEUS code did not show any rotational velocity vectors on the leeside surface of the wing leading edge.

An example of a crossflow plot is shown in Figure 17. The wing region of the plot is magnified in Figure 17b to better illustrate the velocity in this region. The plot correctly shows the flow velocity increasing towards the leading edge of the wing on the windward side. On the leeward side, the flow does not rotate at the leading edge, as was mentioned previously. The flow just above the wing and close to the body appears to have a low velocity. The flow seems to turn a little towards the top of the model. Overall, not many conclusions can be drawn from these crossflow plots which is why this topic is not pursued further.

Because of its zonal structure, the ZEUS code was able to handle the off-axis fin configurations and was found to be considerably more robust than the SWINT code. The multiple zone procedures employed in ZEUS made the geometry restrictions less stringent. The Godunov scheme is inherently more robust than the MacCormack scheme. This added robustness in the Godunov scheme is partially a result of the fact that the scheme is cast in a finite volume, rather than a finite difference, setting. Also, the ZEUS code does not need to apply special procedures at the surface edges.

The ZEUS code appeared to be the more robust code because it could be run from just upstream of the fin to the base of the body in a single stage for every successful run. On the other hand, the SWINT code often had to be run in multiple stages with trial and error input changes to reach the base of the body. For some of the lower Mach numbers and higher angle-of-attack cases, neither SWINT nor ZEUS could be run completely over the entire configuration without encountering subsonic flow. The only inputs which could be changed on ZEUS to attempt to get complete solutions were the mesh size and the marching step size. Changing these two variables, however, did not allow the marching to continue, and the ZEUS code was still not able to obtain a complete solution for these cases.

Nevertheless, ZEUS seemed more robust than SWINT because the ZEUS code either ran the entire length of the body with the given inputs or it did not. On the other hand, SWINT would sometimes obtain a complete solution with the initial given inputs, but often the input variables had to be changed to continue the calculation and, in some cases, a complete solution could not be obtained with any combination of inputs. References 1 and 2 contain more details on the robustness and other comparisons between ZEUS and SWINT.

Again, these codes were merely utilized as a means of obtaining the theoretical computations to assess their accuracy in predicting the experimental results.

CHAPTER IV

DISCUSSION OF RESULTS

The results presented in this report consist of pressure measurements, vapor screen photographs, and computational pressure predictions. These results will be presented in three parts: the experimental trends, the vapor screens, and comparisons between the theoretical calculations and the experimental data,

Prior to discussing the data results, however, a review of flowfield information for the basic components that make up the present configurations will be given.

1. Background Flowfield Information

The model used in this study consists essentially of two simple components:

1. a cylindrical body with a tangent ogive nose
2. a flat, highly swept delta wing

The flowfields of similar components have been analyzed in many previous studies, including References 16-18. A basic knowledge of the wing alone and body alone configurations provides a background for understanding the more complex flowfields of the wing/body configurations tested in this investigation. The next few paragraphs provide some basic flowfield information on body alone and wing alone configurations.

The crossflow plane of the body alone at angle of attack in supersonic flow is similar to Figure 18. The crossflow is symmetrical about the vertical plane of symmetry for the angles-of-attack (α's) of interest (-4^{o} to 24^{o}) and remains attached on the windward side of the body. As the flow travels around the body to the leeward side it expands and separates to form primary vortices. Because of the vortices, part of the flow is induced in a downward direction

towards the body leeward surface. This flow may reattach on the leeside surface and may separate to form secondary vortices which rotate in the opposite direction as the primary vortices.

Generally, flow over delta wings is divided into windward side and leeward side flow. A basic trend for delta wings at supersonic speeds includes the formation of vortices on the leeward side resulting from high pressures on the wind side and low pressures on the leeside which is also similar to the body alone trends. Windward side flow is usually attached and orderly for wing alone configurations; whereas, leeward side flow is very complex and has been the focus of much study.

For a delta wing with highly swept subsonic leading edges in supersonic flow, the leeside flow will separate resulting in a classical leading edge vortex (Ref. 16). An example of a classical leading edge vortex for wing alone is shown in Figure 19. This vortex is formed when the high pressure flow on the lower surface of the wing expands around to the upper surface of the wing. As the flow expands and separates at the leading edges, a primary vortex is formed. The primary vortex is highly rotational and can induce surface velocities which, in turn, can decrease the wing pressure distribution. This decrease in pressure results in an increase in lift, known as vortex lift. Furthermore, the primary vortex induces flow which may reattach to the wing surface at some point. The flow is streamwise inboard of this point and outward spanwise outboard of the point. The outward spanwise flow often separates into another vortex, known as the secondary vortex. The secondary vortex rotates in the opposite direction as the primary vortex and results in a further change in the pressure distribution. The classical vortex flow is only one of several types of flow which may occur in leeside flow at supersonic speeds, but this classical vortex flow gives a good representation of the

behavior of the flowfield. According to Reference 16, the delta wings for the Mach numbers and and α's used in this experiment should demonstrate classical vortex flow if tested as wing alone.

2. Experimental Pressure Trends

Normally, for wing alone and body alone data, wing pressures are plotted as a function of the spanwise coordinate, whereas body pressures are plotted as a function of circumferential angle. Thus, to conform to this style, the data are plotted in either one of two ways: Cp vs. Θ or Cp vs. Y/S where

Cp - coefficient of pressure

Θ - circumferential angle around the body (in degrees)

Y - spanwise location on the wing (in inches)

S - wing semispan at the trailing edge (4.82 inches)

Θ and Y are defined as shown in the diagram below:

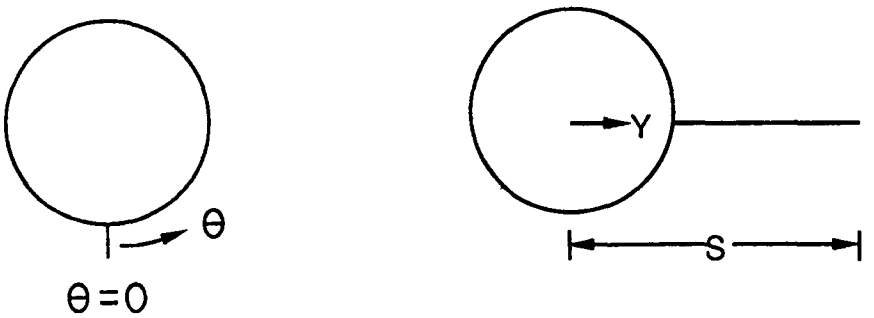

Thus, the Cp vs. Θ graphs provide information about the pressures around the body including the effect of the wing and the Cp vs. Y/S graphs provide information about the wing pressures including the effect of the body. As a consequence of the data, the windward side pressures are generally

represented by positive coefficients of pressure and the leeward side pressures are generally represented by negative coefficients of pressure.

One of the more important objectives of this experimental investigation was to observe how the different wing locations affected the pressure distributions both around the body and on the wings. The body alone configuration serves as an appropriate case to discuss initially since the pressure distribution with no wing effects can be shown. The experimental trends for each configuration will be discussed in the following order: body alone, bent-wing, inverted bent-wing, intermediate low-wing, low-wing, mid-wing, intermediate high-wing, and high-wing. This order was chosen so as to group the configurations with similar flow patterns together. For each configuration, except for body alone, first the body pressures and then the wing pressures will be discussed. For the body pressures, only $\Theta = 0^{o}$-180^{o} are discussed since through the range of angles-of-attack from -4^{o}-24^{o} the flow remains symmetric. The low Mach number (M = 1.70) and, usually, the high Mach number (M = 2.86) are shown in the analysis to provide the extreme range of Mach numbers.

Body Alone Configuration

The pressure distribution, for the body alone at station 1 and Mach number (M) = 1.70 as shown in Figure 20a, is somewhat irregular, especially on the leeside, mainly as a result of vortex interaction as observed in the vapor screen photographs. The pressure coefficient on the windward side is essentially zero for the low α's (-4^{o}, 0^{o}, and 4^{o}) and is positive for the higher α's. Also, for the higher α's, the pressure steadily decreases from the windward stagnation line ($\Theta = 0^{o}$) to negative values with increasing Θ until separation occurs at about $\Theta = 75^{o}$. After separation occurs, formation of the leeside vortices discussed previously can result in very complex pressure

distributions. After separation for M = 1.70, the pressure increases and then remains constant. For the other Mach numbers, the pressure remains essentially constant at the separation pressure.

Near the top of the model ($\Theta = 180^{o}$), the vortices are close to and possibly impinging on the surface, which causes a slight increase in the pressure. This increase in pressure at the top of the model due to the vortices will be referred to as the vortex impingement effect. This effect can be substantiated by observing vapor screen photographs. Even though the vortices themselves may not be lying on the surface of the model, the vortices induce the flow in a vertically downward direction at the top of the model. Thus, this induced flow may be causing the pressure increase. This impingement seems to have the largest effect at $\alpha = 12^{o}$-16^{o}. For α greater than 12^{o}, the vortices appear to be lifting off the body surface and the pressure increase is not as large. Stations 2 and 3 do not demonstrate the impingement effect (Figs. 20b-c), probably because the vortices at these downstream stations have lifted off the model surface throughout the range of α, but otherwise these two stations have the same approximate pressure patterns as those shown at station 1. For stations 2 and 3 at $\alpha = 24^{o}$, the flow appears to be asymmetric. Cp vs. Θ plots for the three stations at M = 2.86 are also shown in Figures 20d-f. In observing all the Mach numbers, the pressures behave in much the same way as the M = 1.70 case, but the pressures increase with increasing Mach number on both the wind and leeside. All of this experimental body alone data is consistent with the body alone flowfield information discussed previously.

Bent-Wing Configuration

Body. - The bent-wing body pressures at station 1 and the lower α's are similar to the body alone pressures. For example, at M = 1.70 , the pressure

coefficients for station 1 (Fig. 21a) are approximately zero around the entire body for the lower angles of attack. As with the body alone for higher α's the pressure decreases monotonically and becomes negative around the body until separation occurs at approximately $\Theta = 75^{o}$. The pressure increases slightly after separation occurs until the fin is encountered at $\Theta = 135^{o}$. The pressure coefficients on the leeside of the body are negative and increase slightly where the vortices impinge on the body. The pressures at station 2 behave in a similar manner (Fig. 21b), but separation occurs at about $\Theta = 60^{o}$. At station 2, increased wing interference effects resulting from the increase in the local span cause the flow to separate at smaller values of Θ. Also, since the pressures on the leeward surface between the fins at this station remain approximately constant, vortex impingement in this region is insignificant as in the results noted at this station for the body alone configuration (Fig. 20b).

At station 3, the wing interference effects are the greatest. As before for the higher α's, maximum pressures are measured at the windward stagnation line ($\Theta = 0^{o}$) and decrease until separation occurs at approximately $\Theta = 60^{o}$ (Fig. 21c). Unlike the other two stations, the pressure does not decrease to a negative value in the region of separation. This effect is probably due to a combination of the increased wing effect plus the effect of the wing leading edge shock. As with station 2, the vortices have lifted off the model surface on the leeward side so the pressures on the leeside remain constant. Through the test Mach number range for all the stations, the pressure tends to remain about the same as the M = 1.70 case on the windward side and tends to increase with increasing Mach number on the leeward side. Figures 21d-f show the three separate stations at M = 2.86 for all α's.

Wing. - For the bent wing configuration the wing begins at Y/S = 0.191. The wing leading edge is located at Y/S = 0.50, 0.75, and 0.95 for the stations 1, 2,

and 3, respectively. These values of Y/S for the wing leading edge are the same for every configuration. The wing pressures for the bent-wing configuration vary somewhat from station to station especially on the windward side, but each station has basically the same pattern for every Mach number. For station 1 (Figs. 21g-h), the pressures on the windward side remain positive and fairly constant for each α up to approximately 12^{o}. The $\alpha = 12^{o}$ case is not shown on the plots for the purpose of clarity, but the trend was verified based on a complete set of data For the higher α's, large pressure gradients occur where the pressures closest to the body are negative due to the wing-body interference. Towards the leading edge of the wing the pressures increase and reach a maximum value at the wing leading edge region. On the leeward side for any $\alpha > 0$, the pressure is negative and decreases even more towards the leading edge of the wing. This decrease is due to the vortex lift which was discussed previously.

At stations 2 and 3 (Figs. 21i-l), the windward side pressures behave like the pressures at stations 1 until $\alpha = 12^{o}$. For the higher α's, the pressures close to the body continue to decrease due to the wing-body interference until approximately Y/S = 0.5. For Y/S > 0.5, the body effects become less and the pressures increase. Then, because the cross-section at stations 2 and 3 consists of a larger spanwise section of the wing, the pressures decrease again as the flow begins to expand around the wing. The pressures on the leeside for stations 2 and 3 behave in much the same way as they did at station 1.

Inverted Bent-Wing Configuration

Body. - The body pressures for the inverted bent-wing configuration are definitely influenced by the presence of the wing. The pressure coefficients on the windward side at M = 1.70 (Figs. 22a-c) are about 0.3 larger in C_p than they are for the body alone case at the same α. The pressures below

the wing remain relatively constant from the windward stagnation line rather than decreasing as they did in the body alone case. Because of the wing, the flow is not able to expand as it goes around the body. The wing is located at $\Theta = 45^{o}$. On the leeside, the flow is probably in a low pressure separation region at about $\Theta = 60^{o}$ due to the vortices coming off the leading edge of the wing. The previous figures show the low pressure peaks on the leeside where the flow is separated. The pressure increases as the flow moves around the body and away from the vortex. The vortex impingement effect is especially prominent for $\alpha = 12^{o}$ and 16^{o} at M = 1.70 for station 1 (Fig. 22a). At stations 2 and 3 for all of the α's, no impingement effect is noticed since the pressure remains almost constant across the leeside. Only the M = 1.70 cases are shown because the same trends in pressure, except for the fact that the low pressure peak is not as exaggerated as it is in the M = 1.70 case, are also noticed at the higher Mach numbers.

Wing. - The wing pressures on the windward side of the bent-wing configuration are approximately constant at each α, but the pressure increases with increasing angle-of-attack as would be expected. On the leeward side of the wing at each station for M = 1.70 (Figs. 22d-f), the pressure, probably due to vortex lift, decreases moving away from the body and towards the leading edge of the wing. At the higher Mach numbers, the vortex lift effect to a lesser extent is observed at $\alpha > 8^{o}$. Also at each station for M > 1.70 the pressure coefficients at $\alpha = 16^{o}$ and 24^{o} are almost the same magnitude (Figs. 22g-i). Thus, for the higher Mach numbers and $\alpha > 16^{o}$, the angle-of-attack appears to have little effect on the pressures for the α range of this test.

Intermediate Low-Wing Configuration

Body. - The intermediate low-wing case has the wing located at $\Theta = 45^{o}$, just as in the inverted bent-wing case. The magnitude of the body pressures

on the windward side are lower for the intermediate low-wing case (Figs. 23a-c) than for the inverted bent-wing case, but otherwise the same pressure trends are observed in both cases. On the leeward side, the flow appears to be in a low pressure region from about $\Theta = 60^{o}$ to $\Theta = 75^{o}$. This region is once again probably a result of the leading edge wing vortex as was discussed in the inverted bent-wing case. Because the effective turning angle for the intermediate low-wing case is greater than that for the inverted bent-wing case, a larger low pressure region is formed for the intermediate low-wing case. Again, the low pressure region is much more prominent at the lower Mach numbers and higher angles-of-attack. As the Mach number is increased, the pressures remain fairly constant on the leeward side (Figs. 23d-f). Again, vortex impingement appears to be occurring on the top of the model. The trends of the vortex impingement in the intermediate low-wing case are similar to those previously discussed in the inverted bent-wing case.

Wing. - The wing pressures are nearly constant across the wing for each station on the windward side (Figs. 23g-i). This constant pressure trend holds even as M and α are increased. Thus, since the trends are similar for all M, only the M = 1.70 cases for each station are shown. Vortex lift effects are present on the leeward side for $\alpha > 0$ at each station. The leeside pressure trends differ from those discussed in the inverted bent-wing analysis. The reason for these different flow behaviors is not known. But, these different pressure trends could be caused by the fact that the effective turning angle which the flow must negotiate for the intermediate low-wing is greater than that for the inverted bent-wing.

Low-Wing Configuration

Since the graphs for the low-wing case are similar to the previously discussed intermediate low-wing configuration, no data are presented here.

Body. - For the low-wing case, no windward body pressures are recorded since the physical model wing covered the body until about $\Theta = 45^{o}$. The low-wing body pressure on the leeward side behaves in approximately the same manner and has approximately the same magnitude as the leeside pressure in the intermediate low-wing case. The low pressure region is present for the low Mach numbers and high angles-of-attack as before, and this region once again diminishes as M increases.

Wing. - For the low-wing case, the wing pressures on both the windward and leeward side have about the same pressure trends and magnitudes as the intermediate low-wing case.

Mid-Wing Configuration

Body. - For the mid-wing configuration, only the unrolled ($\beta = 0^{o}$) case is discussed in this analysis although data exist for the $\beta = \pm 30^{o}, 60^{o}, 90^{o}$ cases also. At station 1, the body pressure seems to remain almost constant at M = 1.70 (Fig. 24a) and increase at M = 2.86 (Fig. 24b) from the windward stagnation line until about $\Theta = 30^{o}$. Up to this Θ, this pressure trend is somewhat similar, especially for the M = 2.86 case, to the body alone pressure where the flow is expanding around the body and separating. A shock off the leading edge of the wing probably interferes with the body pressures and causes the pressure to increase until $\Theta = 60^{o}$ approximately. Because of this shock effect, the pressure does not continue to decrease as it did in the body alone. Instead, the pressure increases with increasing Θ. The shock effect is more pronounced as M increases. At approximately $\Theta = 60^{o}$, the pressure stops increasing and begins decreasing as the flow continues to expand around the body until the wing is encountered at $\Theta = 90^{o}$. On the leeward side of the body the pressures are negative since the flow is separated and is possibly in the low pressure region due to vortex lift previously discussed. The pressures increase slightly

as Θ increases. For $\alpha > 8^{o}$, the impingement effect appears to be present. For M = 1.70 this effect is most prominent at $\alpha = 16^{o}$ and for the higher Mach numbers this effect is most prominent at $\alpha = 12^{o}$ as noticed in the body alone case.

At stations 2 and 3 (Figs. 24c-f), the body pressures on the windward side remain fairly constant with the windward stagnation line pressure. The wing effects at these stations are increased and are possibly dominating the flow. Thus, the flow does not begin to expand at the windward stagnation line as it did in the station 1 case. On the leeward side for $\alpha > 4^{o}$ at M = 1.70 (Figs. 24c and 24e), the pressures from $\Theta = 90^{o}$ to 135^{o} decrease as the flow continues to expand around the body. At $\Theta = 135^{o}$, the pressures begin increasing due to the vortex possibly impinging on the body. At both stations 2 and 3 for M = 2.86 (Figs. 24d and 24f) and $\alpha > 4^{o}$ from $\Theta = 90^{o}$ to 150^{o}, the pressure remains fairly constant. At approximately $\Theta = 150^{o}$, the pressure increases slightly, possibly due to vortex impingement effects. These leeside trends are similar to the effects observed in the intermediate low- and the low-wing. For both stations 2 and 3, as the Mach number increases, the low pressure gradient on the leeside and the vortex impingement effect decreases.

Wing. - The wing pressures on the windward side for $\alpha < 8^{o}$ are constant along the wing for station 1 at all of the Mach numbers (Figs. 24g-h). Since the body interference effects are greater at station 1, the pressures nearest the body are less than those which are closest to the wing leading edge for $\alpha > 8^{o}$. The wing pressures at points nearest to the body are approximately equal to the body pressures at $\Theta = 75^{o}$ which is just before the Θ value where the wing is located. These similar pressures are probably due to the fact that the pressure on the wing is being dominated by the body flowfield. The pressure increases until $Y/S \cong 0.4$ and then begins to decrease again. The pressure

increases as the flow moves away from the body. The second decrease towards the leading edge of the wing results from the flow starting to expand around the wing. On the leeward side for $\alpha > 0^{o}$, vortex lift effects similar to those discussed in previous configurations are observed. At higher Mach numbers ($M > 1.70$), the vortex lift effect is most prominent at about $\alpha = 8^{o}$.

At stations 2 and 3 (Figs. 24i-l), the body interference effects are less. As a result, the pressures on the windward side remain constant along the wing rather than varying as they did at station 1. The leeward side flow is similar to that at station 1, but the wing vortex has probably lifted further off the wing causing the effect of decreased pressure due to vortex lift to be less than that observed at station 1.

Intermediate High-Wing Configuration

Body. - The intermediate high-wing configuration shows several interesting wing-body interference effects on the pressures around the body at station 1 (Fig. 25a). For $M = 1.70$ and $\alpha > 4^{o}$ the pressure decreases from the windward stagnation line until about $\Theta = 45^{o}$. This decreasing pressure is a result of the flow expanding around the body just as it did in the body alone case. For the other Mach numbers at station 1, the pressure decreases until about $\Theta = 60^{o}$ (Fig. 25b). At $\Theta = 45^{o}$ for $M = 1.70$ or at $\Theta = 60^{o}$ for the higher Mach numbers the shock effect occurs as discussed in the mid-wing configuration. Thus, because of this shock effect the pressure increases until about $\Theta = 90^{o}$ for all the Mach numbers. Then the pressures begin to decrease again as the flow expands around the body. A minimum pressure occurs around $\Theta = 105^{o}$. A sharp increase in the pressure is observed at $\Theta = 120^{o}$ which is located underneath the wing. This high body pressure is about the same value as the wing pressure closest to the body on the windward side and is probably the result of a high pressure separation region under the wing. On the leeward

side for $\alpha < 8^{o}$, the pressures remain constant across the top of the model. For $\alpha > 8^{o}$, the vortex probably impinges on the surface causing an increase in pressure near the top of the model.

For station 2 on the windward side, the shock effect, as discussed for station 1, is not present (Fig. 25c). As the Mach number increases, the shock effect becomes apparent (Fig. 25d). Also, because of the increased wing effect the pressure does not decrease as much as it did at station 1 as the flow expands around the body. Thus, the minimum pressure is not significantly lower than the other windward pressures as it was at station 1. The high pressure separation region becomes more prominent as M increases. For station 3 (Figs. 25e-f) on the windward side, the wing is dominating the flow, so the pressure remains essentially constant until about $\Theta = 75^{o}$ for each Mach number. The flow begins to expand past $\Theta = 75^{o}$, and at approximately $\Theta = 95^{o}$ a minimum pressure is reached. The pressure then increases in the possible high pressure region under the wing as discussed previously. For station 2 at M=1.70 (Fig. 25c), the pressures on the leeside increase at the top of the model for $\alpha = 20^{o}$ and 24^{o} approximately, while the pressures remain almost constant for the lower angles-of-attack. As the Mach number increases, the pressures for all of the α's remain essentially constant on the leeside for both stations 2 and 3. Also on the leeside for station 3 and $\alpha \geq 20^{o}$, the flow appears to be asymmetric for M = 1.70 (Fig. 25e). Yet, as the Mach number increases to 2.86, this flow appears to be symmetric.

Wing. - The pressures along the wing for the intermediate high-wing configuration are almost constant on the windward side for $\alpha < 8^{o}$ (Figs. 25g-i). As the angle-of-attack and the extent of crossflow increases the flow may behave similar to the flow over a forward facing step (Ref. 19). The pressures are high towards the leading edge of the wing and low close to the body, which

is similar to pressure level trends over the edge and base, respectively, of the face of a forward facing step. The flow near the body is possibly in a separated region which could explain the lower pressure. On the leeside of the wing, the vortex lift effect is present once again for $\alpha > 0^{o}$. The effect is especially pronounced at $\alpha = 8^{o}$ for all Mach numbers, but decreases for the higher α's at the higher Mach numbers. Since the trends are basically similar for all the Mach numbers, only M = 1.70 is shown.

High Wing Configuration

Since the trends for the high-wing case are similar to those of the intermediate high-wing case (Figs. 25a-i), no pressure plots are shown for the high-wing case.

Body. - The windward pressures around the high-wing configuration behave in much the same way as the intermediate high-wing configuration previously discussed. For the two configurations, the pressure trends are similar and overall the pressure magnitudes are almost equal Since the high wing was mounted at the top of the body, no leeside body pressures are available.

Wing. - The wing pressures on both the windward and leeward sides of the high-wing case also have the same trends as those observed in the intermediate high-wing. Both the windward and leeward wing pressures for the high-wing case have about the same magnitude (within 0.03 C_p) as their intermediate high-wing counterparts.

3. Selected Vapor Screens

The vapor screen photographs serve as a valuable tool in the analysis of the experimental pressure data, especially on the leeside of the model. The vapor screen photographs show leeside vortices, shocks, plus some other flow phenomena. These photographs are useful in helping to explain some of the

trends seen in the experimental pressure graphs. Because of the quality of some of the vapor screen photographs and the sheer quantity, only selected photographs will be presented in this section. The photos were taken at $\alpha = 12^{o}$ and 20^{o}. In the experimental pressure discussion, the M = 1.70 and M = 2.86 cases were discussed. Therefore, only these two Mach numbers will be highlighted in the following sections. The white arrows on the vapor screen photographs indicate regions of interest.

Body Alone Configuration

Vapor screens were taken at stations 1 and 3 for the body alone, and at stations 1, 2, and 3 for all of the other configurations. The quality of the photograph for the M = 1.70 and $\alpha = 12^{o}$ for station 1 is too poor to discern any flowfield information. For the body alone at M = 1.70 and $\alpha = 12^{o}$, two symmetrical vortices, which have lifted from the body are observed at station 3. For M = 2.86 and $\alpha = 20^{o}$, symmetrical vortices which are close to the top of the model can be seen at station 1. At station 3, these vortices have become elongated and have lifted from the body. These vortices also have shocks emanating from them. All of the vapor screens are consistent with the experimental data and validate the pressure trends. Because of the overall poor quality of the photographs none of the body alone vapor screens are shown.

Bent-Wing Configuration

From the bent-wing vapor screen photographs, classical vortices, as discussed in the background flowfield information, can be seen emanating from the leading edge of the wing. For M = 1.70 and $\alpha = 12^{o}$, these vortices lie close to the wing surface and remain similar in shape at each station. Figure 26a shows the vortices at station 3 where M = 1.70 and $\alpha = 12^{o}$. From this figure, a possible vortex is seen under the wing which, as seen from the experimental

data, could be causing the pressure increase that begins at $\Theta = 60^{o}$ in Figure 21f. Also observed in Figure 26a are a pair of faint dark vertical projections, which may be associated with a pair of shock waves that are formed as the leeward flow realigns with the vertical plane of symmetry. For the same flow conditions, these projections were not observed at the first two stations. As the angle-of-attack is increased to 20^{o}, the vortices have lifted further from the wing surface, but otherwise have the same structure as those found at $\alpha = 12^{o}$. The vertical projections are present at all three stations in the M = 1.70 and $\alpha = 20^{o}$ case. The wing vortices for M = 2.86 and $\alpha = 12^{o}$ look almost identical in size and shape to those found at M = 1.70 and $\alpha = 12^{o}$. At M = 2.86 and $\alpha = 20^{o}$ (Fig. 26b), the wing vortices have elongated and have shocks emanating from them at station 2. These shocks were also observed at the other two stations. The vortices at these conditions seem to be further from the surface than the ones at M = 2.86 and $\alpha = 12^{o}$. No vertical projections are observed in any of the M = 2.86 cases.

The photographs help verify the vortex lift theory on the leeside of the wing. The photographs also show that the vortices themselves may not actually be impinging on the top surface of the model. The flow is probably forced around the vortices in such a manner that the pressure will show an increase at $\Theta = 180^{o}$ as can be seen in the experimental data.

Inverted Bent-Wing Configuration

The inverted bent-wing configuration has some interesting flowfield phenomena. If any wing vortices or separation bubbles are located on leeside of the wing, they are not readily observed from the vapor screens at M = 1.70 and $\alpha = 12^{o}$. A very faint wing vortex can be seen at M = 1.70 and $\alpha = 20^{o}$ (Fig. 27a). Two obvious symmetric body vortices are present, though, for both angles-of-attack. These body vortices lie close to the body at $\alpha = 12^{o}$ and lift

from the body for $\alpha = 20^{o}$. The vortices also lift from the body at the more aft stations for both angles-of-attack. On top of the model, two finger-like vertical projections are present (Fig. 27a). These may be similar to the ones observed in Figure 26a. At M = 1.70 and for both $\alpha = 12^{o}$ and $\alpha = 20^{o}$, these projections become more developed from station 1 to station 3. The origin of the projections is not known presently; although, as discussed previously, they may be from shocks which possibly develop from the symmetrical behavior of the flow. At M = 2.86, the separation bubble on the wing is hard to discern, but apparently it still exists and may even have a shock emanating from it. Again, the body vortices lie closer to the body at the lower angle-of-attack ($\alpha = 12^{o}$) and at station 1. As the angle-of-attack increases and/or a more aft body station is reached, the vortices lift from the body. At $\alpha = 20^{o}$, the vortices appear to have shocks emanating from them. Furthermore, the projections which were present at M = 1.70, no longer exist (Fig. 27b) at either angle-of-attack. Although the projections are absent at M = 2.86, the pressure distribution trends across the top of the model do not change significantly from the M = 1.70 trends. Thus, the effect, if any, of the finger-like projections on the leeside pressure is not obvious.

Intermediate Low-Wing

At M = 1.70 and $\alpha = 12^{o}$, the intermediate low-wing configuration has very definite classical wing vortices as opposed to the case of the inverted bent-wing configuration. Also, body vortices exist which are similar to the ones on the inverted bent-wing. Both the wing and body vortices lie on the model surface at station 1 and gradually lift at the further aft stations. Possible faint traces of the finger-like projections found in the inverted bent-wing case can be seen at station 1 for the intermediate low-wing case. Again, these

projections grow stronger at the more aft locations as shown in Figures 28a-c. No vapor screen photographs were available at M = 1.70 and $\alpha = 20^{o}$.

At the higher Mach number (M = 2.86), the wing vortices appear to have shocks coming from them at all three stations. The body vortices no longer evidance a feeding sheet for either the $\alpha = 12^{o}$ case (Fig. 28d) or the $\alpha = 20^{o}$ case. The feeding sheet, which probably emanates from the windward side of the wing, is evidenced by the curved line and is connected tangentially to the core vortex. At $\alpha = 20^{o}$, the body vortices become elongated and also appear to have shocks on them. No finger-like projections are noticed for the M = 2.86 case.

Low-Wing Configuration

The low-wing configuration has vapor screens which appear to be almost identical to those of the intermediate low-wing The vortices even have essentially the same size and shape in both cases. Thus, no figures are shown for the low-wing case.

Mid-Wing Configuration

At M = 1.70 and $\alpha = 12^{o}$ for stations 1 and 2, the mid-wing vapor screens are similar to those of the intermediate low-wing. At station 3, the classical wing vortices are observed. Probably since the flow has less body surface to go around on the leeward side as compared to the intermediate low-wing and the low-wing configuration, no body vortices have formed. Instead, only the finger-like projections are present on the top surface of the model (Fig. 29a). The vortices are somewhat larger, but otherwise follow the same pattern as the M =1.70 and $\alpha = 12^{o}$ from station to station for M = 1.70 and $\alpha = 20^{o}$

At M = 2.86, as with the other low-mounted fin cases no finger-like projections are noticed. The body vortices at station 3 (Fig. 29b) for both angles-of-attack are very small compared to those of the intermediate low-

wing. At stations 1 and 2, the size of the mid-wing vortices seem comparable to those of the intermediate low-wing. The body vortices for the mid-wing case have feeding sheets as opposed to the low- and intermediate low-wing cases. The M = 2.86 low-wing case shows shocks emanating from the vortices in a similar manner as those observed in the other low-mounted fin cases.

Intermediate High Wing Configuration

The intermediate high-wing photographs show classical vortices on the wings. For M = 1.70 and $\alpha = 12^{o}$ (Figs. 30a-c), the vortices are fairly small and probably remain far enough from the body so that the leeside body pressures are unaffected as confirmed in Figures 22a, 22c, 22e. At stations 2 and 3, secondary vortices can be seen. Also at station 3, a dark region appears on the windward side under the wing and close to the body. This region probably indicates the high pressure separation region discussed in the experimental trends. The quality of the photographs for the M = 1.70 and $\alpha = 20^{o}$ cases were too poor to make any analysis. However, based on the trends observed in the previous cases, the vortices in these cases are probably larger than the $\alpha = 12^{o}$ case so that they interfere with the body pressures.

For M = 2.86 and $\alpha = 12^{o}$, the vortices appear somewhat larger but, otherwise, are almost identical to the M = 1.70 case. The vortices for the M = 2.86 and $\alpha = 20^{o}$ cases appear larger, more elongated, and more diffuse (Fig. 30d) than the M = 2.86 and $\alpha = 12^{o}$ vortices. Also, the vortices at $\alpha = 20^{o}$ have shocks emanating from them which seem weaker than those observed in the previous configurations at the same angle-of-attack.

High-Wing Configuration

The M = 1.70 and $\alpha = 12^{o}$ cases for the high-wing are similar to those of the intermediate high-wing. At $\alpha = 20^{o}$, the wing vortices are larger than those observed for $\alpha = 12^{o}$ and lift off the surface more for the aft stations

(Figs. 31a-c). These figures are shown since the photographs for the intermediate high-wing at $\alpha = 20^{o}$ did not develop.

All of the M = 2.86 and $\alpha = 12^{o}$ vapor screens for the high wing look almost identical to those of the intermediate high-wing. At M = 2.86 and $\alpha = 20^{o}$, the vortices have shocks coming off them as expected. But, at these conditions, the vortices seem to have a horizontal shock between them (Fig. 31d) that was not noticed in the intermediate high-wing case.

4. Comparisons Between Theoretical Computations and Experimental Data

Another major motivation for this investigation was to compare the theoretical calculations with the experimental data for the off- axis fin configurations (i.e., the high-, low-, intermediate high-, and intermediate low-wing configurations). Although the SWINT code was run for all of the on-axis cases, none of the on-axis fin calculations are discussed because of already existing reports on similar cases (Refs. 2, 3, and 12). For the same configurations, ZEUS has been found to give results similar to SWINT. Thus, only the off-axis cases are discussed in this section because SWINT is unable to calculate the flowfields for these cases. The comparisons are presented in the same way as the experimental data in the previous section with Cp vs. Θ graphs for body pressures and Cp vs. Y/S graphs for wing pressures. The ZEUS code was run for nominal angles-of-attack of 0^{o}, 8^{o}, 16^{o}, and 20^{o}. In most cases, however, for the lower Mach numbers (M = 1.70 and 2.16) especially, the ZEUS code was unable to obtain a complete solution for the body for $\alpha = 16^{o}$ and 20^{o}, probably because subsonic flow was encountered. For every configuration for both windward and leeward wing and body pressures, ZEUS calculated $Cp \cong 0$ at $\alpha = 0^{o}$ for all stations, which is accurate in all cases when compared to the experimental data. Thus, the $\alpha = 0^{o}$ case will not be discussed for any of the

configurations. The angle-of-attack for some of the experimental cases varied up to 0.7^{o} from the nominal angles listed previously. For a few cases, ZEUS was run at the exact experimental angle-of-attack and the data were almost identical to the other ZEUS computations for the nominal angles-of-attack. Thus, to limit the number of ZEUS cases to run, the nominal values for the α's were used in the ZEUS calculations without any loss of generality in the comparison with the experimental data.

Intermediate Low-Wing Configuration

Body. - For M = 1.70 and $\alpha = 8^{o}$ at station 1 (Fig. 32a), the ZEUS pressure coefficients on the windward side decrease by about 0.03 until approximately $\Theta = 30^{o}$ and then increase by about the same amount until just ahead of the wing ($\Theta = 45^{o}$). On the other hand, the experimental pressures remain fairly constant on the windward side. Although the same pressure trends are not observed, the experimental and the ZEUS pressures on the leeward side are always within a C_p of about 0.02 of each other. At first glance, a coefficient of pressure range of 0.02 may appear to be in good agreement. However, this 0.02 difference between the experimental and theoretical pressure coefficients could result in percent differences from about 20% to 100%. For stations 2 and 3 (Figures 32b and 32c, respectively), the ZEUS pressures on the windward side are within a C_p of about 0.01 of the experimental values. For station 2 (Fig. 32b) on the leeward side, the ZEUS pressures increase until about $\Theta = 105^{o}$ and then remain constant as Θ increases. Except for the Θ location above the wing (at about $\Theta \cong 60^{o}$), the experimental and the ZEUS pressures are again within about 0.02 C_p of each other. Above the wing, ZEUS predicts a lower pressure than the experimental data. Also, ZEUS does not predict the slight increase in pressure at the top of the model due to vortex impingement. Station 3 (Fig. 32c) exhibits similar trends as those just discussed for station 2.

Additional α = 16° and 20° cases were obtained for M = 2.86 using the ZEUS code. At M = 2.86, ZEUS was accurate in predicting the windward side pressures at all three stations to within at least a C_p of 0.02 of the experimental values. On the leeward side for station 1 (Fig. 32d), ZEUS accurately predicts the pressures for α = 8° up to approximately Θ = 90°. Between Θ=90° and 150°, the ZEUS pressure coefficients are about 0.04 too high when compared to the experimental data. The experimental data trends for α = 16° and 20° are almost identical to each other. The ZEUS pressures are accurate for these angles-of-attack from about Θ = 60° to Θ = 90°. As the experimental data remain essentially constant, the theoretical pressures decrease and then inaccurately begin to increase towards the top of the model at about Θ = 150°. The reason for this theoretical trend is not known. For stations 2 and 3 (Figs. 32e and 32f, respectively), the computed pressures are within at least 0.05 C_p of the experimental pressures. The code does not always follow the trends of the experimental data, though.

Wing. - On the windward side, the predicted ZEUS wing pressures are accurate to within at least 0.02 - 0.03 C_p of the experimental data. The ZEUS pressures also follow the same constant pressure trends shown by the experimental data, except toward the leading edge of the wing ZEUS predicts a sharp increase in pressure. This increased pressure is not noticed for every case, and is discussed in greater detail in the wing section for the intermediate high-wing configuration. On the leeward side, ZEUS is unable to predict the vortex lift effect accurately at any station. Figure 32g shows station 3 at M = 1.70. As the Mach number increases, the vortex lift effect diminishes (Fig. 32h), but ZEUS is still unable to predict the pressure trends shown by the experimental data.

Low-Wing Configuration

Body. - The leeward pressures for the low-wing follow the same trends as the intermediate low-wing according to the experimental data. Similarly, the ZEUS pressures for these configurations follow the same trends. Thus, approximately the same discrepancies noted in the intermediate low-wing pressure comparison can be seen in the low-wing comparison. For this reason, no further discussion is given on the low-wing plots. However, even at M = 2.86, the ZEUS code was only able to obtain calculations up to the $\alpha = 16^{o}$ case for the low-wing configuration.

Wing. - The wing pressures exhibit similar trends as those discussed for the intermediate low-wing configuration. Thus, no plots are shown for the low-wing configuration.

Intermediate High Wing Configuration

Body. - For the intermediate high-wing case, the ZEUS code was able to obtain calculations only for the $\alpha = 0^{o}$ and 8^{o} cases for M = 1.70, 2.16, and 2.40. At M = 2.86, ZEUS was able to run at $\alpha = 16^{o}$ also. At M = 1.70 and $\alpha = 8^{o}$ for station 1, the ZEUS pressures are fairly constant on the windward side (Fig. 33a). ZEUS does not predict the decrease in pressure near $\Theta = 120^{o}$ or the increase in pressure in the region under the wing. For station 2, both the experimental and the ZEUS pressures are fairly constant on the windward side and are of almost the same magnitude (Fig. 33b). At station 3, the ZEUS pressures again are fairly constant around the windward side and are of the same approximate magnitude as the experimental pressures (Fig. 33c). The experimental data show pressure variations which ZEUS does not predict. For the leeward side flow at station 1, the predicted ZEUS pressure shows a sharp increase at about $\Theta = 150^{o}$ which is not shown in the experimental data. The leeside pressures at station 2 and 3 are accurately predicted by ZEUS. For the

body alone case, the ZEUS code accurately predicts the pressure on the windward side, but the code is inaccurate for the leeside. Yet, for the high-mounted fin configurations, ZEUS seems to be accurate for the leeside and inaccurate for the windside pressures. Apparently, the presence of the fin causes interference effects which the ZEUS code is unable to predict.

For station 1 at M = 2.86 (Fig. 33d), the ZEUS code does not accurately predict either the shock effect or the high pressure region found on the windward side in the experimental data. For the two higher α's, the ZEUS pressures seem to decrease as they would for body alone until about $\Theta = 90^{o}$. Then the ZEUS pressures begin increasing until just before the wing location. For station 2 and 3 at $\alpha = 8^{o}$ (Figs. 33e-f), the ZEUS windward pressures match the experimental windward pressures to within approximately 0.02 C_p. For station 2 at $\alpha = 16^{o}$ on the windward side (Fig. 33e), the ZEUS pressures decrease to a minimum at about $\Theta = 60^{o}$ and then increase; whereas, the experimental pressure is fairly constant until showing a slight increase in the high pressure region just under the wing. For station 3 (Fig. 33f) at $\alpha = 16^{o}$ on the windward side, the ZEUS pressure coefficient increases steadily (about 0.08 in C_p) from the windward stagnation line until just before the wing. The experimental pressure trend, on the other hand, remains relatively constant until about $\Theta = 75^{o}$. Then the pressure decreases until about $\Theta = 90^{o}$ and then increases again due to the high pressure region under the wing. Thus, the experimental and theoretical pressures have different pressure trends since the code is unable to predict the high pressure region which is due to viscous separation. The leeward side ZEUS pressures are accurate at every station and every α for M = 2.86.

Wing. - For each station and every α, the agreement between the experimental data and the computational estimates improves with increasing

Mach number. This trend is shown for station 3 at M = 1.70 and M = 2.86 (Figs. 33g-h). On the windward side, the experimental pressures remain fairly constant. the ZEUS pressures at each station and Mach number follow this trend and remain within 0.02 C_p of the experimental values. However, in certain cases, when the leading edge of the wing falls slightly inside a computational cell, the ZEUS code on the windward side predicts a significant pressure increase of about 0.1 - 0.3 C_p (Fig. 33h) for this cell. Since the orifices did not quite go out to the leading edge, no experimental pressures are given in this region. But since the flow is expanding around the wing to the leeward side, the pressures should show a decrease rather than an increase. The tendency of ZEUS to predict this increase around the leading edge region has been noticed in other reports (Ref. 2). The reason for this predicted pressure increase is not known, but is apparently a problem inherent within the code.

High-Wing Configuration

As discussed previously, the experimental pressure trends for the intermediate high-wing and the high-wing cases are similar. In the same way, ZEUS pressure trends are similar for the intermediate high-wing and the high-wing. Again, for M = 1.70 for the high-wing case, ZEUS calculations could only be obtained for $\alpha = 0^o$ and 8^o. However, at M = 2.86, ZEUS was able to obtain runs for $\alpha = 0^o$, 8^o, 16^o, and 20^o. Since the trends are similar between the intermediate high- and the high-wing configurations and since these trends have already been discussed, the graphs of the experimental and theoretical comparisons for the high-wing are not presented.

Wing. - Again, the ZEUS trends for the wing pressures on the high-wing configuration are similar to those of the intermediate high-wing. Thus, no graphs are shown.

CHAPTER V

CONCLUDING REMARKS

An experimental and theoretical pressure and flow visualization investigation was conducted on a cylindrical missile model with a tangent ogive nose. The model was tested using fins located at various vertical locations. The experimental investigation consisted of wind tunnel pressure tests and flow visualization tests in the form of vapor screen photographs. The theoretical investigation was made using Euler codes developed for tactical missile configurations at supersonic speeds. The tests were conducted for a range of Mach numbers from 1.70 to 2.86 and a range of angles-of-attack from -4^{o} to 24^{o}. The results from these tests are summarized as follows:

(1) For every configuration, a general trend of increasing pressure with increasing angle-of-attack existed on the windward side and of decreasing pressure with increasing angle-of-attack on the leeward side.

(2) Wing-body interference effects were obvious for all configurations with wings. These interference effects seemed to be greater at the more aft stations on the body, possibly because the local cross-section of the spanwise section of the wing increases with increasing longitudinal values.

(3) For configurations with fins mounted at or below the centerline, the windward pressures at some longitudinal stations on the fuselage were apparently affected by the wing leading edge shock.

(4) Also on the windward side, for configurations with fins mounted above the centerline, a high pressure separation region existed on the body under the wing.

(5) Most of the configurations, to varying degrees, exhibited effects of vortex lift on the wing and body. This effect was characterized by a decrease in the pressure due to wing vortices.

(6) An increase in pressure was noted in certain cases where the body vortex appeared to be impinging on the top surface of the model. The vortex impingement effect seemed to be diminished at the more aft stations on the body.

(7) The vapor screen photographs provided additional support for conclusions about the origin of many of the leeside effects, such as the vortex lift and the vortex impingement effects. In some cases, even the evidence of the high pressure region under the wing could be seen. For some configurations, symmetrical finger-like projections were present on the top surface of the model. The origin of these projections is unknown, but they may be associated with a pair of shock waves that are formed as the leeward flow realigns with the vertical plane of symmetry.

(8) The ZEUS code seems to be able to predict the pressures for the off-axis cases to within 0.03 C_p of the experimental data for the lower angles-of-attack ($\alpha \leq 8^o$) and the higher Mach numbers (M = 2.40 and 2.86). Yet, the code does not follow the same pressure trends as the experimental data. Because subsonic flow is encountered, the code cannot calculate the flowfield for the lower Mach numbers (M = 1.70 and 2.16) and the higher angles-of-attack ($\alpha \geq 8^o$). Apparently because of the highly viscous nature of the flowfield of the off-axis fin configurations, the ZEUS code is unable to handle the wing-body interference effects on either the windward or leeward side. A possibility for future study would be to change the grid size and/or to cluster the grid cells to determine if better theoretical calculations can be obtained.

REFERENCES

1. Wardlaw, Andrew B., Jr.: Space Marching Euler Solvers. AGARD Report No. 754, Special Course on Missile Aerodynamics, 1987, pp. (5-1) - (5-32).

2. Priolo, F. J.; and Wardlaw, A. B., Jr.: A Comparison of Inviscid Computational Methods for Supersonic Tactical Missiles. AIAA 87-0113, January 1987.

3. Allen, J. M.; and Townsend, J. C.: Application of a Supersonic Euler Code (SWINT) to Wing-Body-Tail Geometries. Journal of Aircraft, Vol. 23, No. 6, June 1986, pp. 513-519.

4. Blair, A. B.: Effect of Wing Location and Strakes on Stability and Control Characteristics of a Monoplanar Circular Missile with Low-Profile Tail Fins at Supersonic Speeds. NASA TM-81878, December 1980.

5. Jackson, Charlie M., Jr.; Corlett, William A.; and Monta, William J.: Description and Calibration of the Langley Unitary Plan Wind Tunnel. NASA TP-1905, November 1981.

6. Baals, Donald D.; and Corliss, William R.: Wind Tunnels of NASA. NASA SP-440, 1981.

7. Stallings, Robert L., Jr.; and Lamb, Milton: Effects of Roughness Size on the Position of Boundary-Layer Transition and on the Aerodynamic Characteristics of a 55^{o} Swept Delta Wing at Supersonic Speeds. NASA TP-1027, 1977.

8. Potter, J. Leith; and Whitfield, Jack D.: Effect of Unit Reynolds Number, Nose Bluntness, and Roughness on Boundary Layer Transition. AEDC TR-60-5, March 1960.

9. Braslow, Albert L.; and Knox, Eugene C.: Simplified Method for Determination of Critical Height of Distributed Roughness Particles for Boundary Layer Transition at Mach Numbers from 0 to 5. NACA TN-4363, September 1958.

10. Braslow, Albert L.; Hicks, Raymond M.; and Harris, Roy V., Jr.: Use of Grit-Type Boundary-Layer Transition Trips on Wind-Tunnel Models. NASA TN D-3579, September 1966.

11. Morris, Odell; Corlett, William A.; Wassum, Donald L.; and Babb, C. Donald: Vapor Screen Technique for Flow Visualization in the Langley Unitary Plan Wind Tunnel. NASA TM-86384, July 1985.

12. Wardlaw, A. B., Jr.; and Davis, S. F.: A Second-Order Godunov Method for Tactical Missiles. NSWC TR 86-506, December 1986.

13. Wardlaw, A. B., Jr.; Hackerman, L. B.; and Baltakis, F. P.: An Inviscid Computational Method for Supersonic Missile Type Bodies - Program Description and User's Guide. NSWC TR 81-459, December 1981.

14. Wardlaw, A. B., Jr.; Baltakis, F. P.; Solomon, J. M.; and Hackerman, L. B.: An Inviscid Computational Method for Tactical Missile Configurations. NSWC TR 81-457, December 1981.

15. Wardlaw, A. B., Jr.; and Priolo, F. J.: Applying the ZEUS Code. NSWC TR 86-508, December 1986.

16. Miller, David S.; and Wood, Richard M.: Lee-Side Flow over Delta Wings at Supersonic Speeds. NASA TP-2430, June 1985.

17. Stallings, Robert L., Jr.; and Lamb, Milton: Wing-Alone Aerodynamic Characteristics for High Angles of Attack at Supersonic Speeds. NASA TP-1889, July 1981.

18. Landrum, Emma Jean: Wind-Tunnel Pressure Data at Mach Numbers from 1.6 to 4.63 for a Series of Bodies of Revolution at Angles of Attack from -4° to 60°. NASA TM X-3558, October 1977.

19. Stallings, Robert L., Jr.; and Wilcox, Floyd J., Jr.: Experimental Cavity Pressure Distributions at Supersonic Speeds. NASA TP-2683, June 1987.

20. Wardlaw, A. B., Jr.: High Angle-of-Attack Missile Aerodynamics. AGARD Lecture Series No. 98, May 17, 1979, p. 5-6.

Table I. - Test Parameters

Mach #	Reynolds #	p_o in PSF	T_o in $^\circ$F
1.70	2×10^6/ft	1113	125
2.16	"	1349	"
2.40	"	1520	"
2.86	"	1934	"

The angles-of-attack ranged from -4° to 24° in increments of 4°.

TABLE II.- Wing Orifice Locations
(see Figure 7)

CONFIGURATION				ORIFICE POSITION #	STATION	$\bar{y}$ (inches)	SLOPE OF RAYS
BW	MW	IHW	HW				
-	-	-	1	1	1	0.241	0.023
-	-	-	2	2		0.482	0.046
-	-	-	3	3		0.723	0.069
-	-	4	4	4		0.964	0.092
-	-	5	5	5		1.205	0.115
6	6	6	6	6		1.446	0.139
7	7	7	7	7		1.687	0.162
8	8	8	8	8		1.929	0.185
9	9	9	9	9		2.049	0.196
10	10	10	10	10		2.170	0.208
-	-	-	11	11	2	0.361	0.023
-	-	-	12	12		0.722	0.046
-	-	13	13	13		1.083	0.069
14	14	14	14	14		1.444	0.092
15	15	15	15	15		1.806	0.115
16	16	16	16	16		2.167	0.139
17	17	17	17	17		2.528	0.162
18	18	18	18	18		2.889	0.185
19	19	19	19	19		3.070	0.196
20	20	20	20	20		3.250	0.208
-	-	-	21	21	3	0.914	0.046
-	-	22	22	22		1.321	0.069
23	23	23	23	23		1.829	0.092
24	24	24	24	24		2.281	0.115
25	25	25	25	25		2.743	0.139
26	26	26	26	26		3.200	0.162
27	27	27	27	27		3.657	0.185
28	28	28	28	28		3.886	0.196
29	29	29	29	29		4.114	0.208

BW - bent-wing configuration
MW - mid-wing configuration
IHW - intermediate high-wing configuration
HW - high-wing configuration

Table III. - Range of Accuracy for C_p

Δp=2-3psfa

M_∞	p_o in psf	q_∞ / p_o	ΔC_p
1.70	1113	.4098	.004 - .007
2.16	1349	.3252	.005 - .007
2.40	1520	.2758	.005 - .007
2.86	1934	.1926	.005 - .008

$$\Delta C_p = \frac{\Delta p}{\left(q_\infty / p_o\right) p_o}$$

Table IV. - ZEUS Parameters

Configuration	Angles-of-Attack at Mach #'s			
	1.70	2.16	2.40	2.86
ILW	0°, 8°	0°, 8°, 16°	0, 8, 16	0, 8, 16, 20°
IHW	0°, 8°	0, 8	0, 8	0, 8, 16
HW	0°, 8	0, 8	0, 8, 16	0°, 8°, 16°, 20°
LW	0°, 8°	0°, 8°, 16°	0°, 8°, 16°	0°, 8°, 16°, 20°

ILW - intermediate low-wing
IHW - intermediate high-wing
HW - high-wing
LW - low-wing

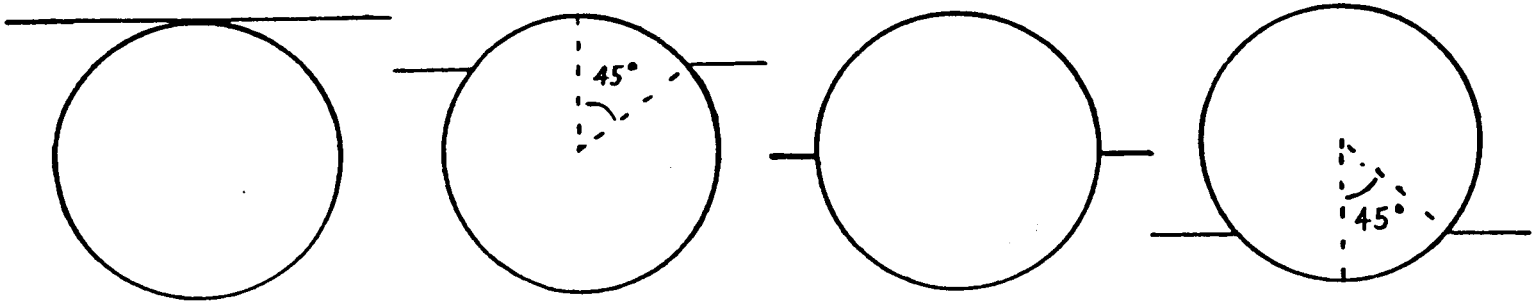

HIGH-WING INTERMEDIATE HIGH-WING MID-WING INTERMEDIATE LOW-WING

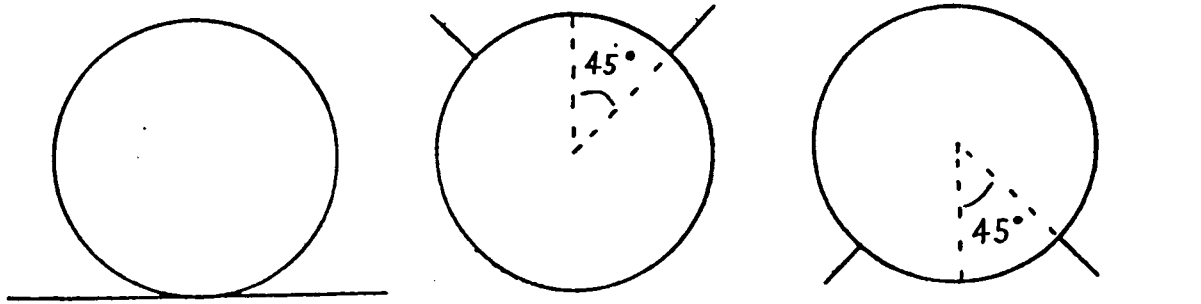

LOW-WING BENT-WING INVERTED BENT-WING

Figure 1.- Cross-Sections Depicting the Various Wing Locations

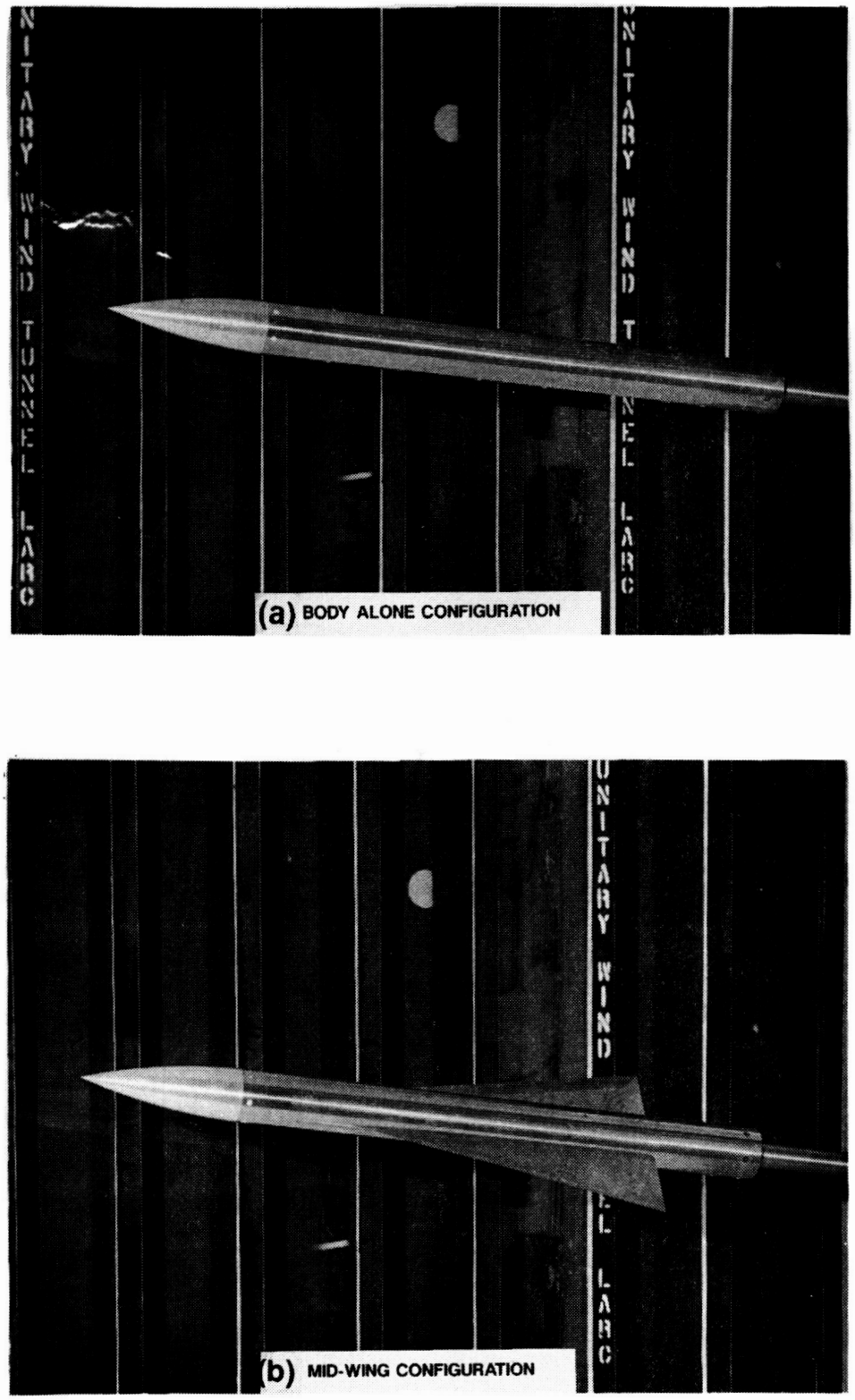

Figure 2.- Missile Configurations

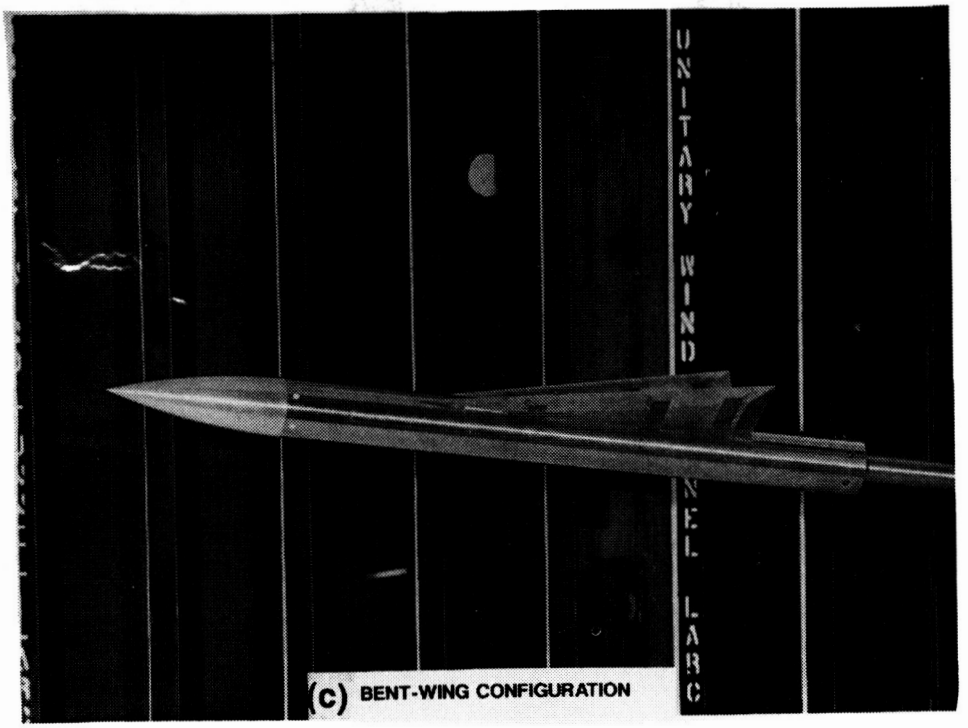

(c) BENT-WING CONFIGURATION

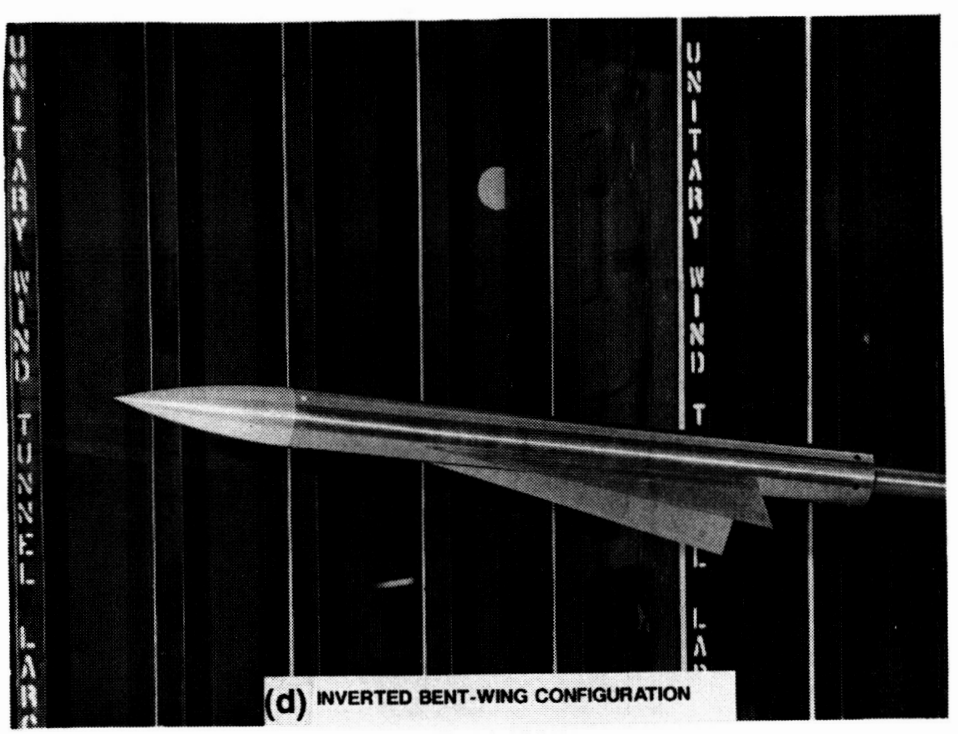

(d) INVERTED BENT-WING CONFIGURATION

Figure 2.- Continued

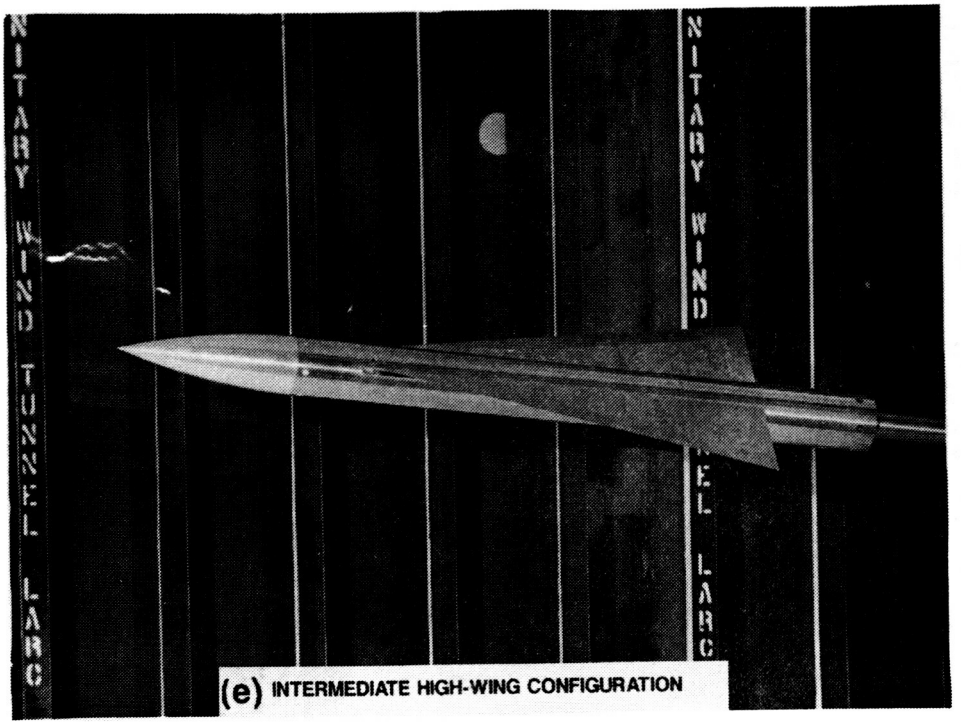

(e) INTERMEDIATE HIGH-WING CONFIGURATION

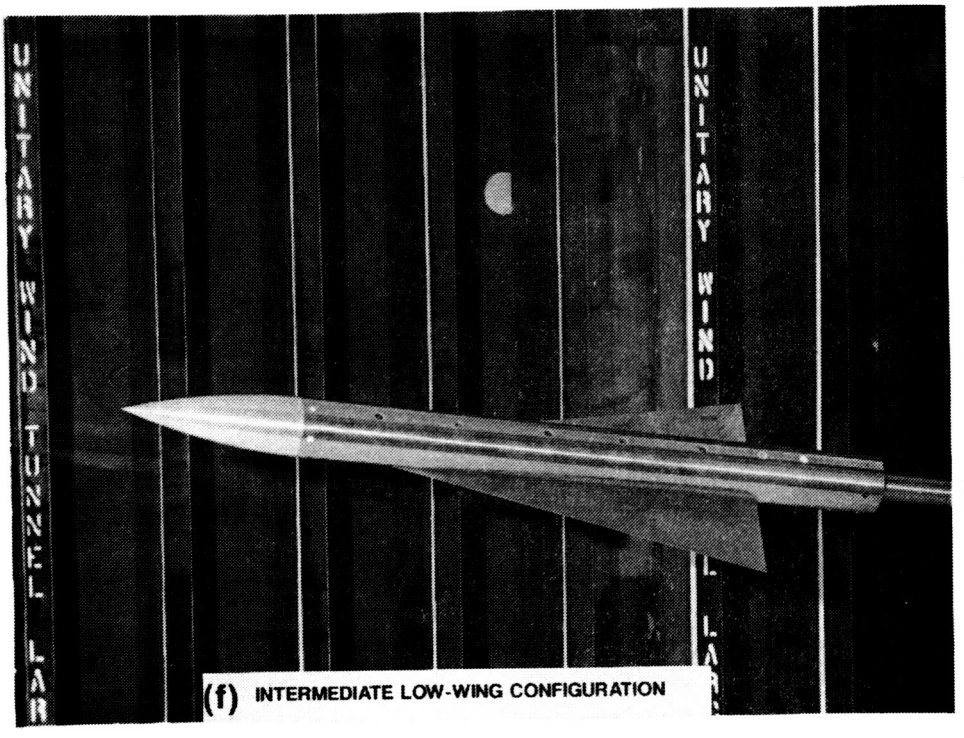

(f) INTERMEDIATE LOW-WING CONFIGURATION

Figure 2.- Continued

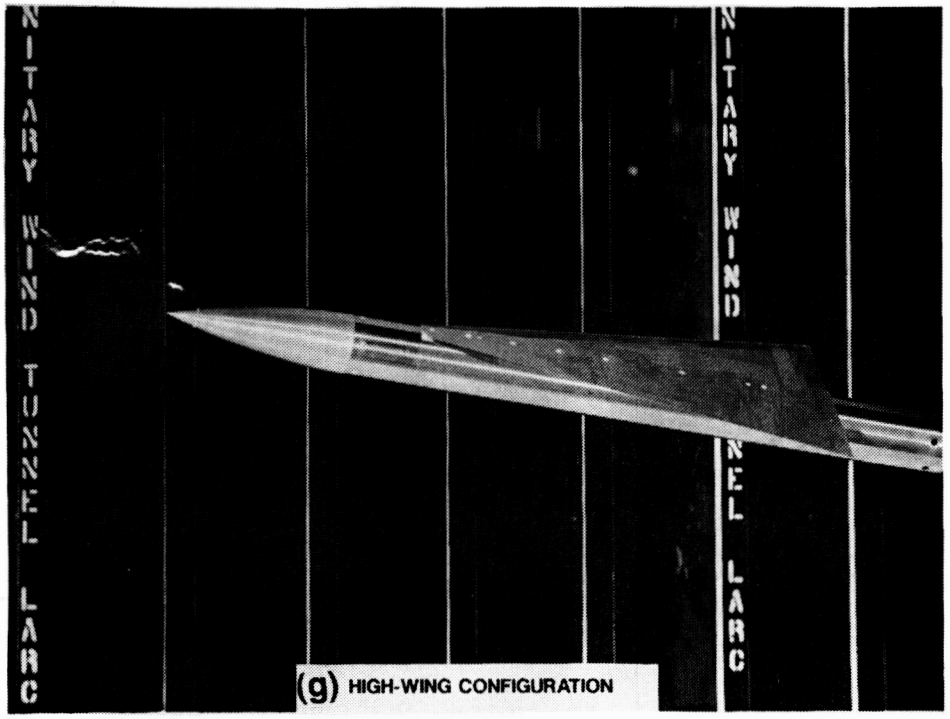

(g) HIGH-WING CONFIGURATION

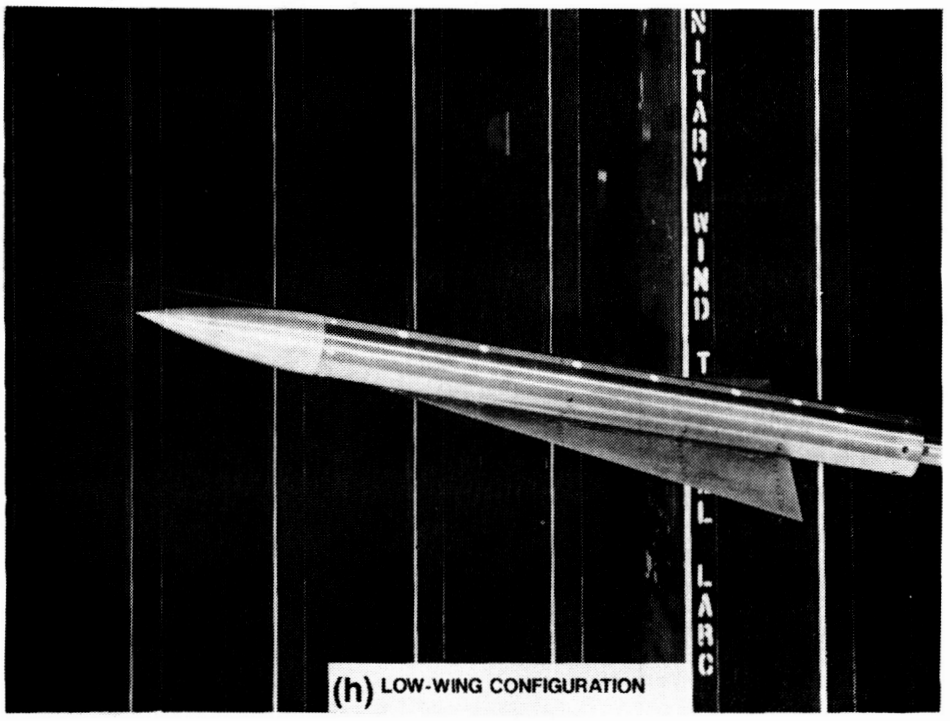

(h) LOW-WING CONFIGURATION

Figure 2.- Concluded

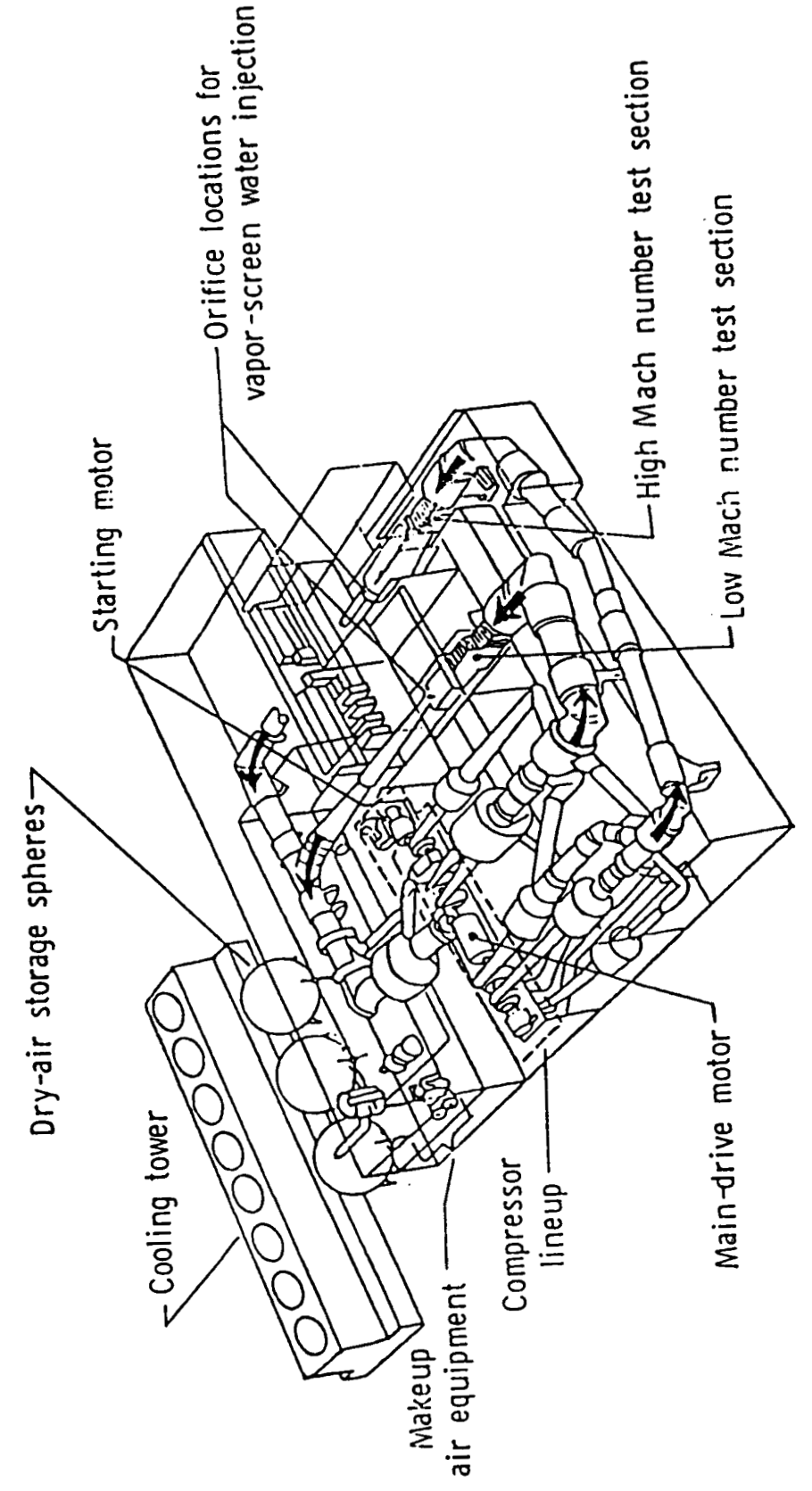

Figure 3.- Schematic Drawing of the Langley Unitary Plan Wind Tunnel (from Ref. 11)

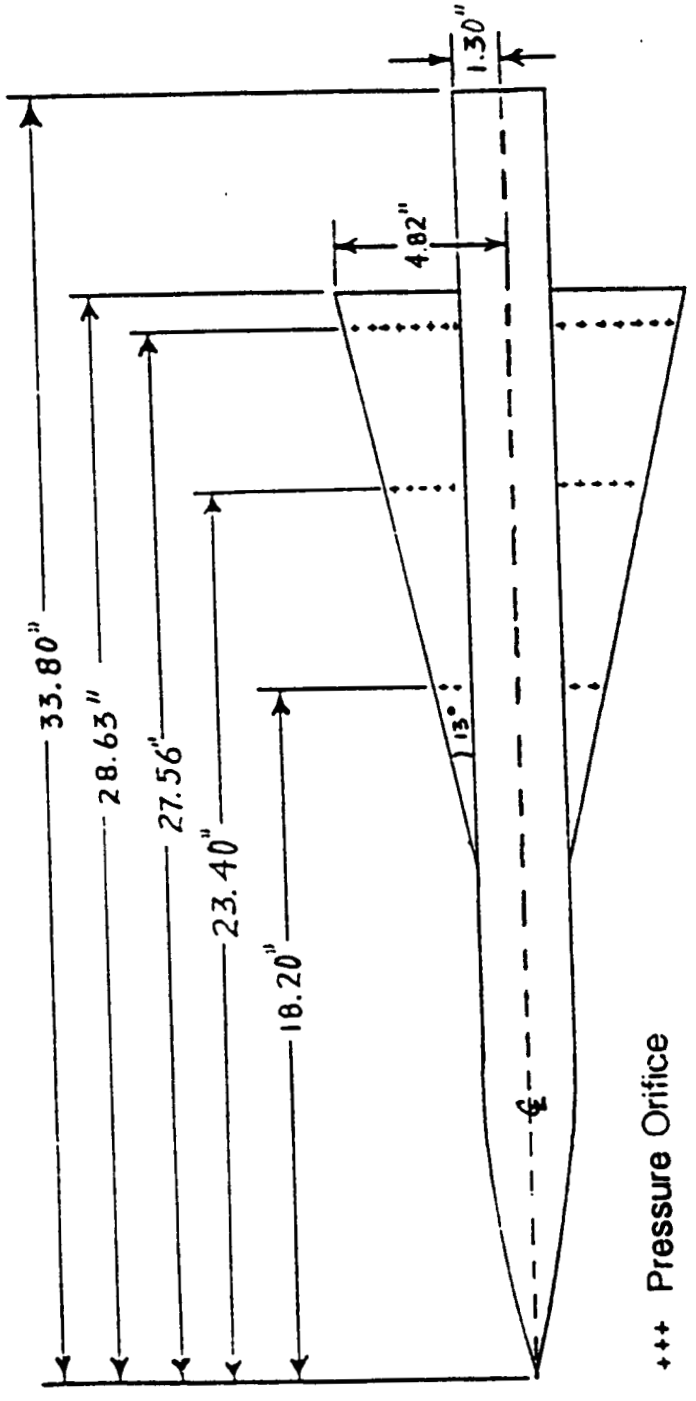

Figure 4.- Model Dimensions

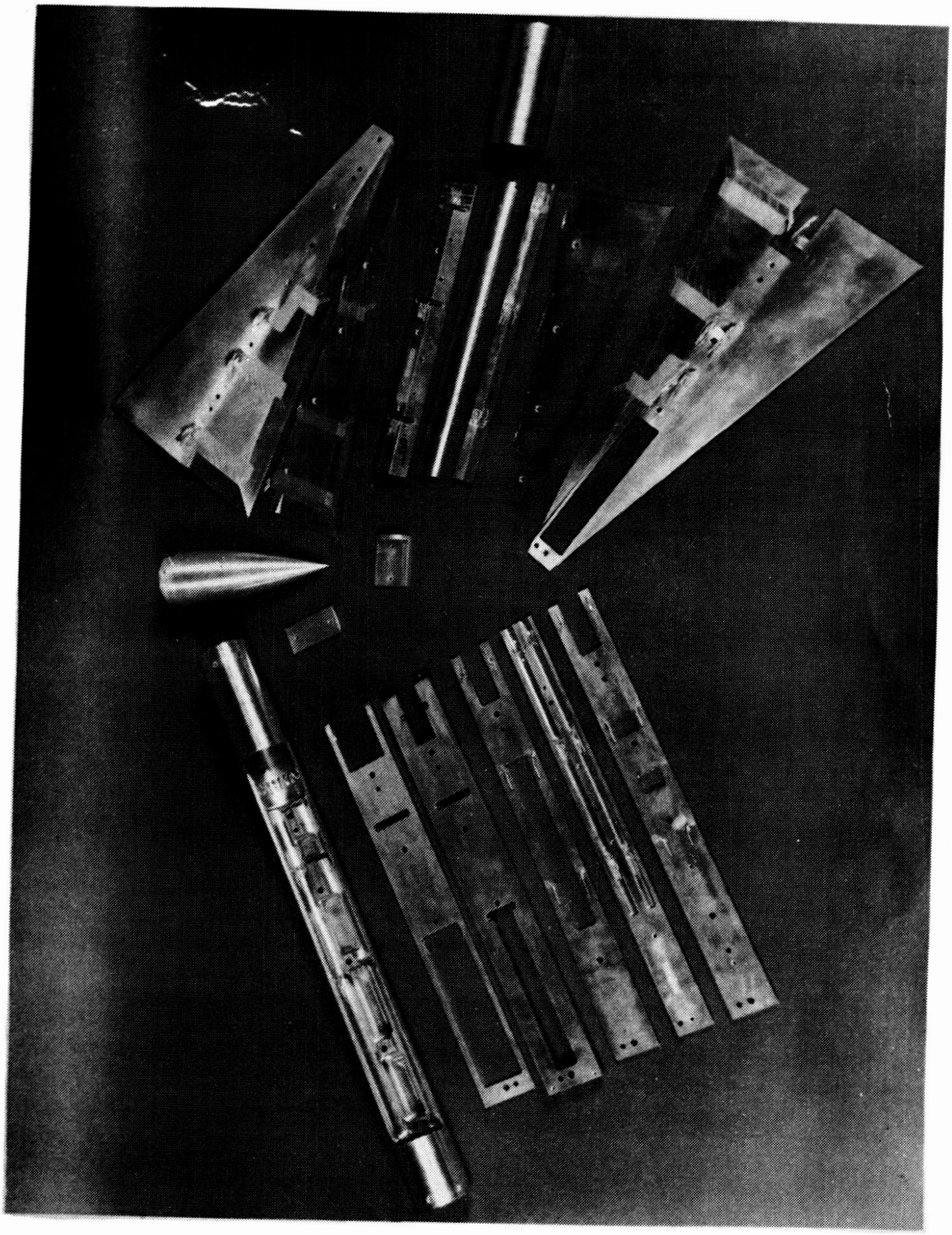

Figure 5.- Model Components

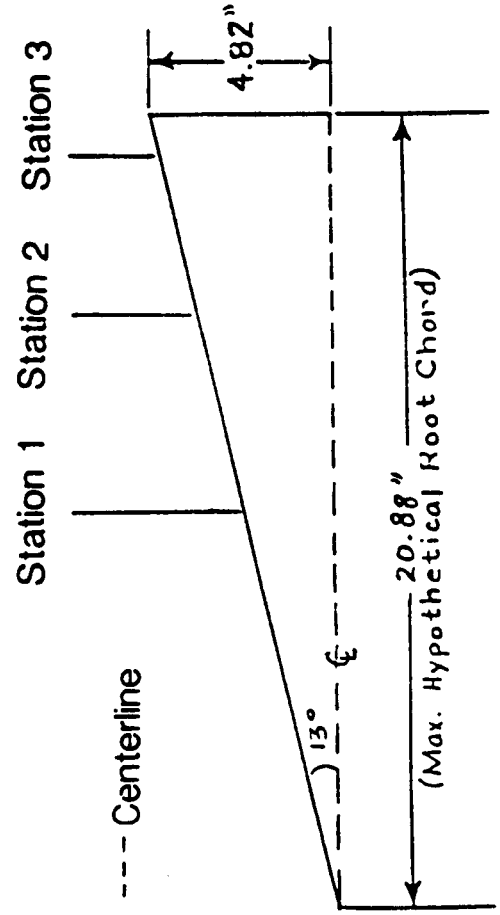

Figure 6.-Maximum Hypothetical Root Chord

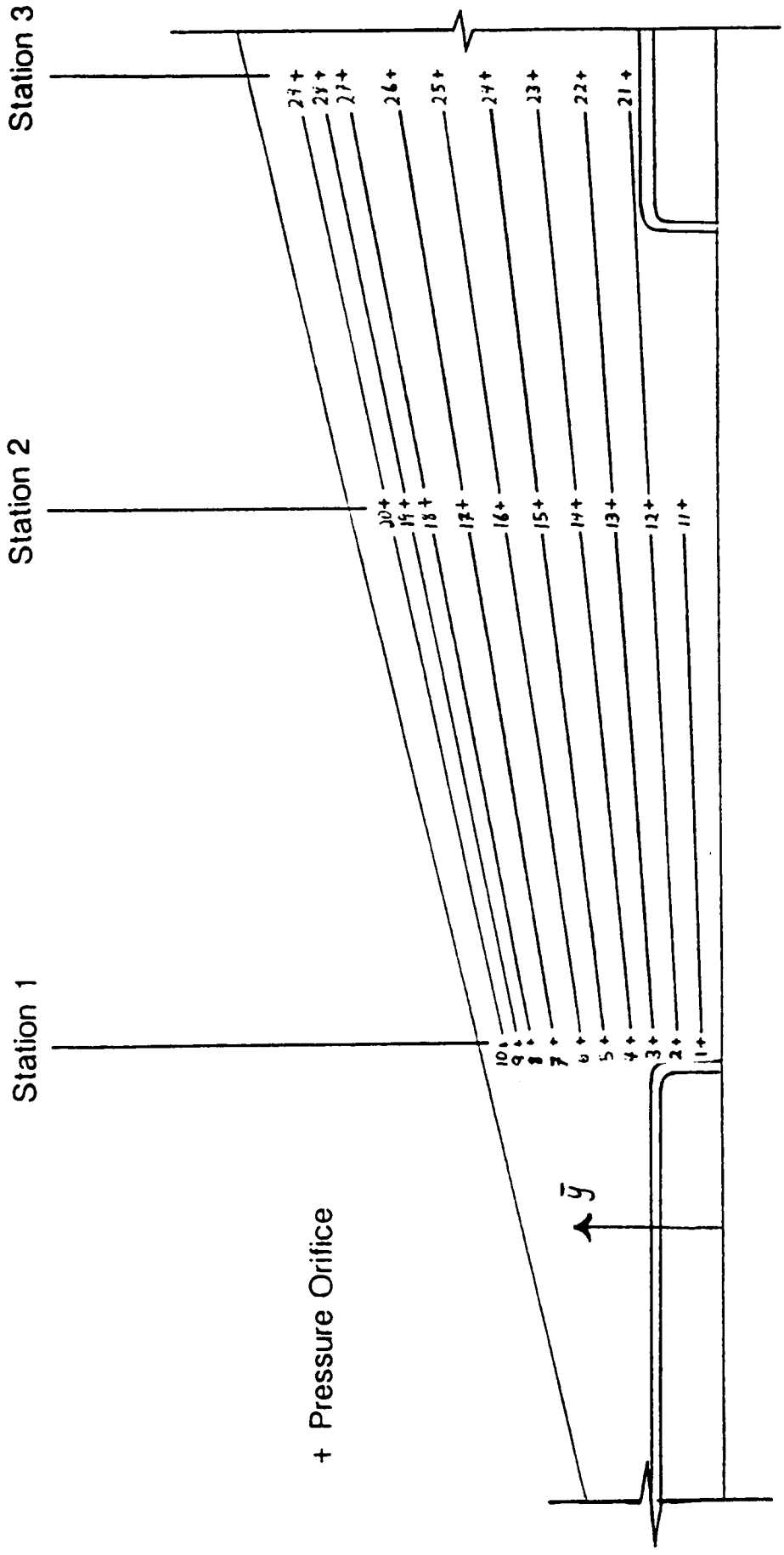

Figure 7.- Wing Pressure Orifice Locations

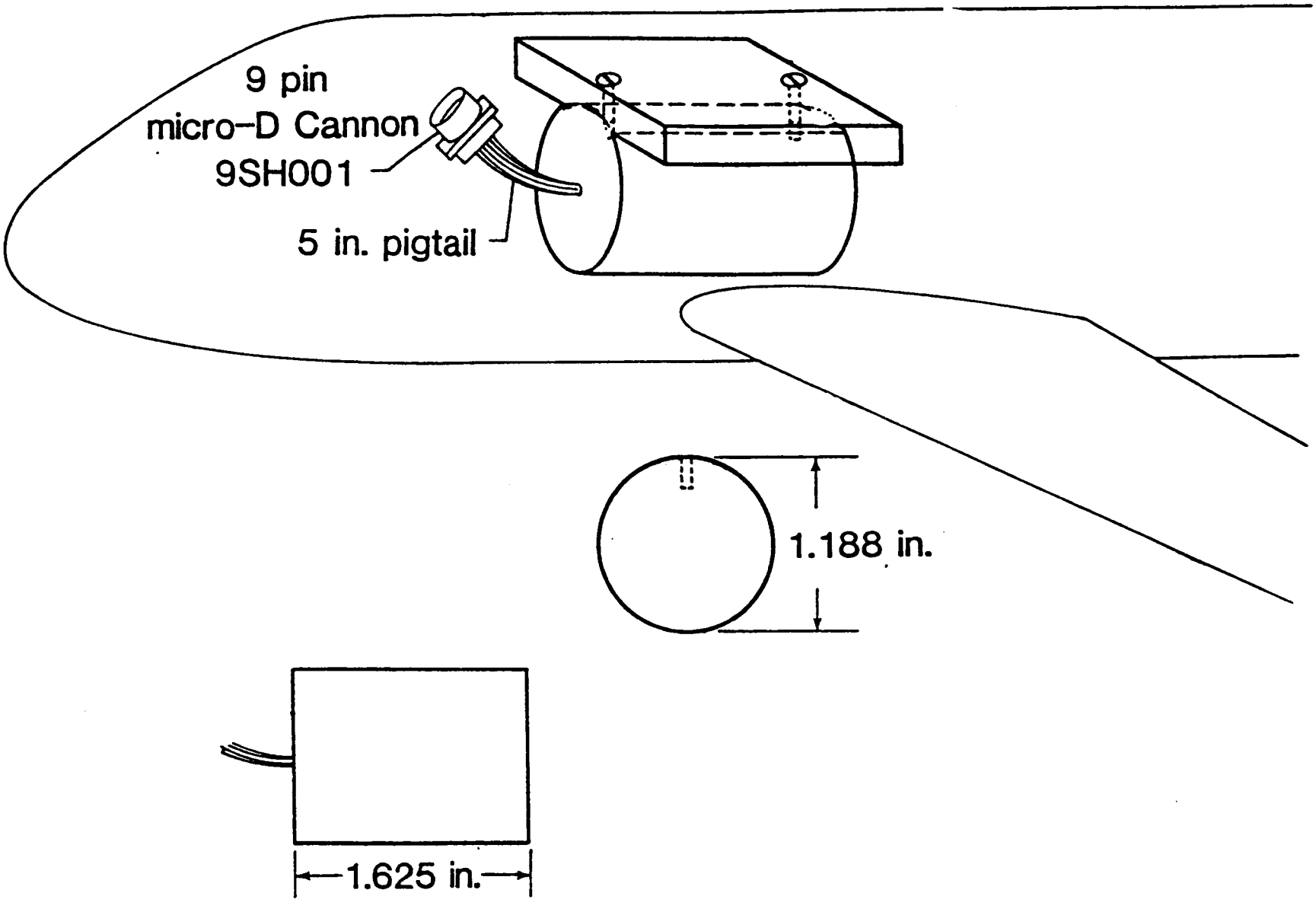

Figure 8.- Angle-of-Attack Sensor

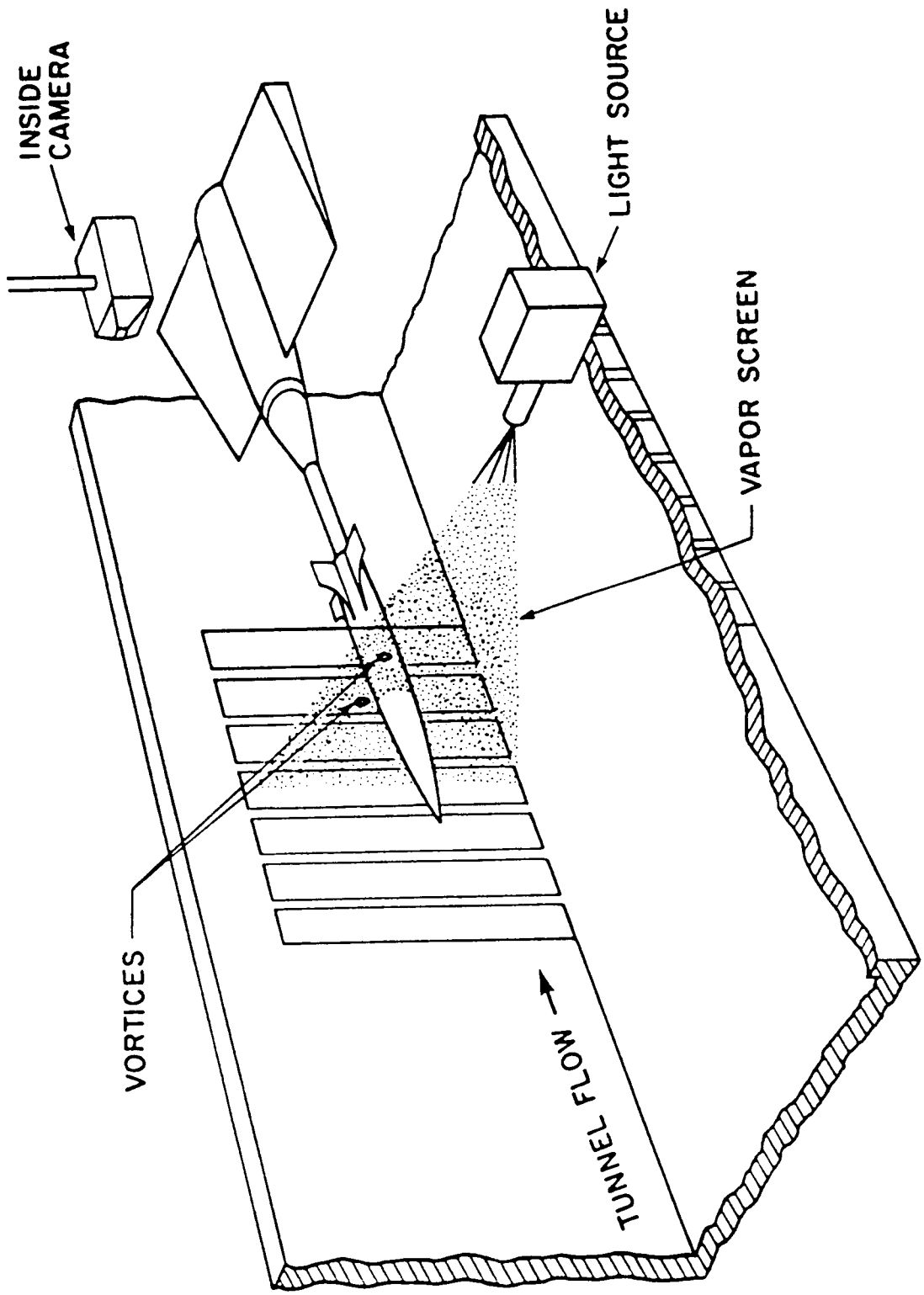

Figure 9.- Schematic Drawing of Vapor Screen Set-Up (from Ref. 11)

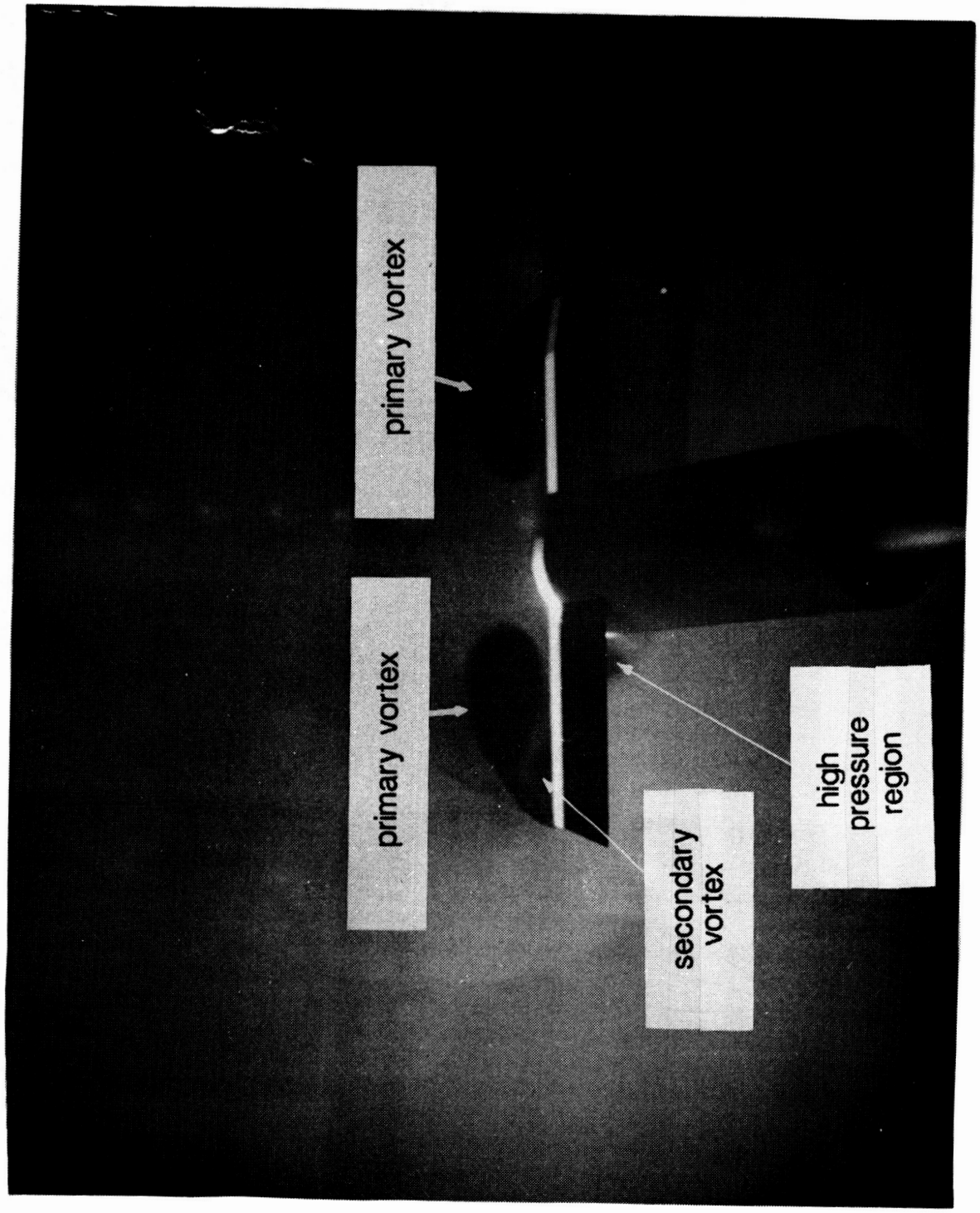

Figure 10.- Vapor Screen Photograph

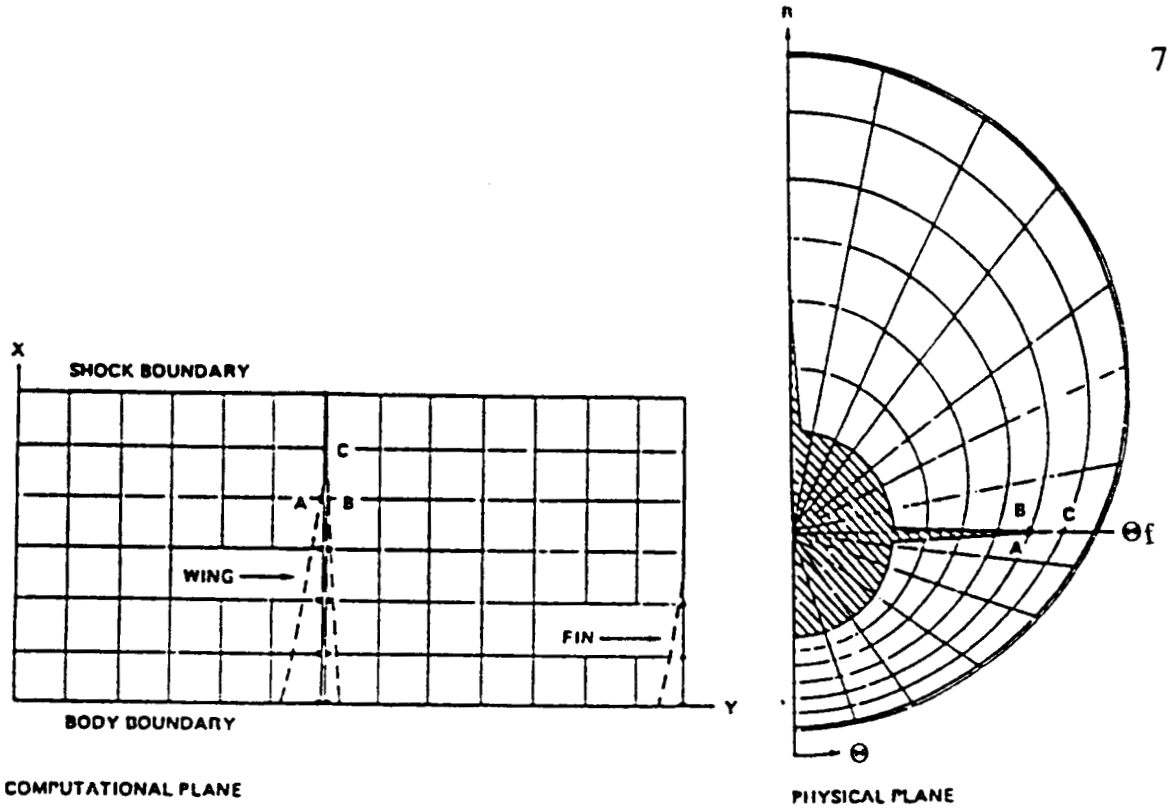

Figure 11.- SWINT Physical and Computational Coordinates

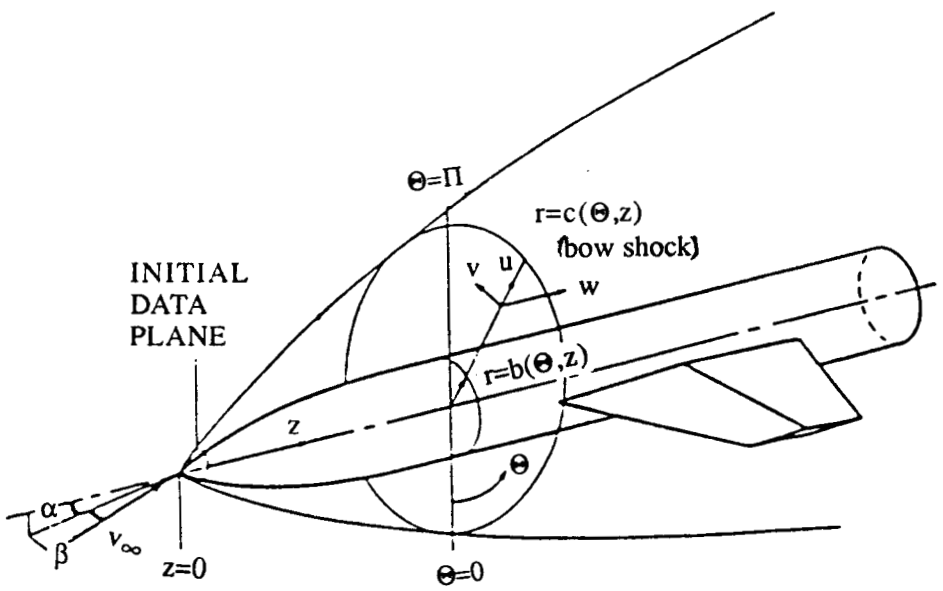

Figure 12.-Cylindrical Coordinate System
(the above figures are from Ref. 14)

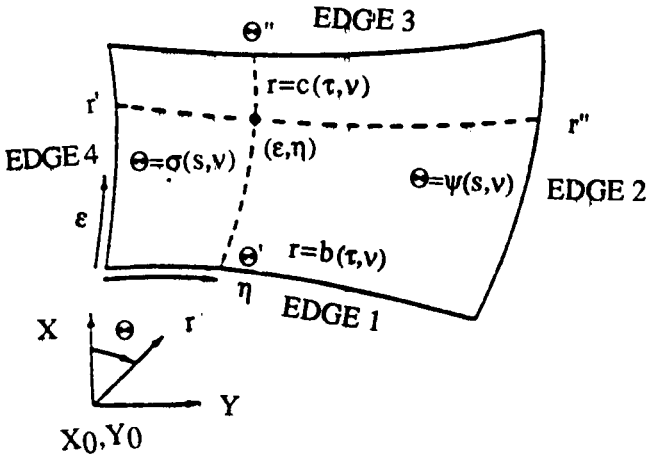

Figure 13.- Zone Edge and Corner Numbering Scheme

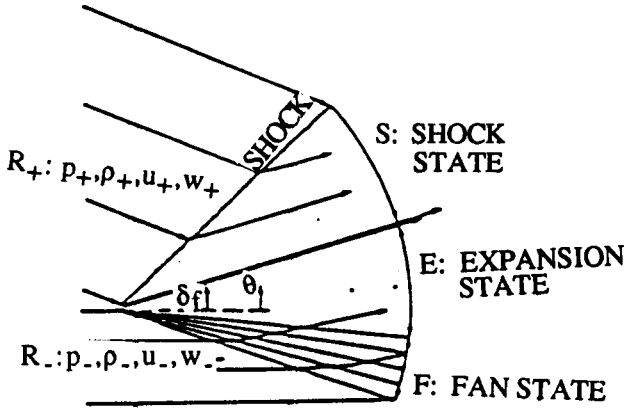

Figure 14.- Supersonic Riemann Problem

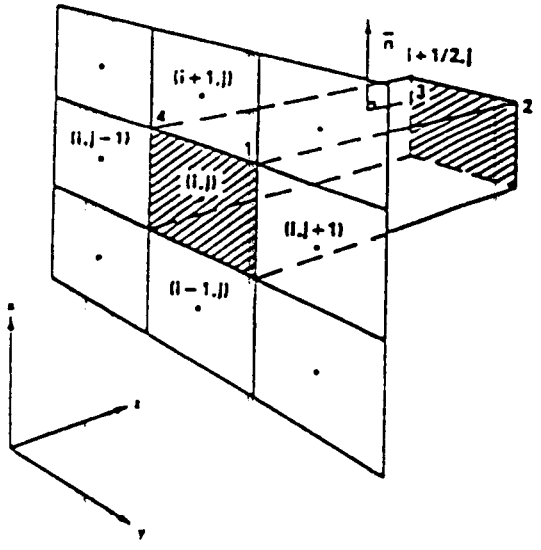

Figure 15.- Control Volume Nomenclature

(the above figures are from Ref. 12)

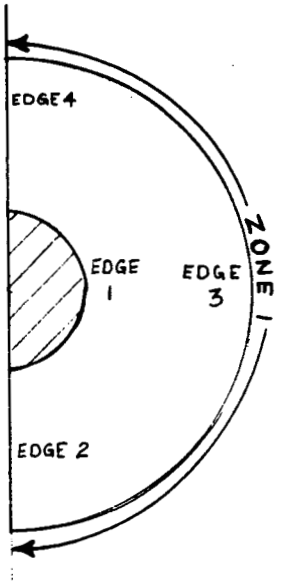

(a) One-Zone Procedure

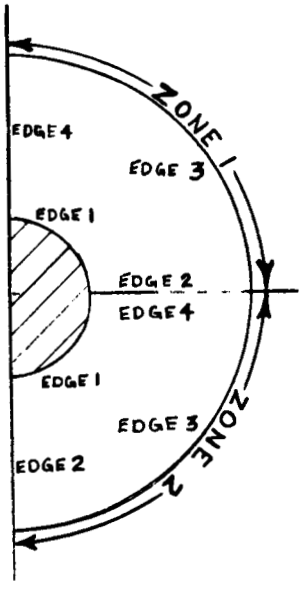

(b) Two-Zone Procedure

Figure 16.- ZEUS Zone Descriptions

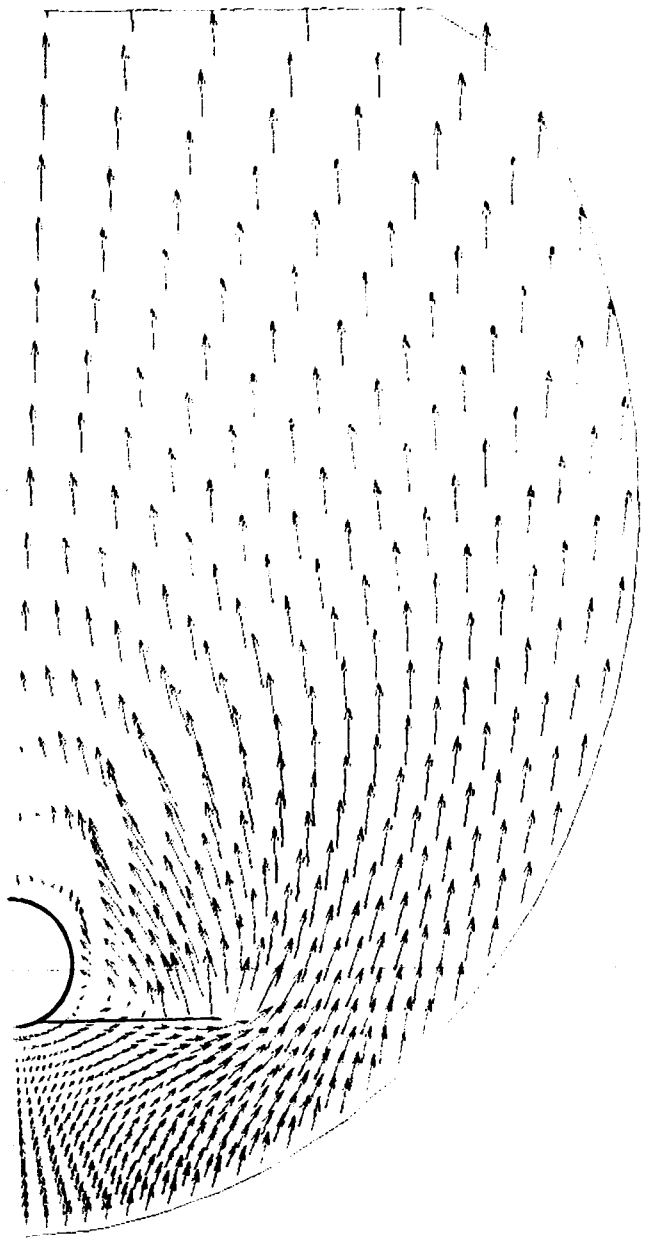

(a)

intermediate low-wing

M = 2.86

$\alpha = 20°$

station 3

Figure 17. - Velocity Vector Crossflow Plot

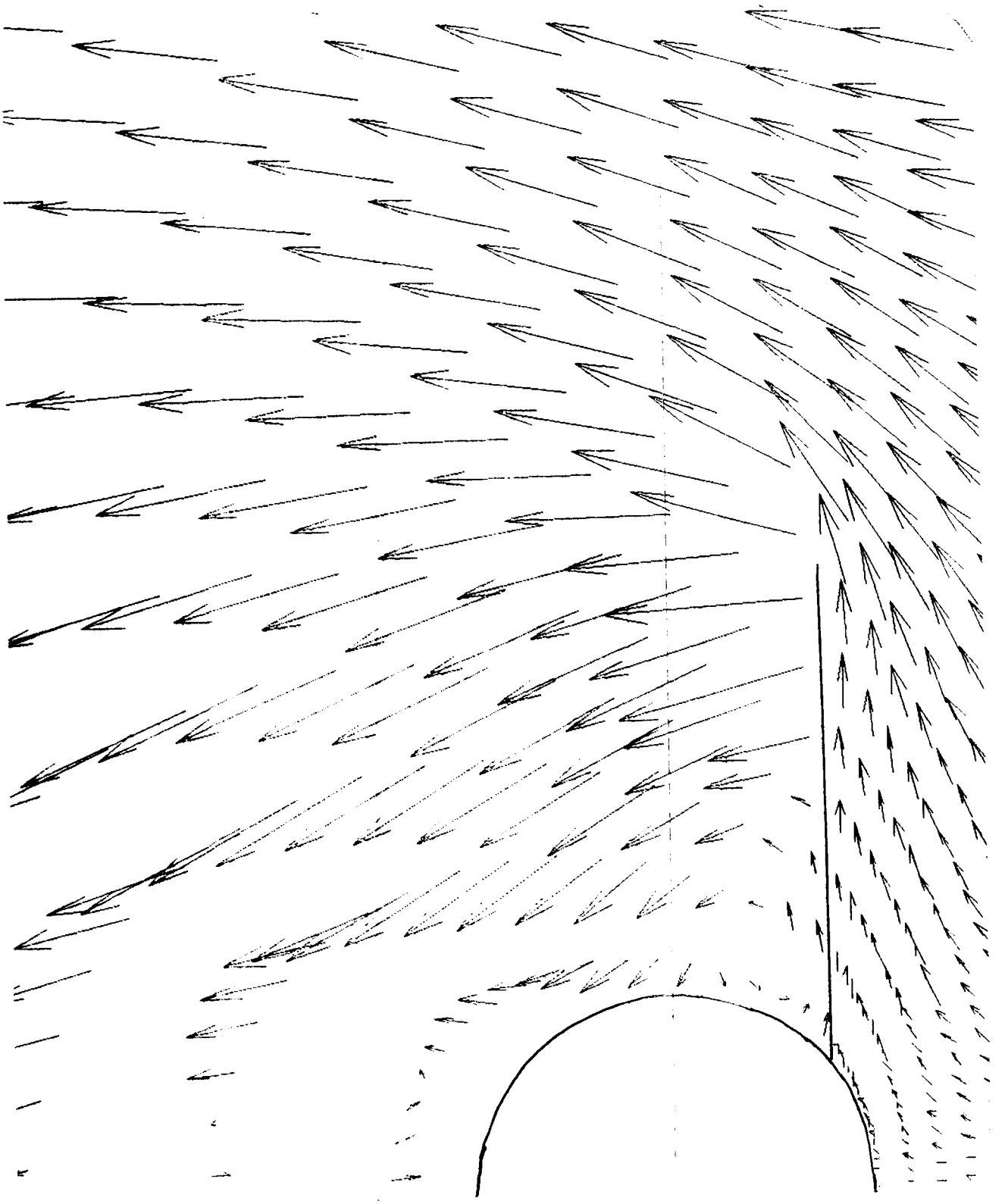

Figure 17. - Concluded

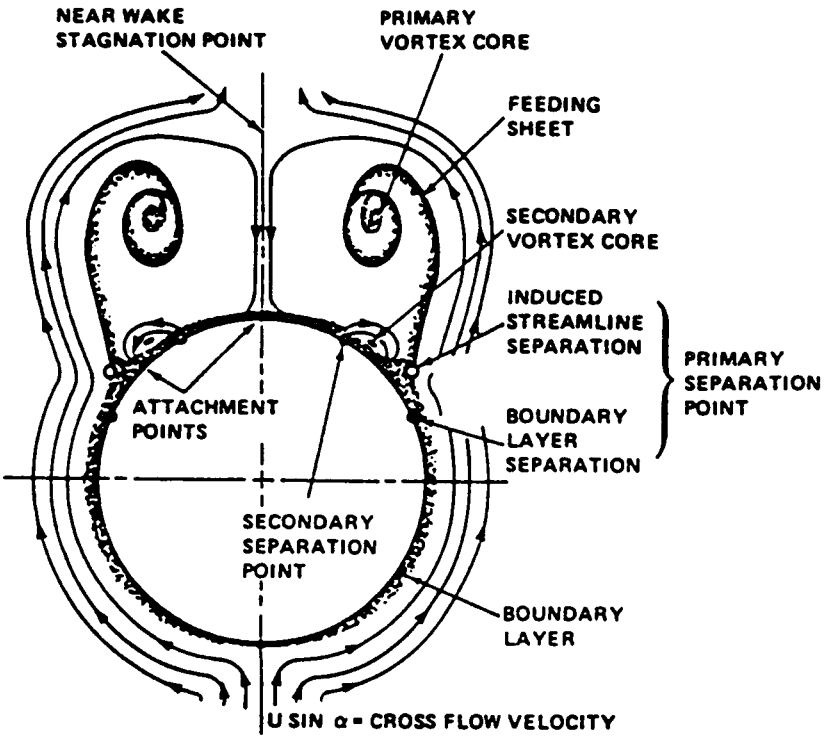

Figure 18.- Symmetric Flow Field for Body Alone
(from Ref. 20)

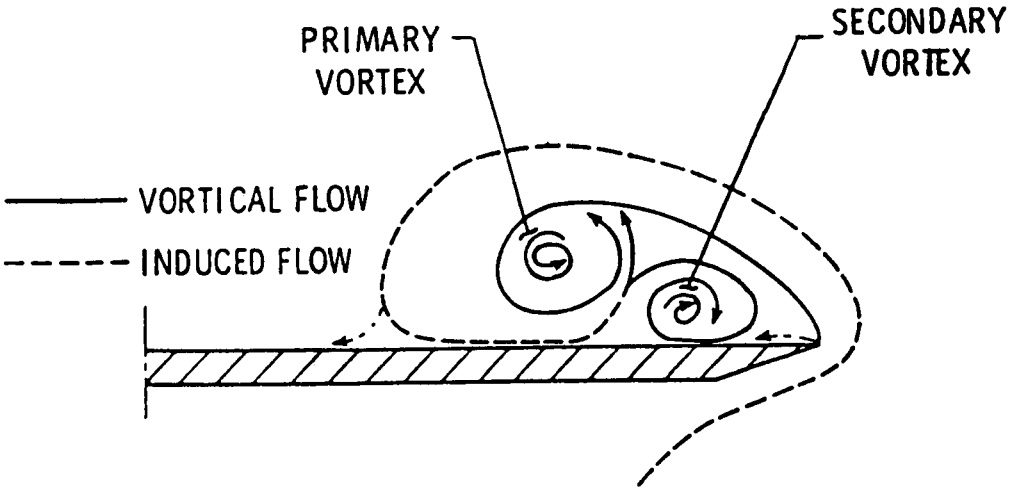

Figure 19.- Classical Leading Edge Vortex
(from Ref. 16)

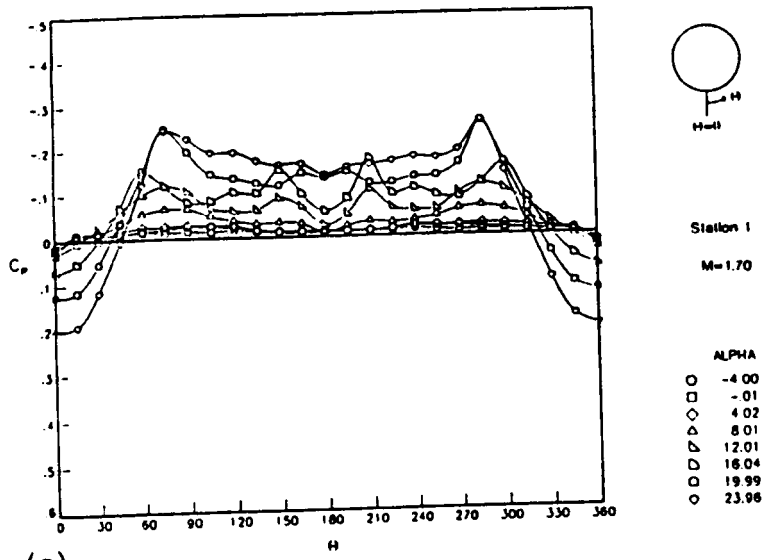

(a)

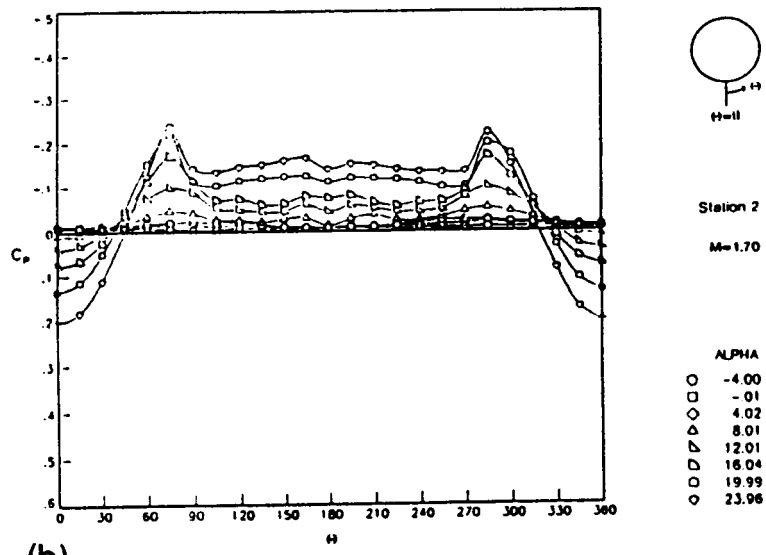

(b)

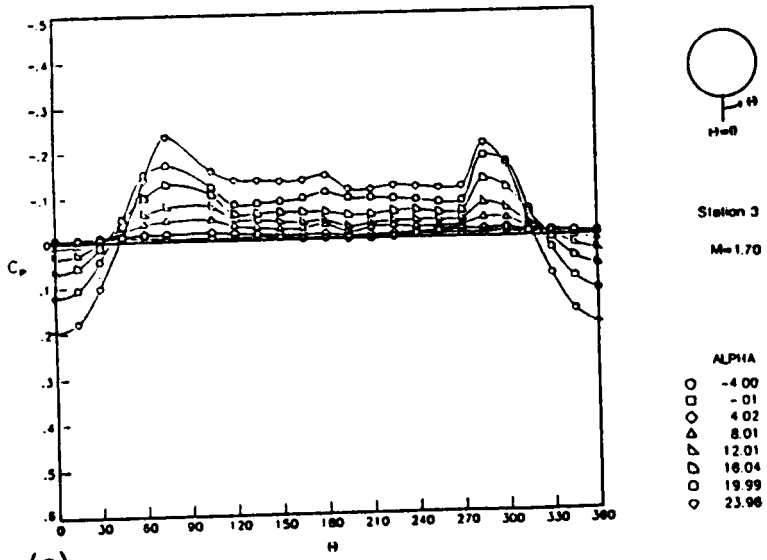

(c)

Figure 20.- Experimental Pressures for Body Alone Configuration

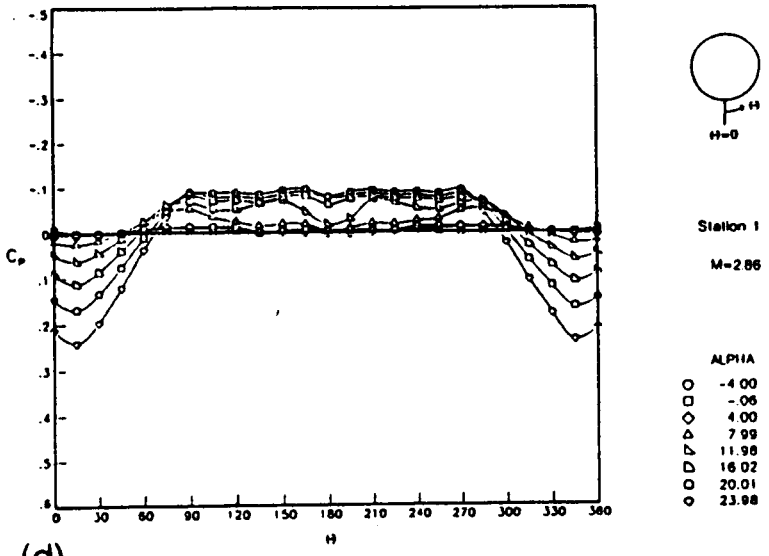

(d)

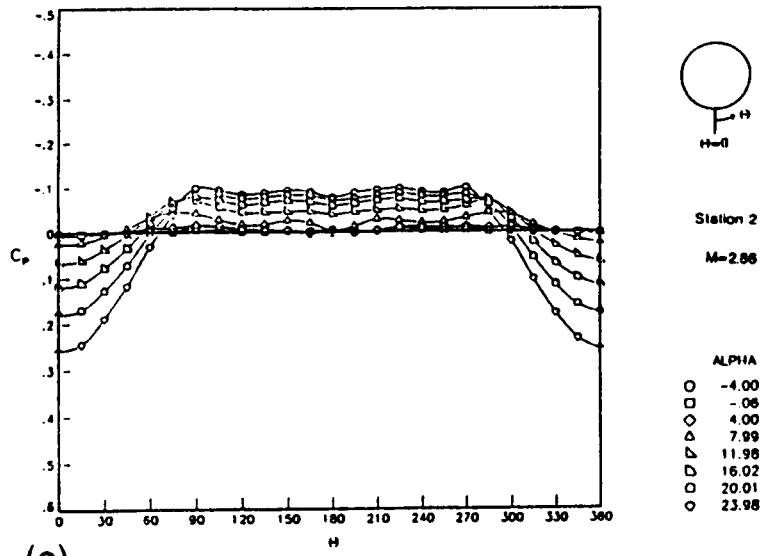

(e)

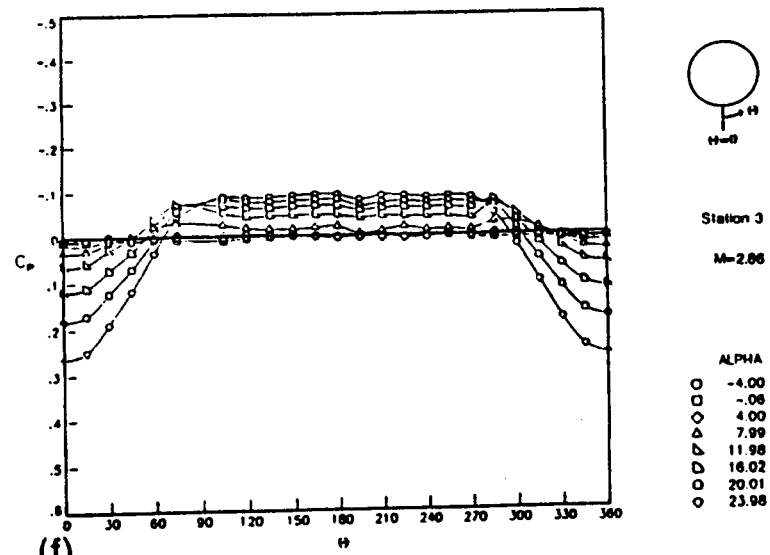

(f)

Figure 20.-Concluded

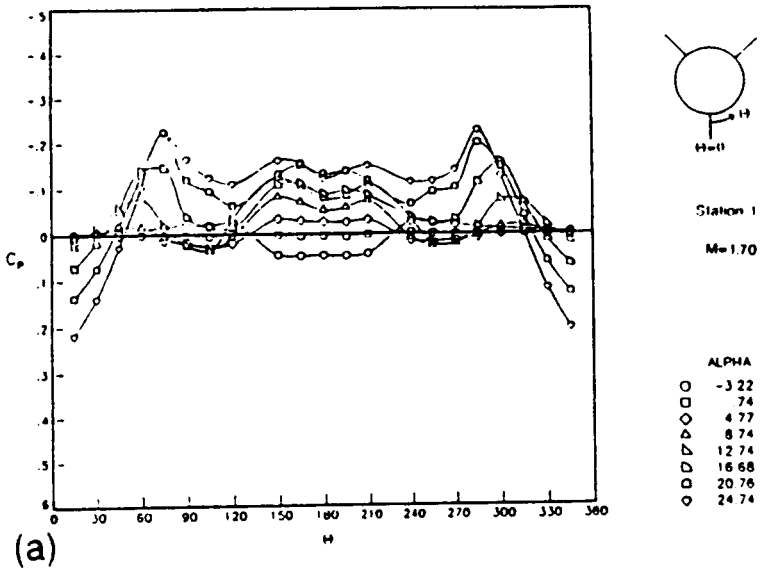

(a)

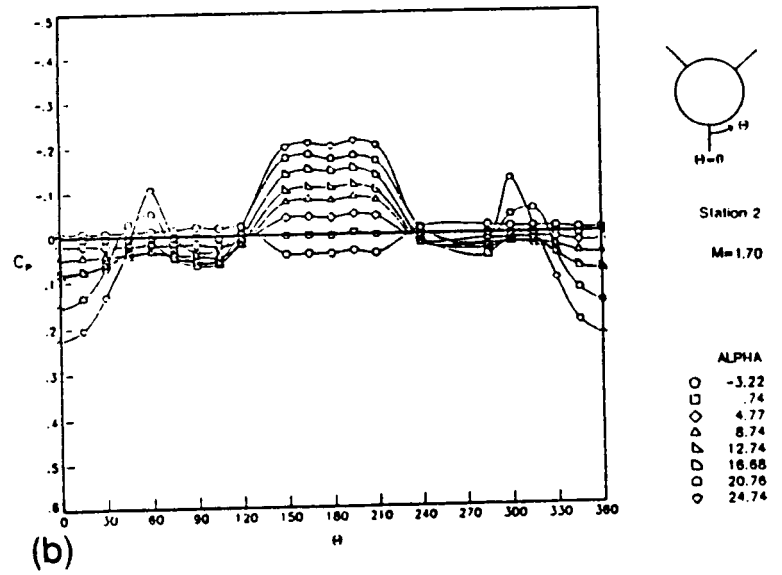

(b)

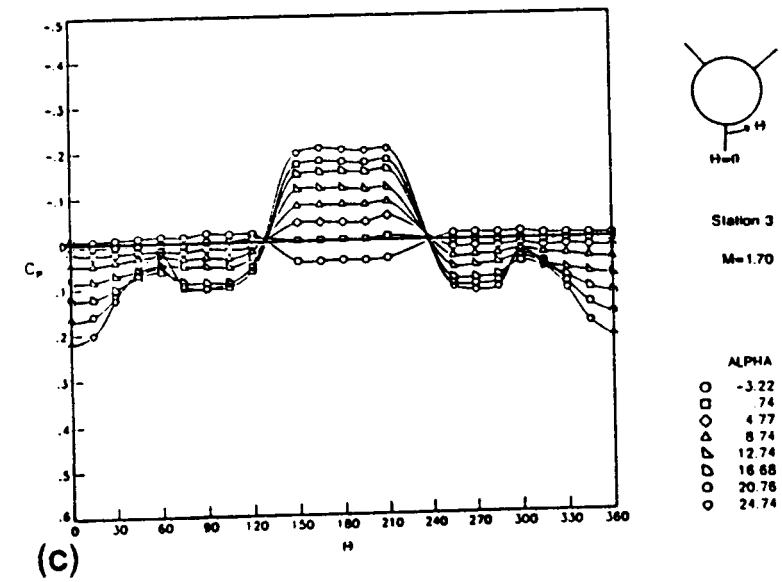

(c)

Figure 21.- Experimental Pressures for Bent Wing Configuration

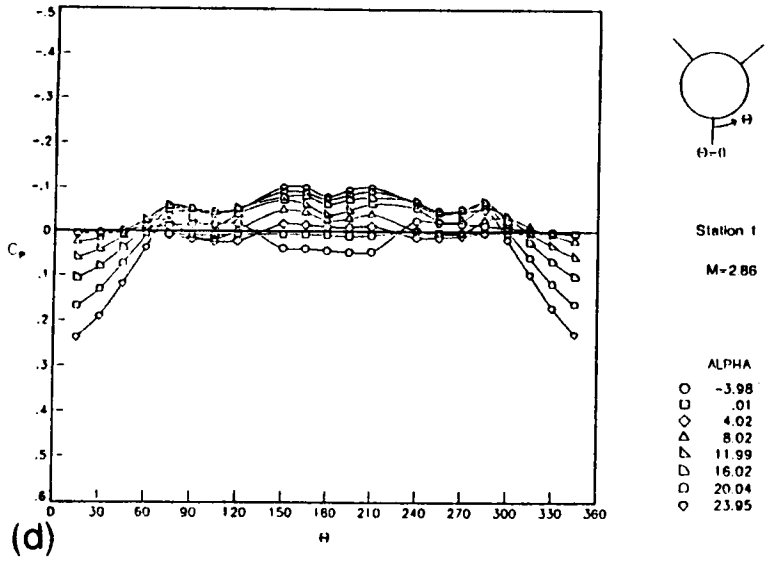

(d)

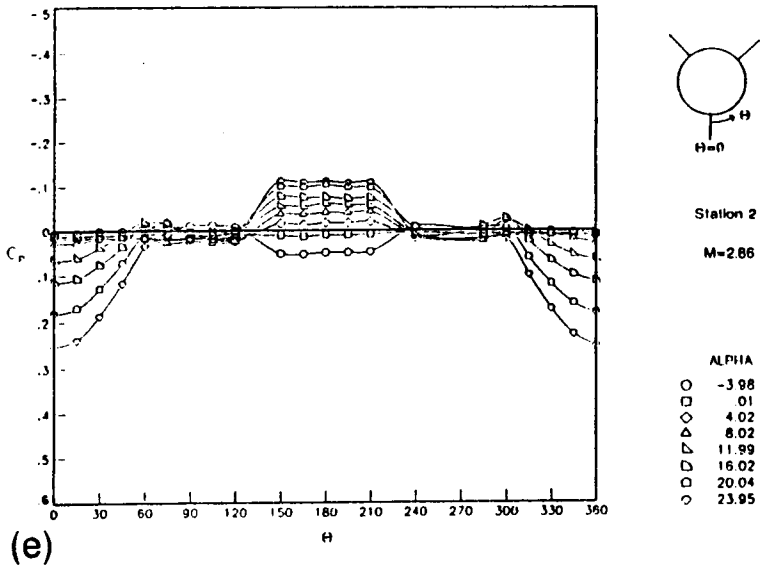

(e)

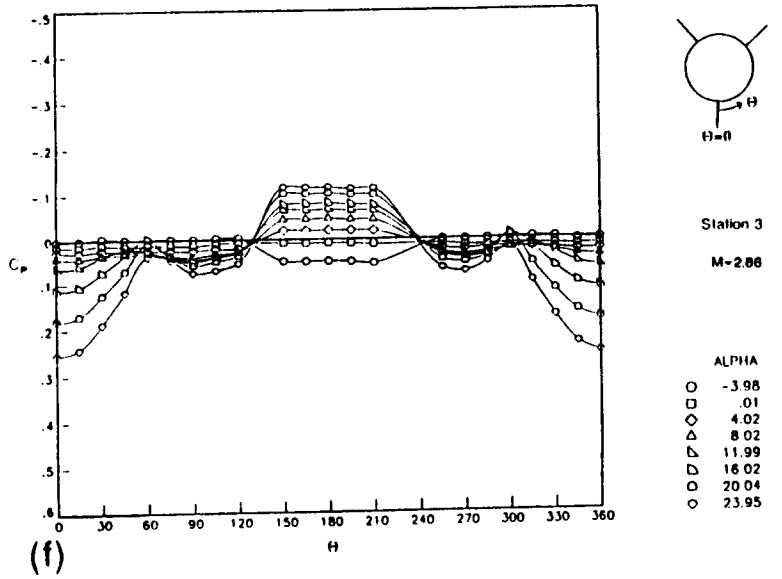

(f)

Figure 21.- Continued

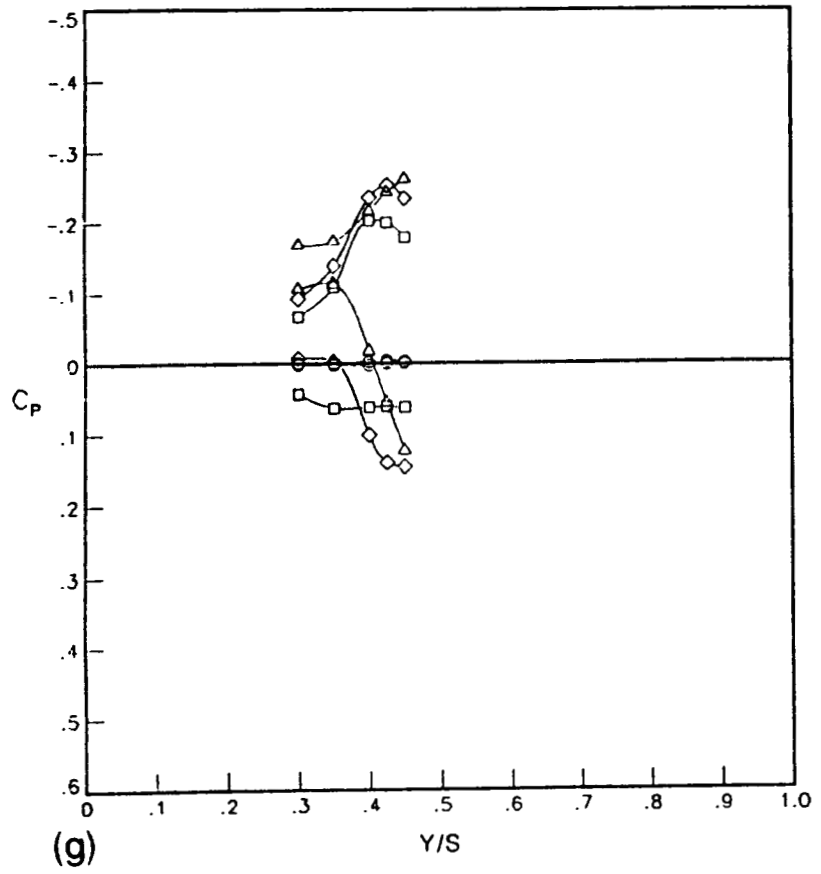

(g)

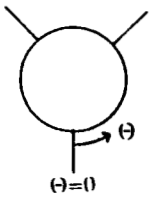

Station 1

M=1.70

ALPHA

○ .74
□ 8.74
◇ 16.68
△ 24.74

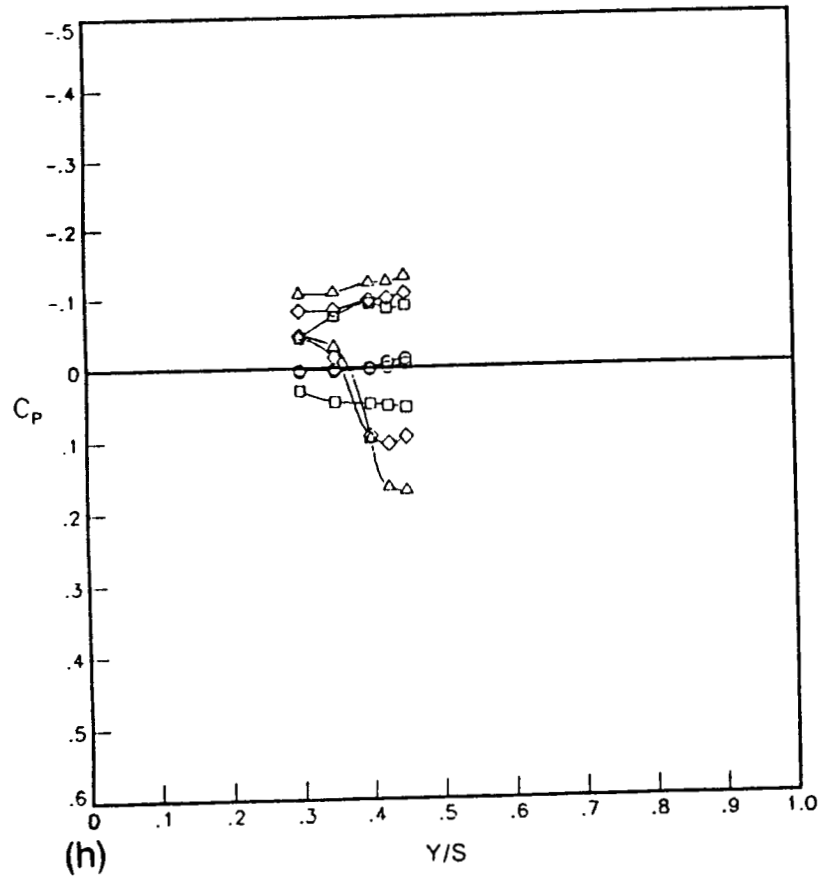

(h)

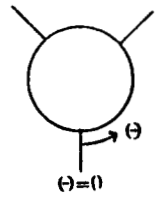

Station 1

M=2.86

ALPHA

○ .01
□ 8.02
◇ 16.02
△ 23.95

Figure 21.- Continued

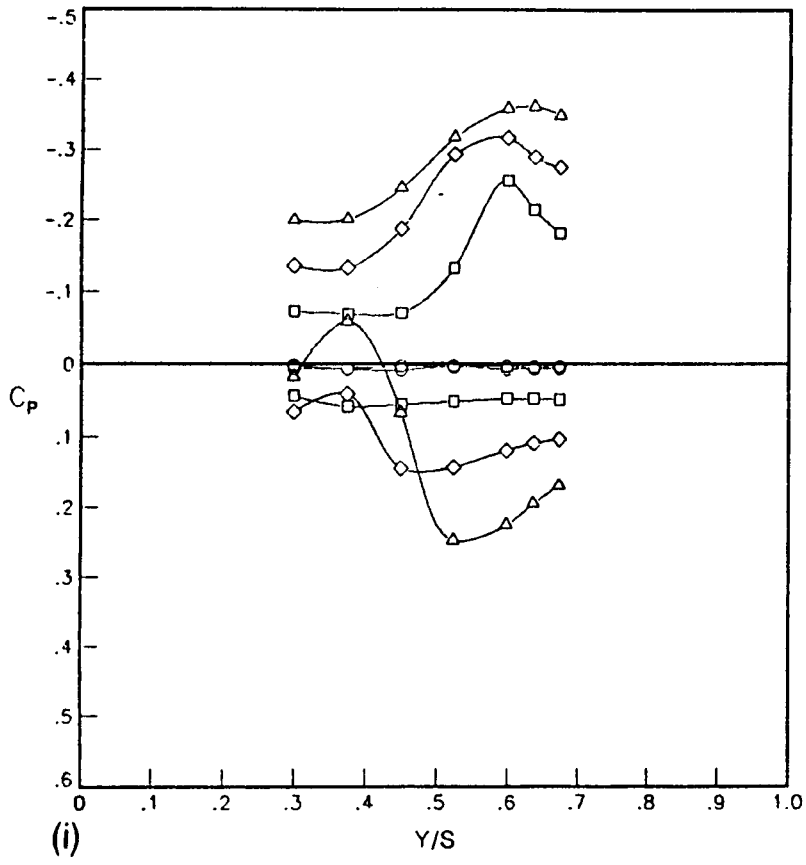

(i)

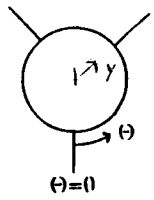

Station 2

M=1.70

ALPHA

○	.74
□	8.74
◇	16.68
△	24.74

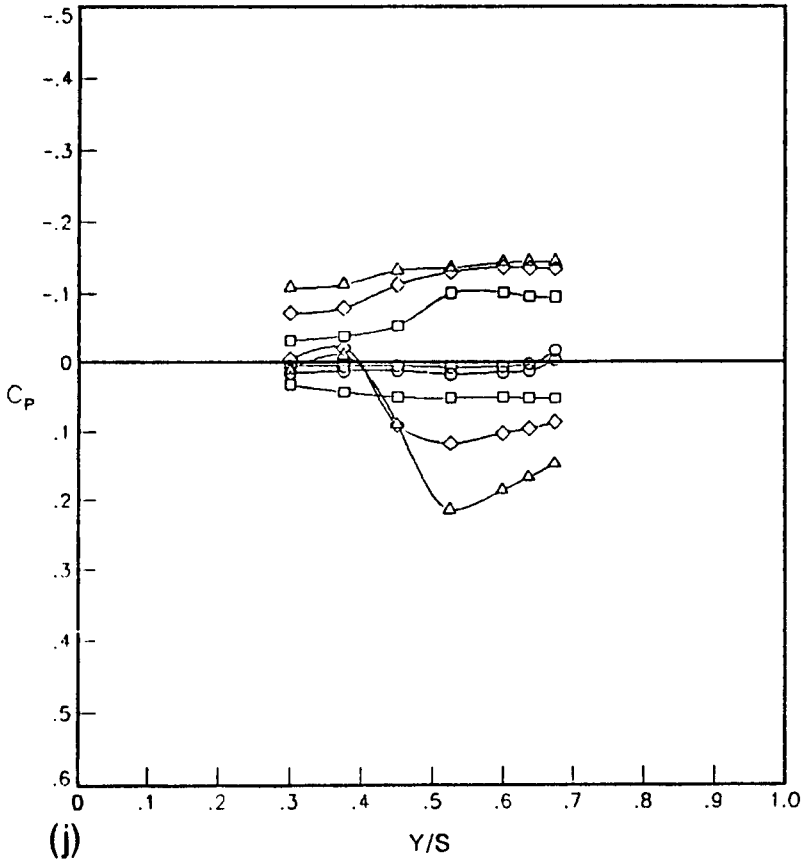

(j)

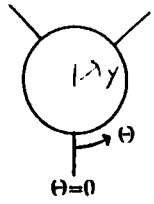

Station 2

M=2.86

ALPHA

○	.01
□	8.02
◇	16.02
△	23.95

Figure 21.- Continued

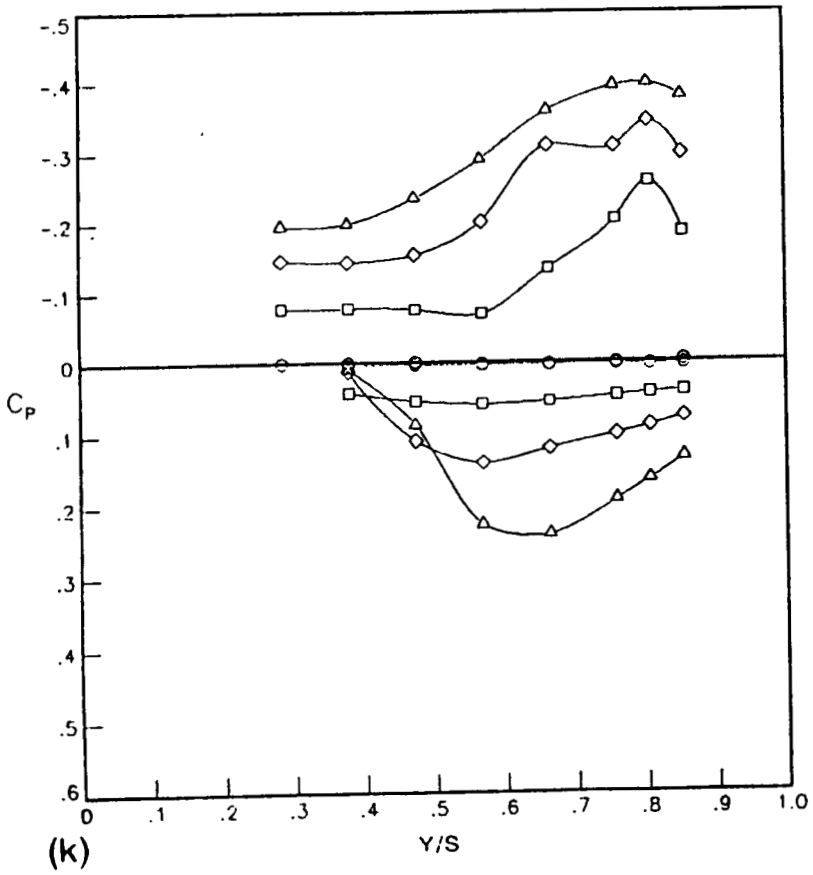

(k)

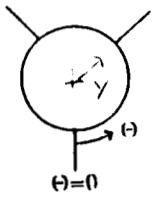

Station 3

M=1.70

ALPHA

○ .74
□ 8.74
◇ 16.68
△ 24.74

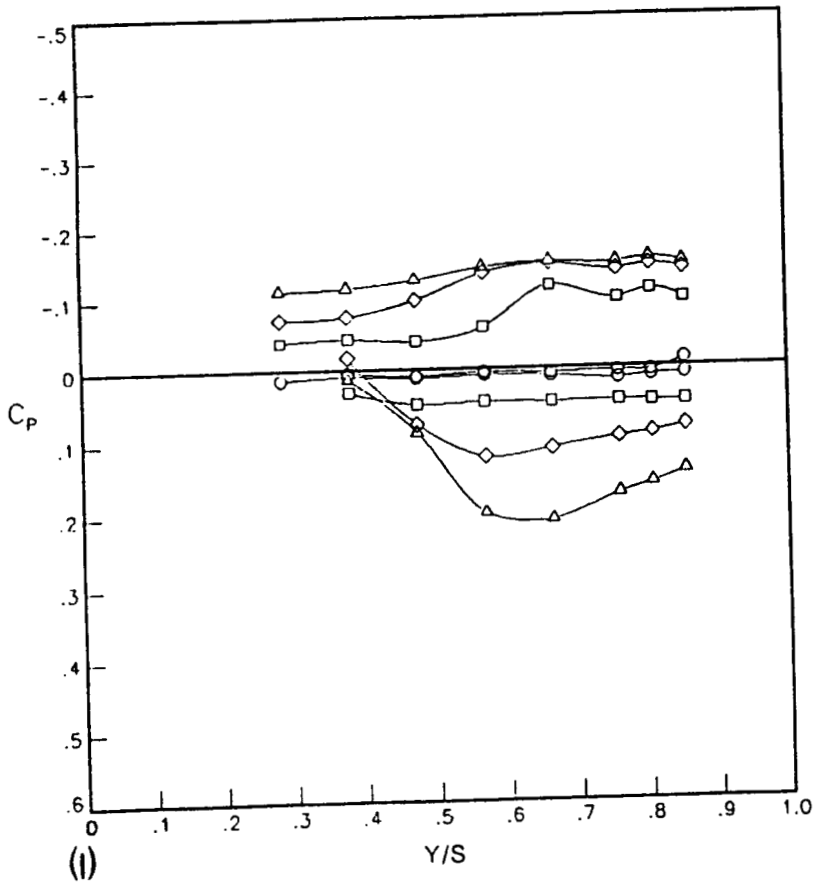

(l)

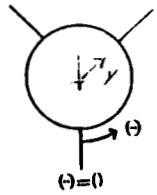

Station 3

M=2.86

ALPHA

○ .01
□ 8.02
◇ 16.02
△ 23.95

Figure 21.-Concluded

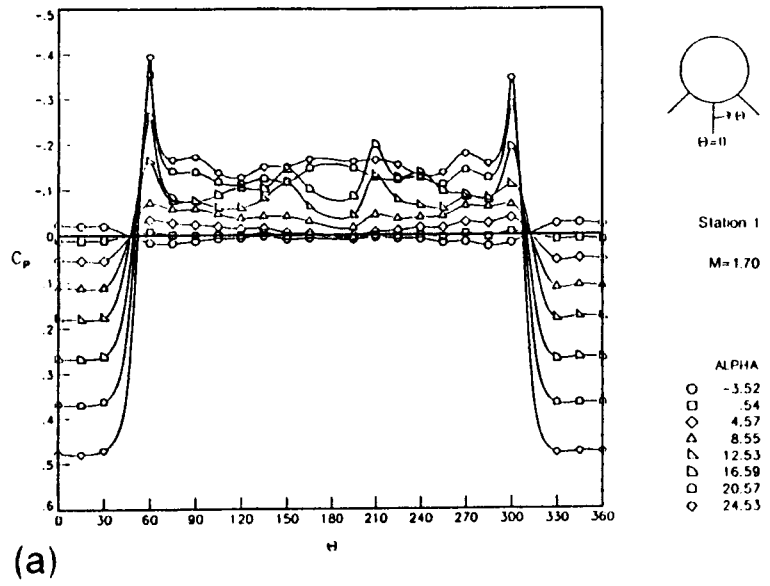

(a)

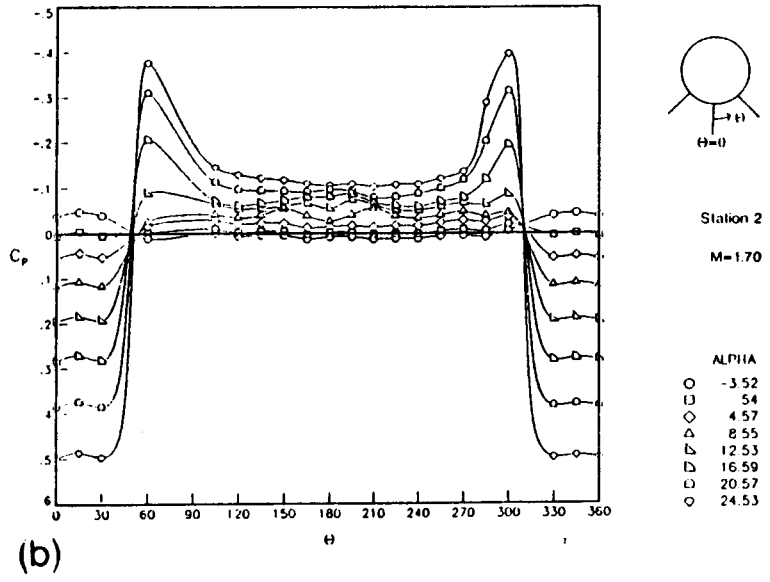

(b)

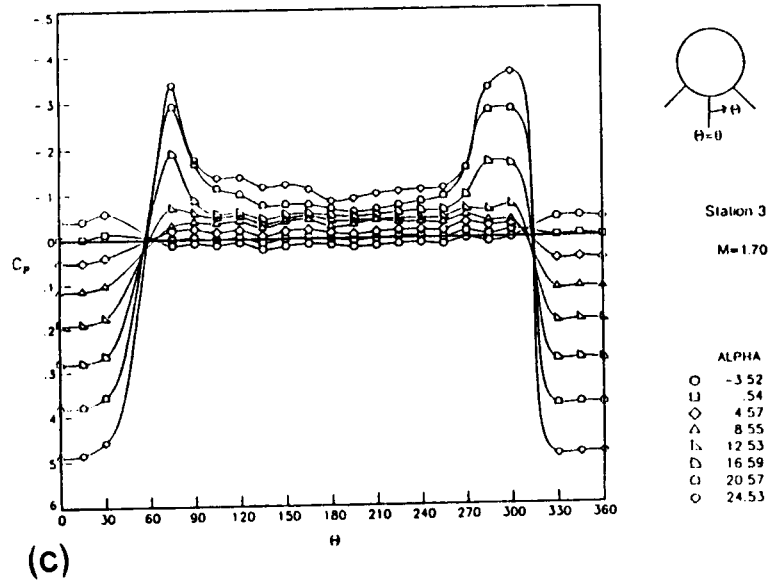

(c)

Figure 22.- Experimental Pressures for Inverted Bent-Wing

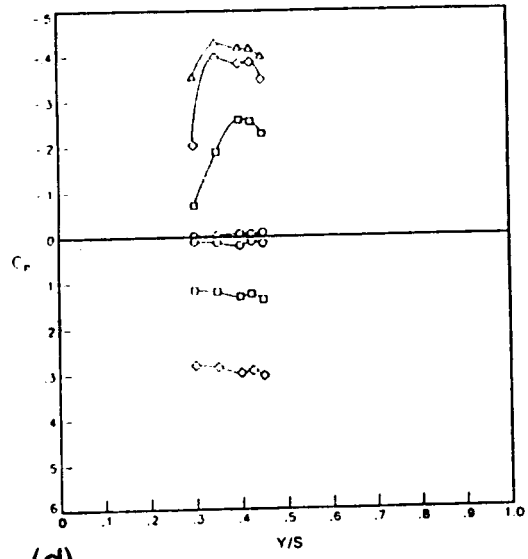

(d)

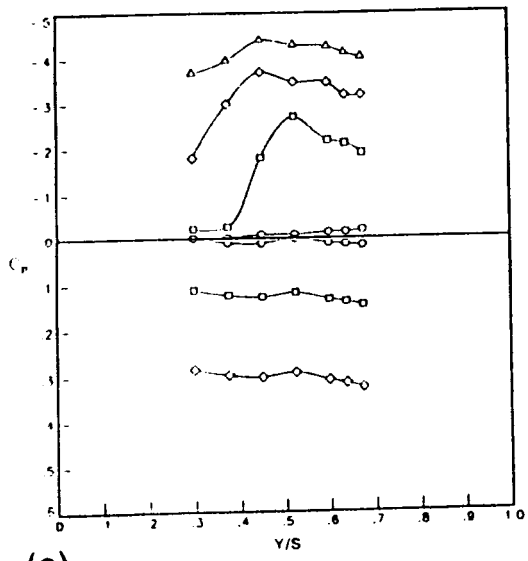

(e)

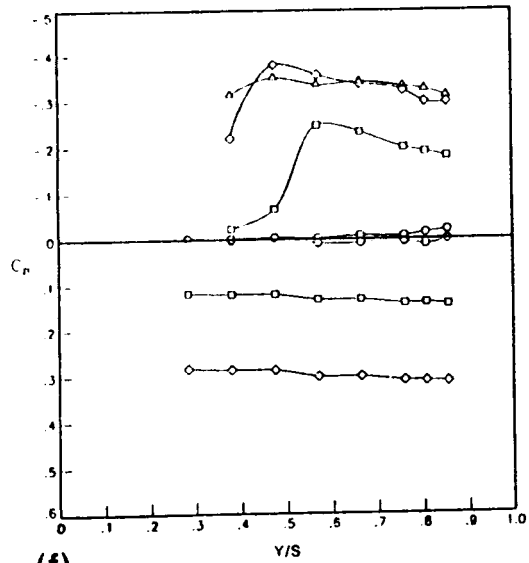

(f)

Figure 22.- Continued

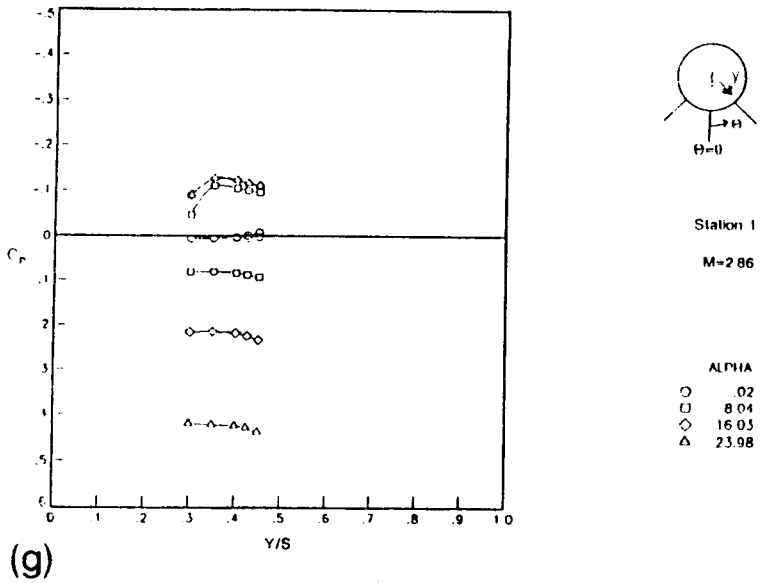

(g)

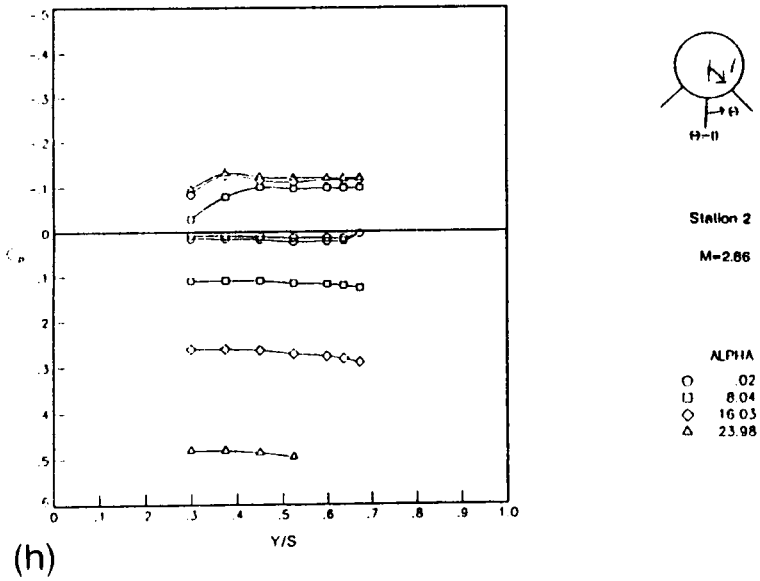

(h)

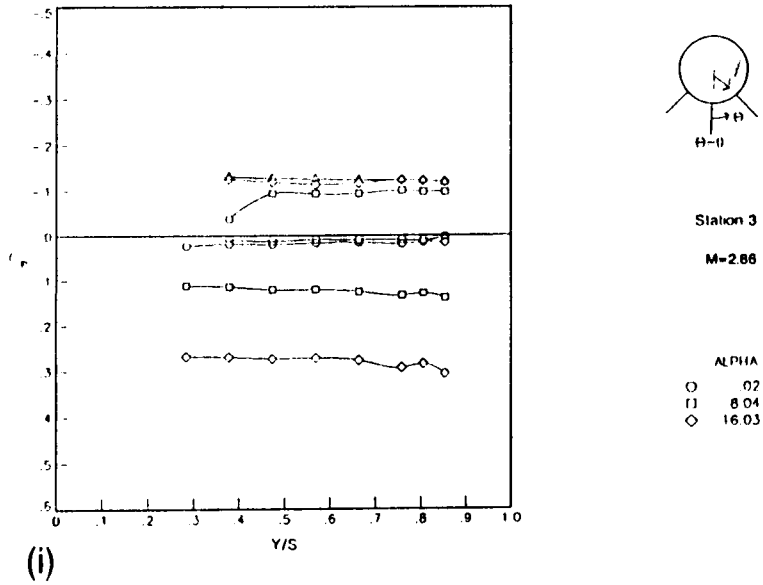

(i)

Figure 22.-Concluded

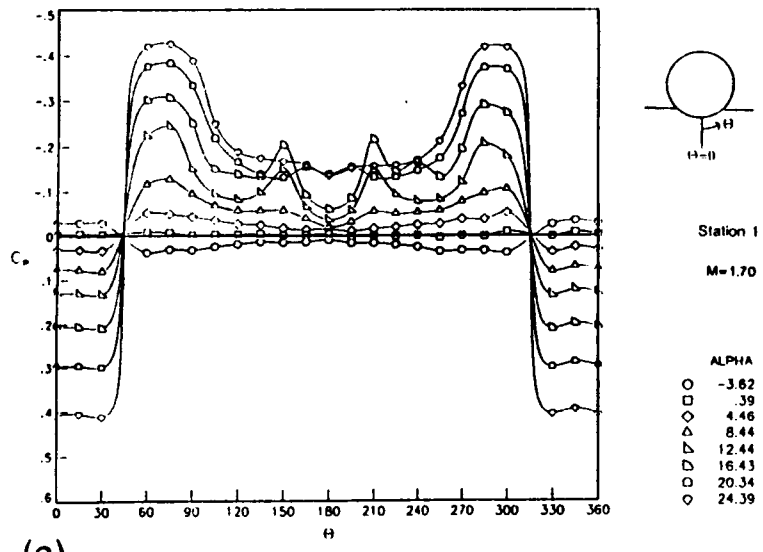

(a)

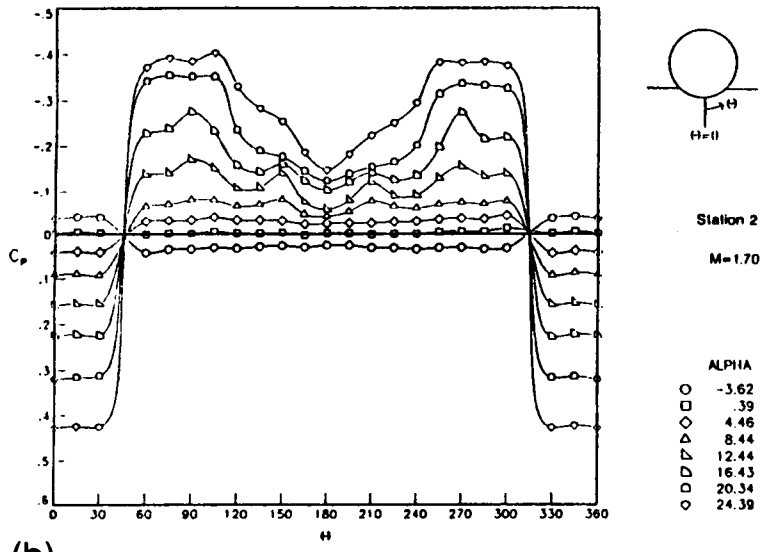

(b)

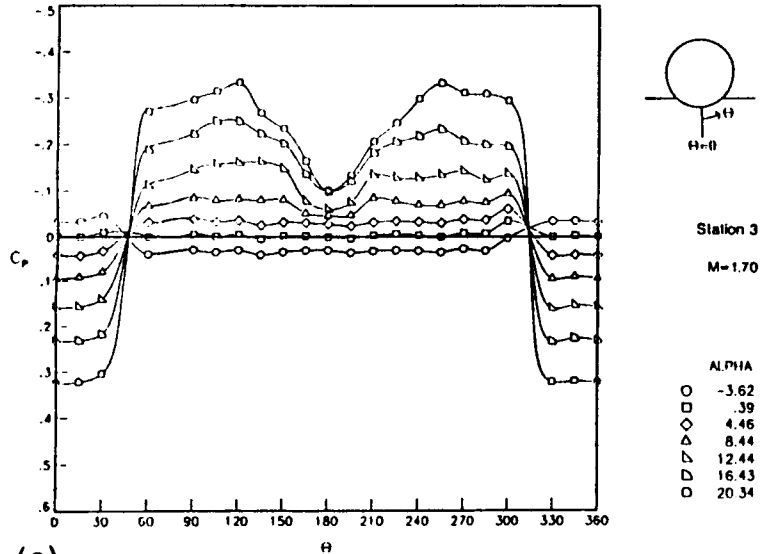

(c)

Figure 23.- Experimental Pressures for Intermediate Low-Wing Configuration

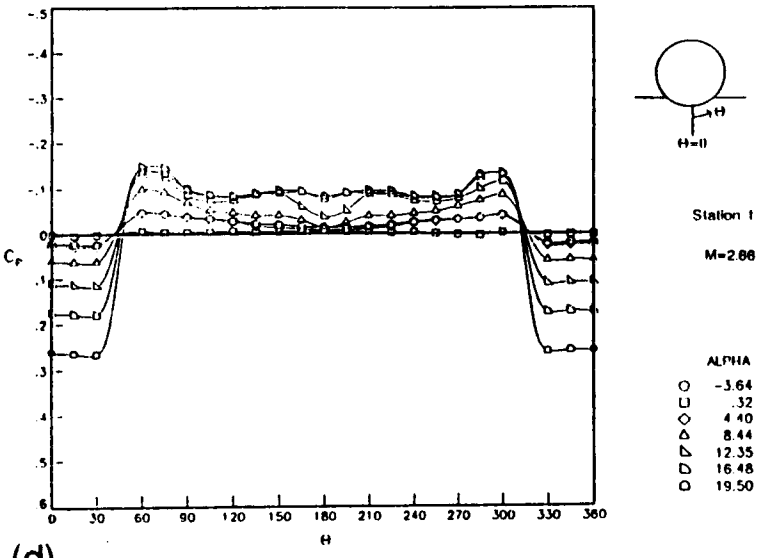

(d)

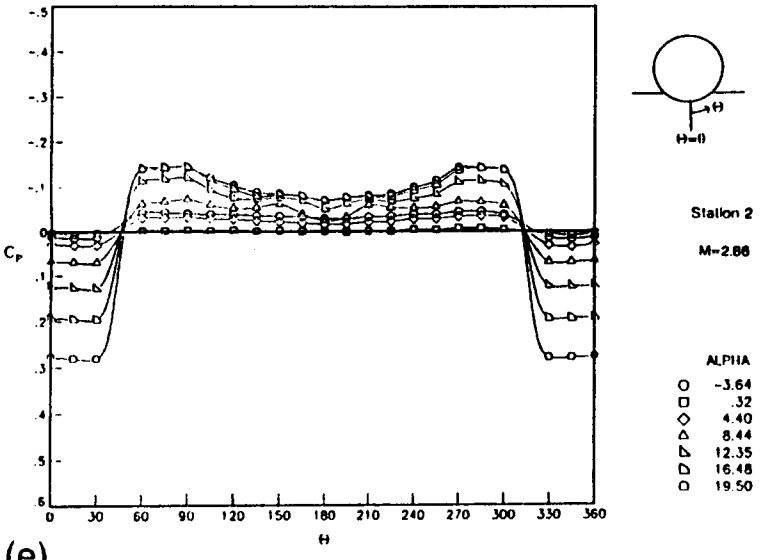

(e)

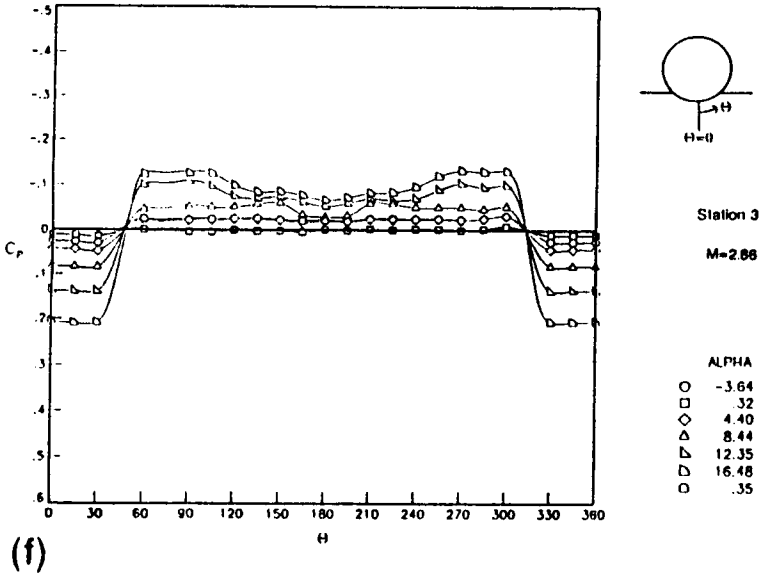

(f)

Figure 23.- Continued

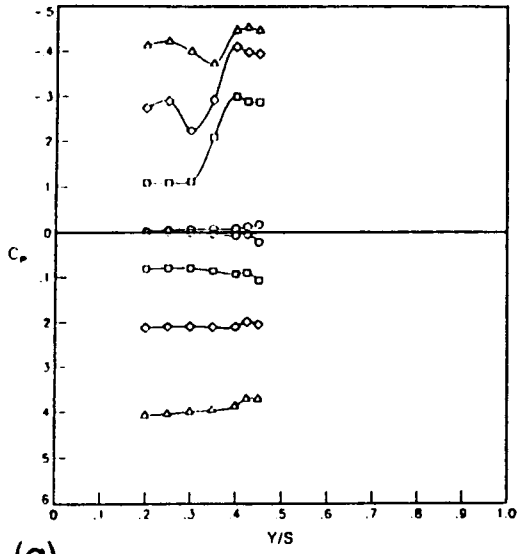

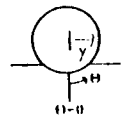

Station 1

M=1.70

ALPHA
○ .39
□ 8.44
◇ 16.43
△ 24.39

(g)

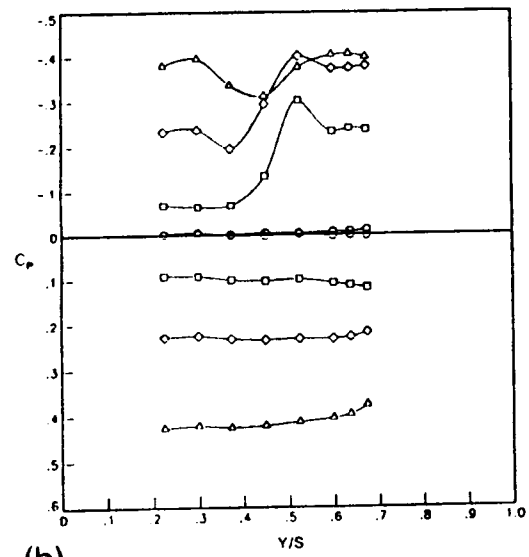

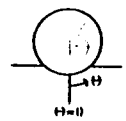

Station 2

M=1.70

ALPHA
○ .39
□ 8.44
◇ 16.43
△ 24.39

(h)

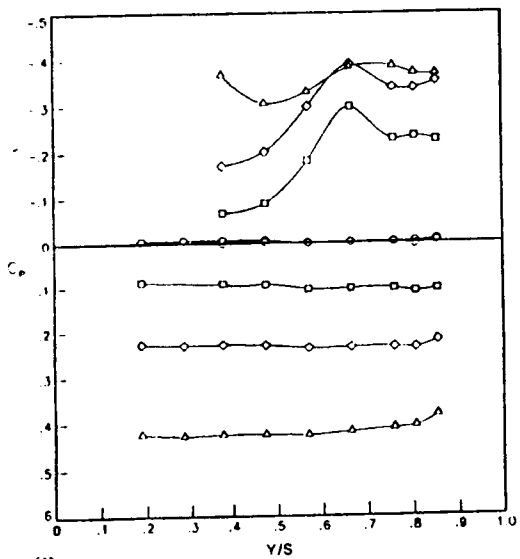

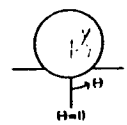

Station 3

M=1.70

ALPHA
○ .39
□ 8.44
◇ 16.43
△ 24.39

(i)

ORIGINAL PAGE IS
OF POOR QUALITY

Figure 23.-Concluded

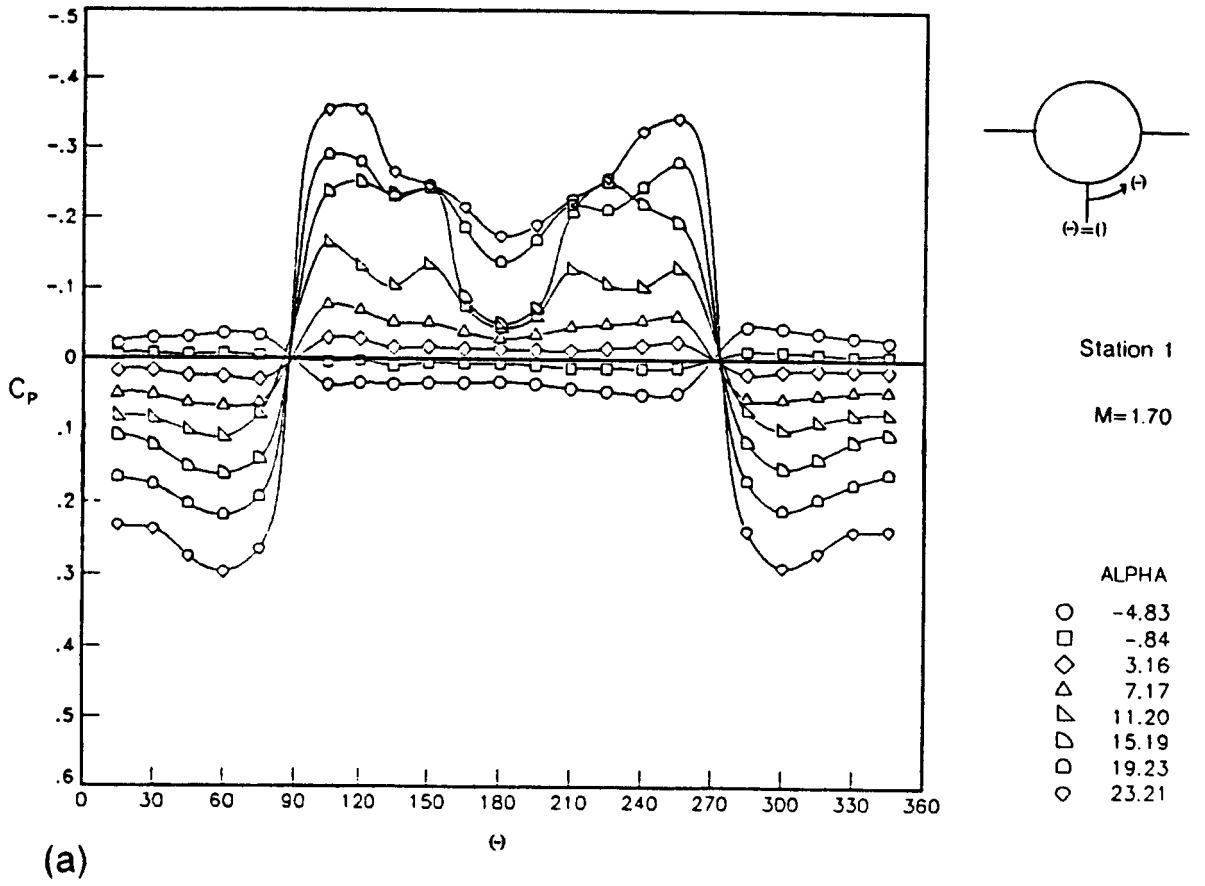

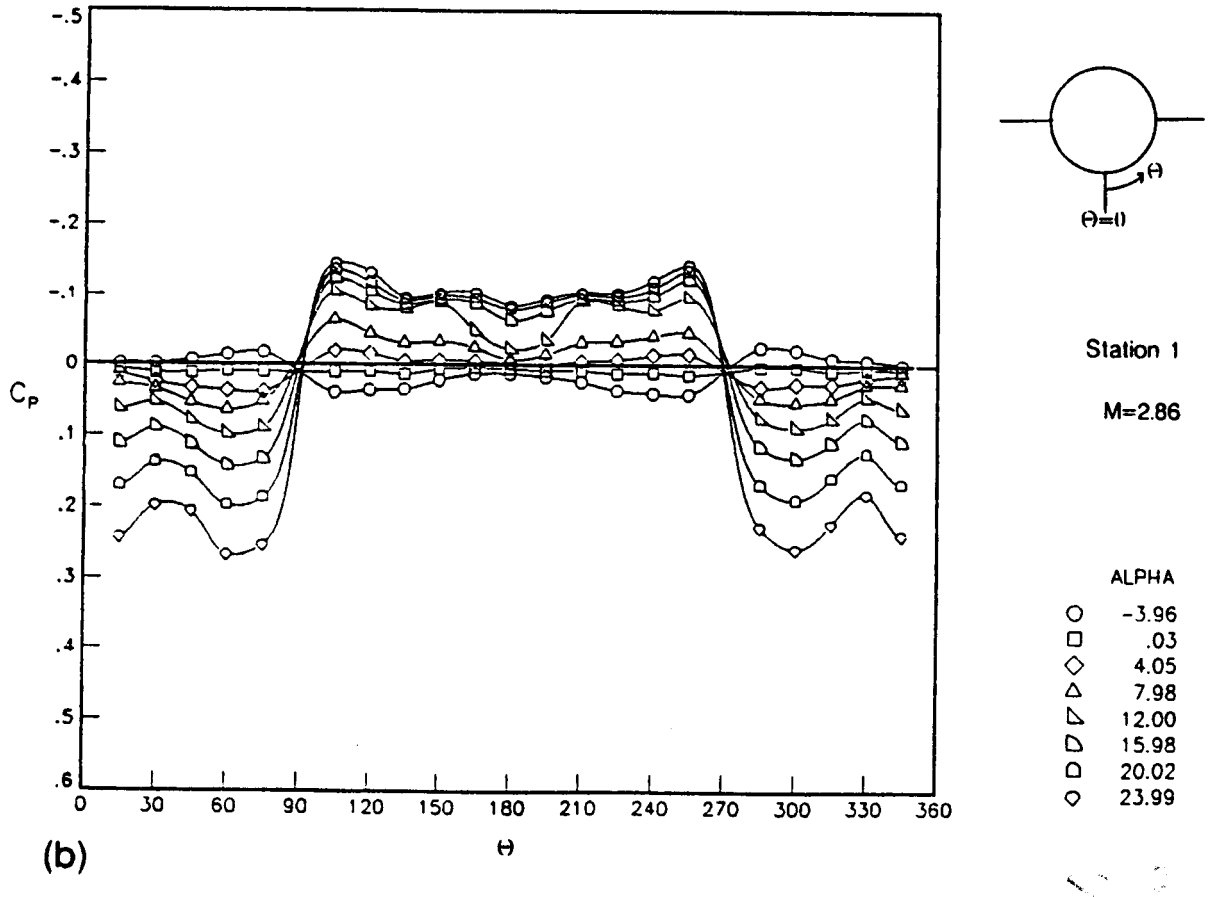

Figure 24.- Experimental Pressures for Mid-Wing Configuration

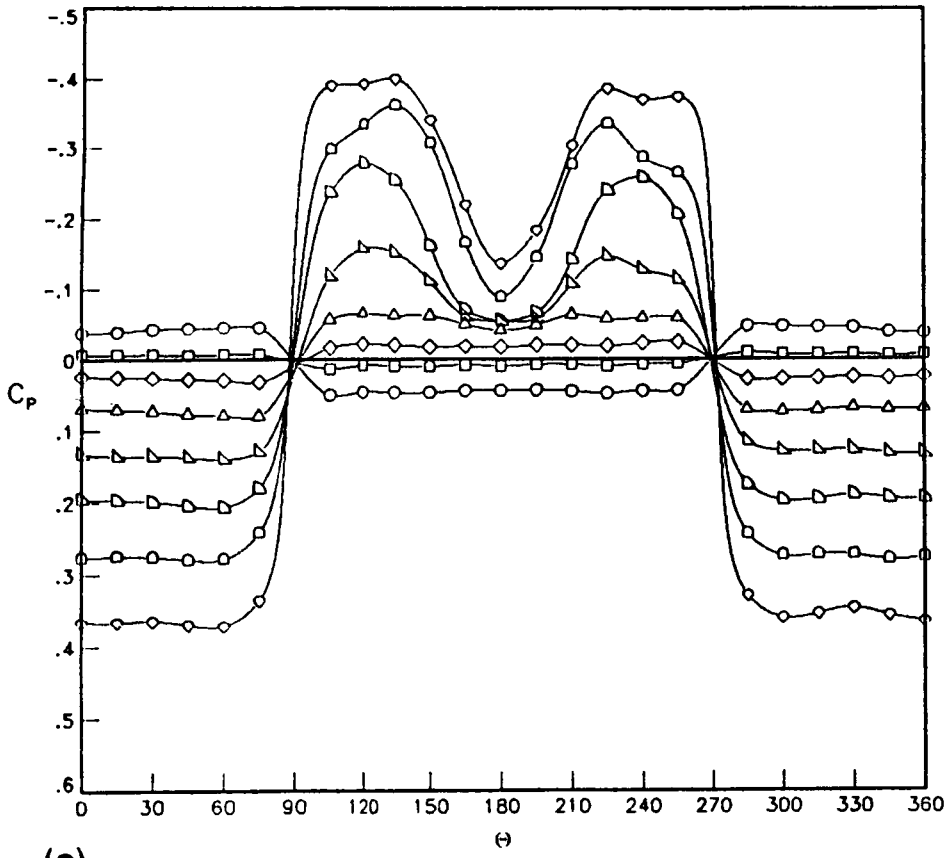

(c)

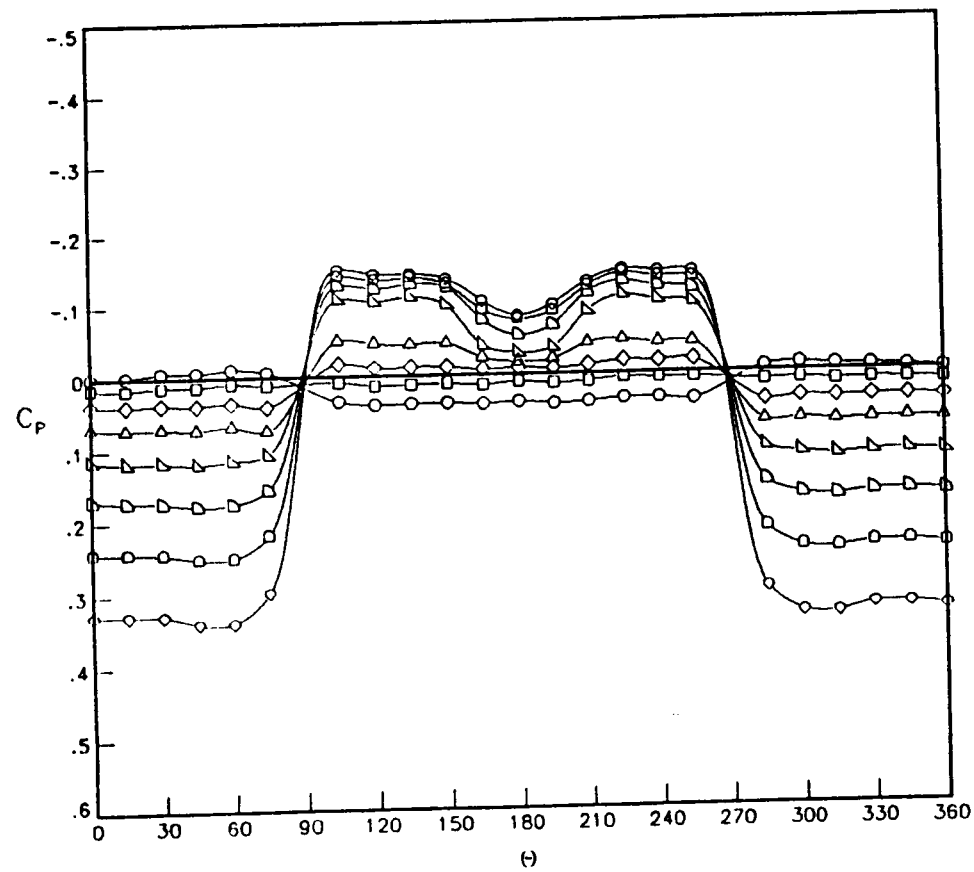

(d)

Figure 24.- Continued

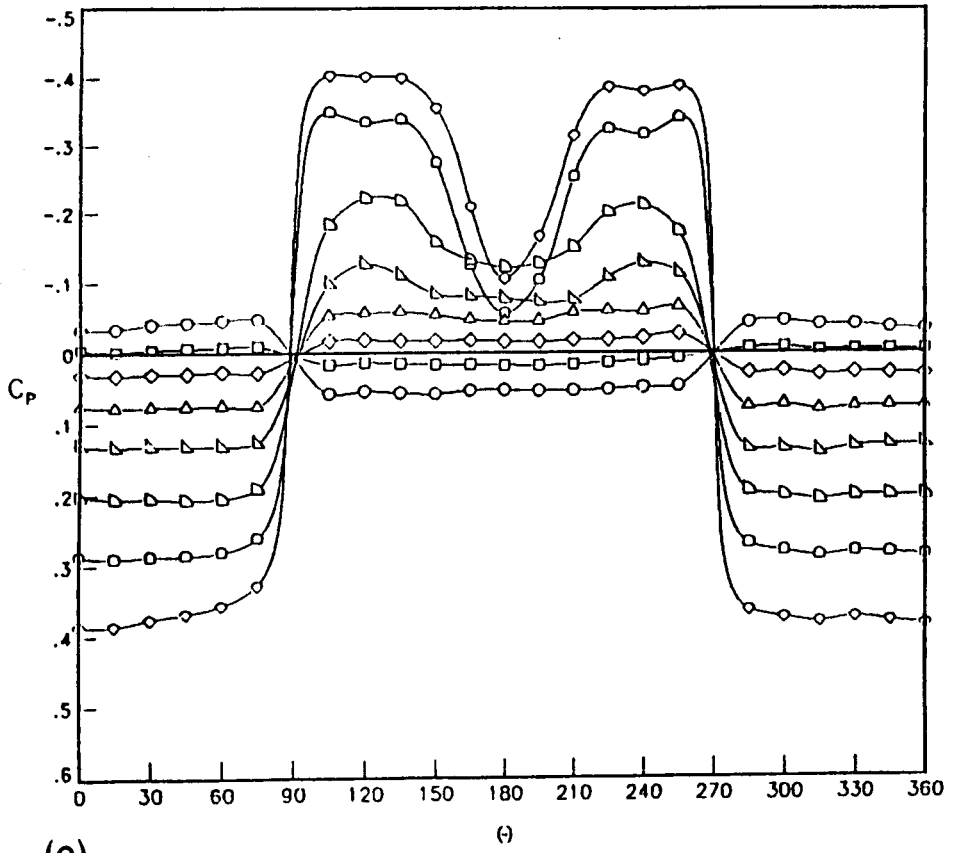

(e)

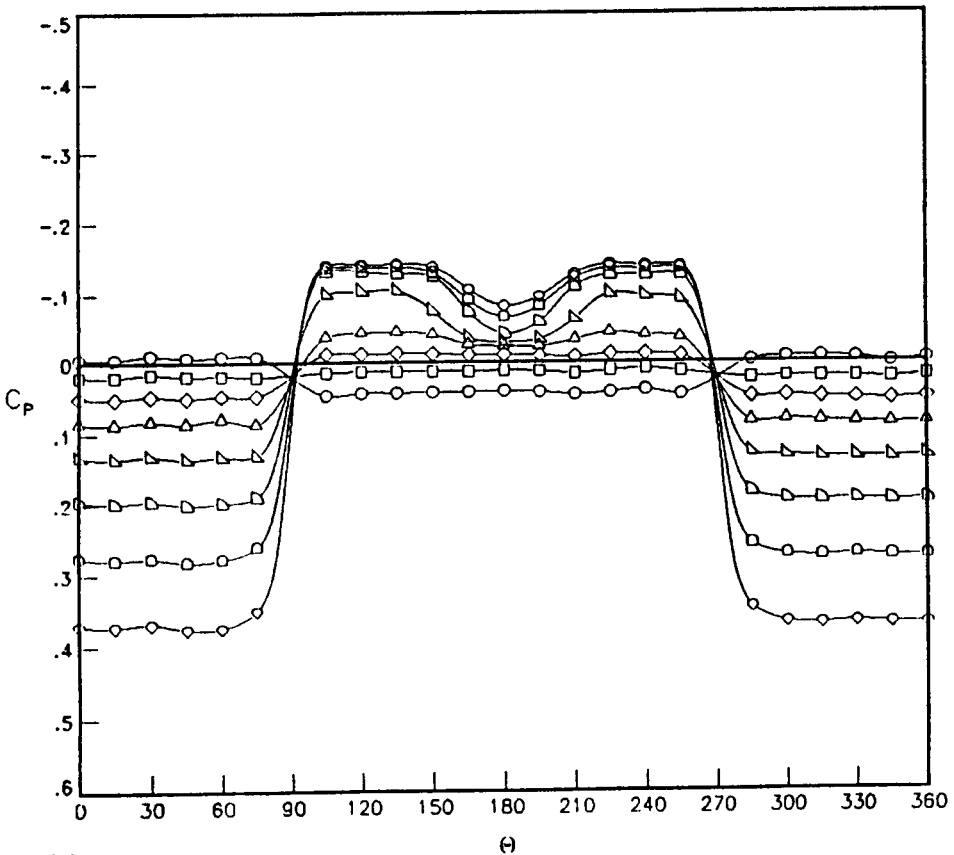

(f)

Figure 24.- Continued

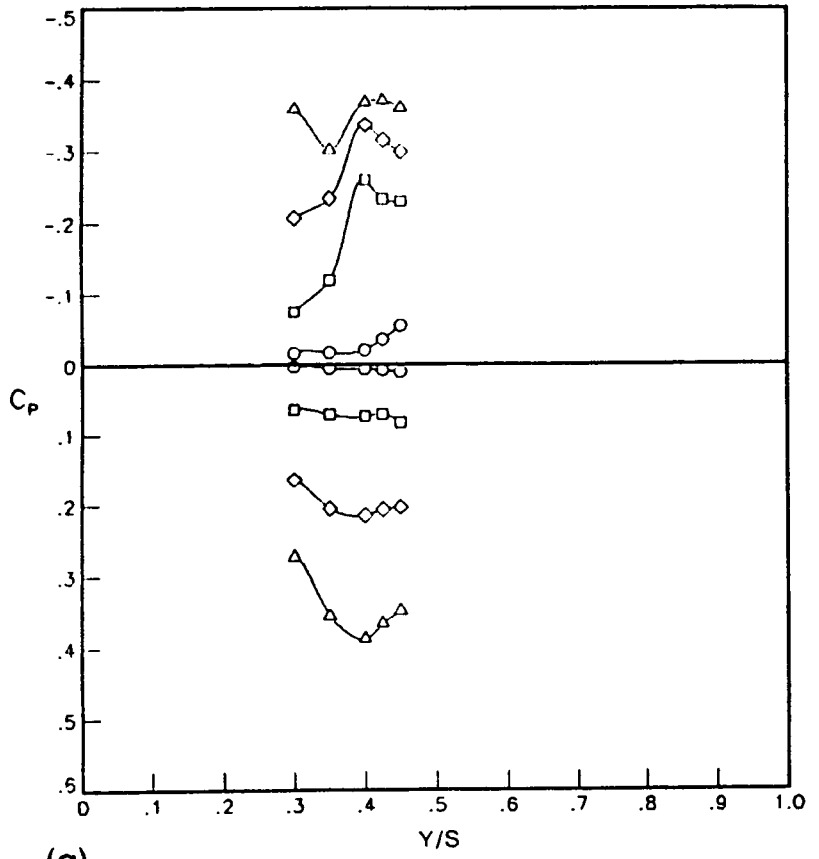

(g)

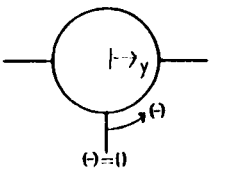

Station 1

M=1.70

ALPHA

○ -.84
□ 7.17
◇ 15.19
△ 23.21

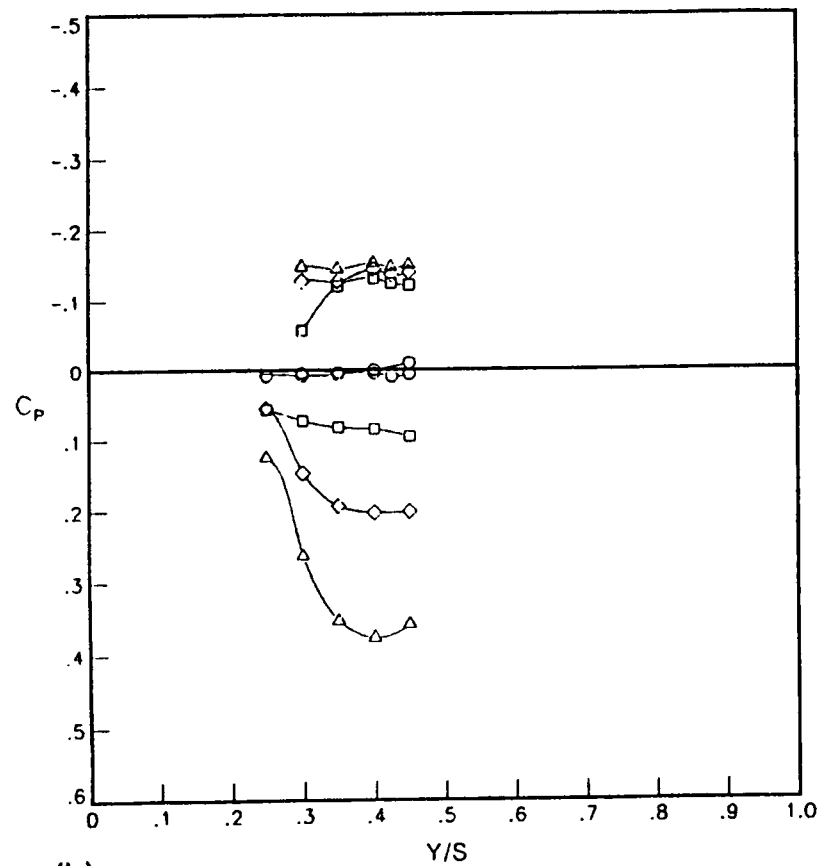

(h)

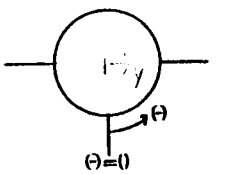

Station 1

M=2.86

ALPHA

○ .03
□ 7.98
◇ 15.98
△ 23.99

Figure 24 .- Continued

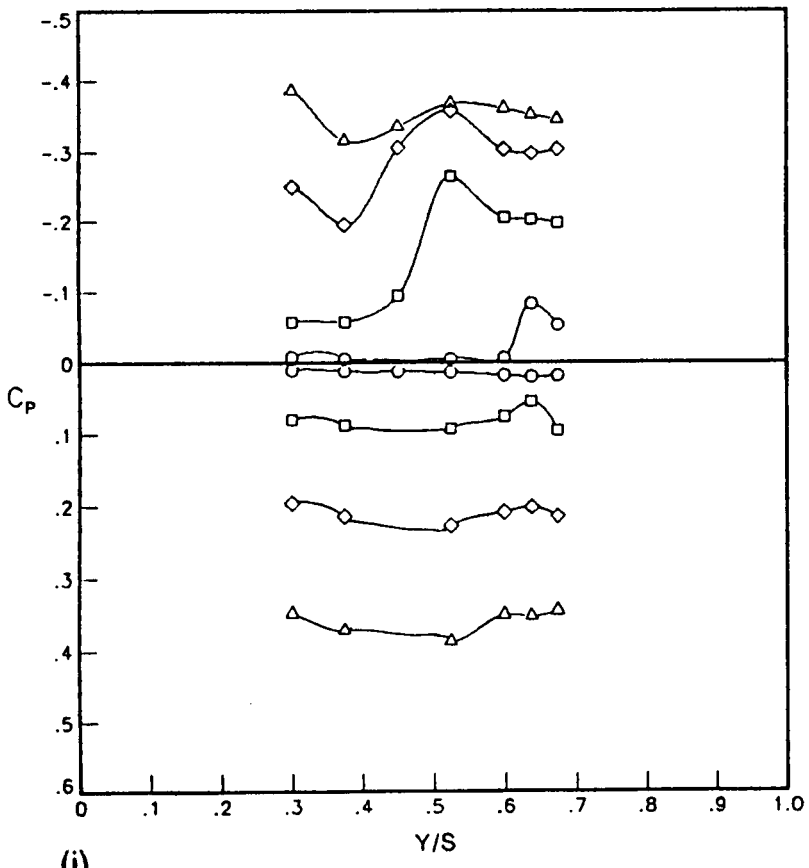

(i)

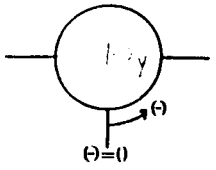

Station 2

M=1.70

ALPHA

○	-.84
□	7.17
◇	15.19
△	23.21

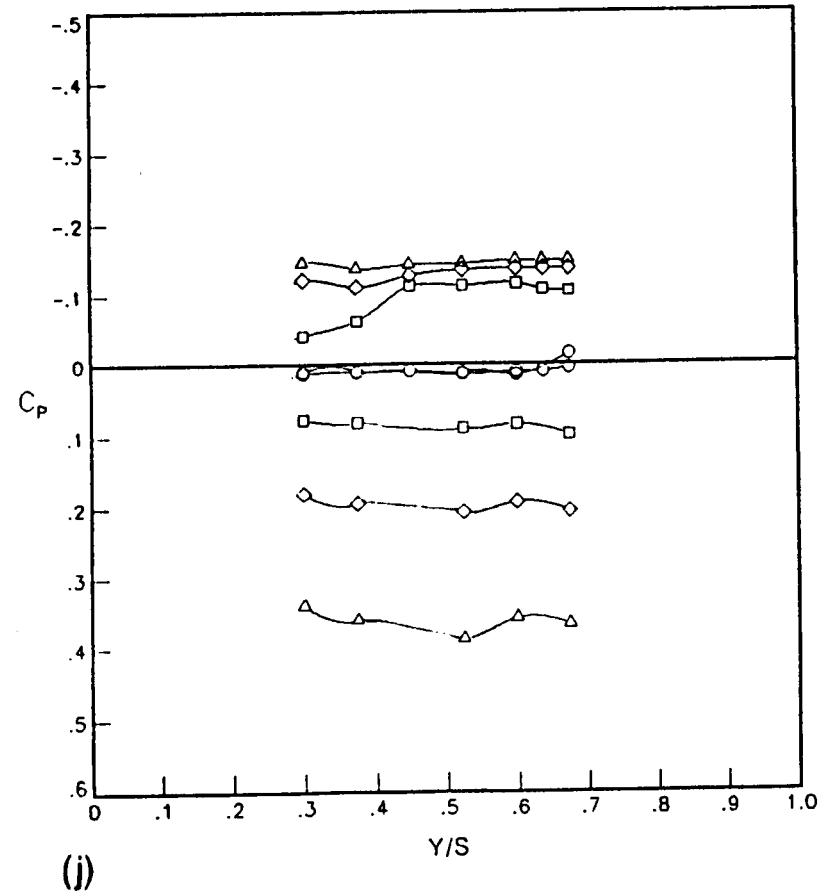

(j)

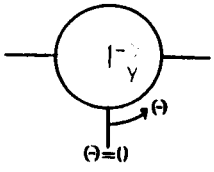

Station 2

M=2.86

ALPHA

○	.03
□	7.98
◇	15.98
△	23.99

Figure24 .- Continued

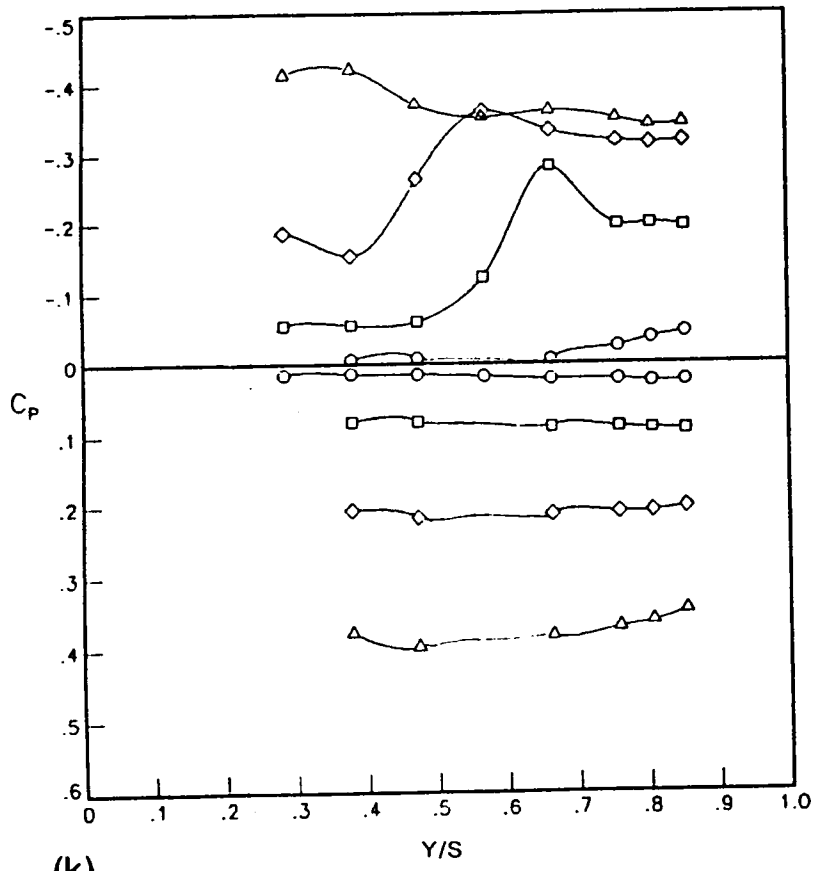

(k)

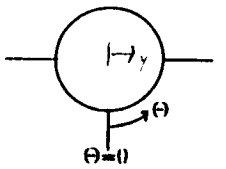

Station 3

M=1.70

ALPHA

○	-.84
□	7.17
◇	15.19
△	23.21

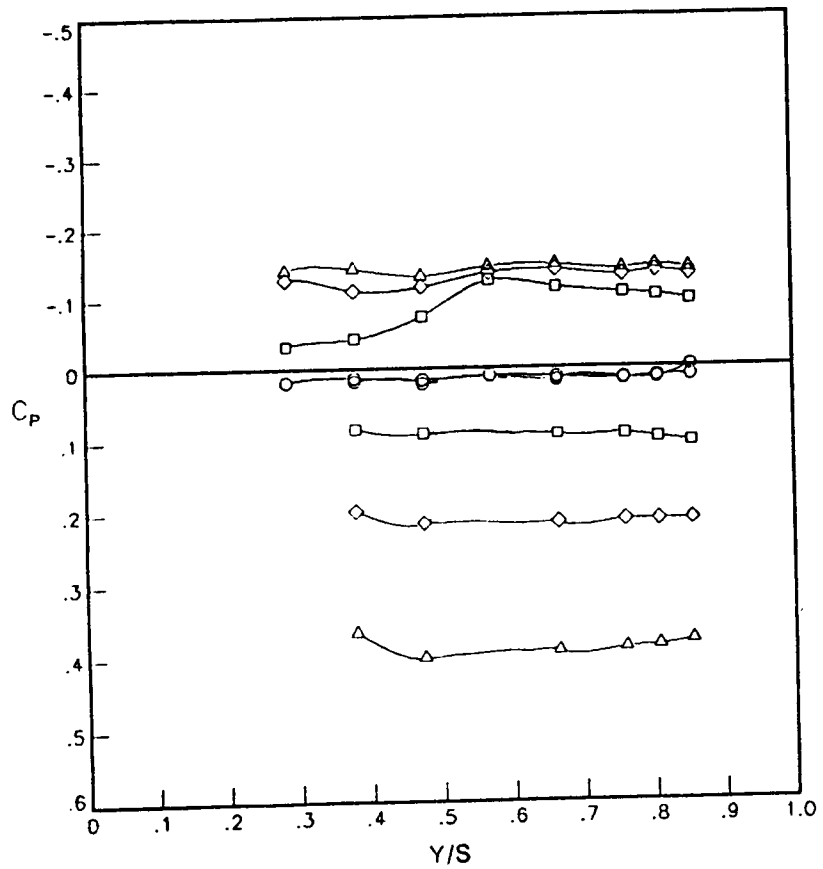

(l)

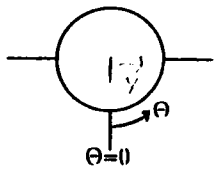

Station 3

M=2.86

ALPHA

○	.03
□	7.98
◇	15.98
△	23.99

Figure 24 .-Concluded

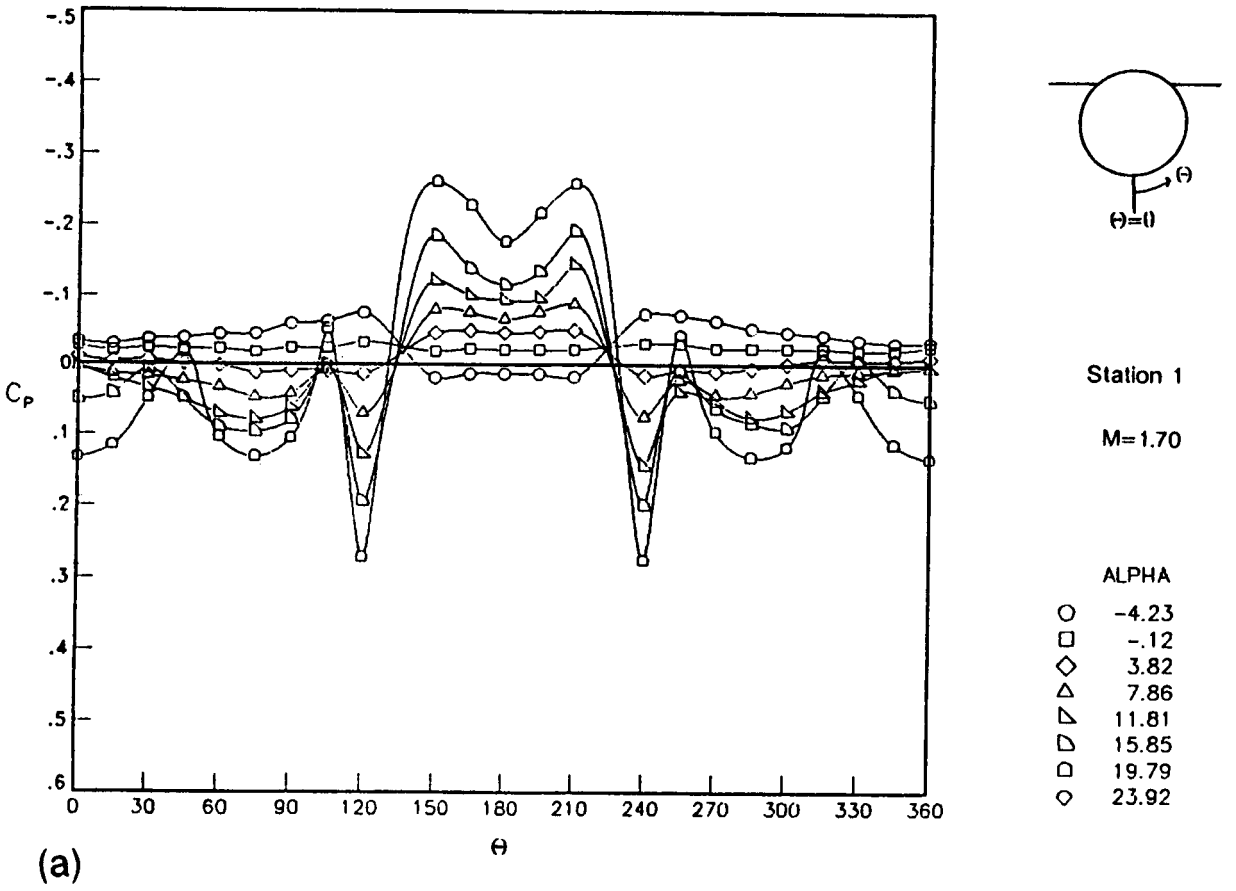

(a)

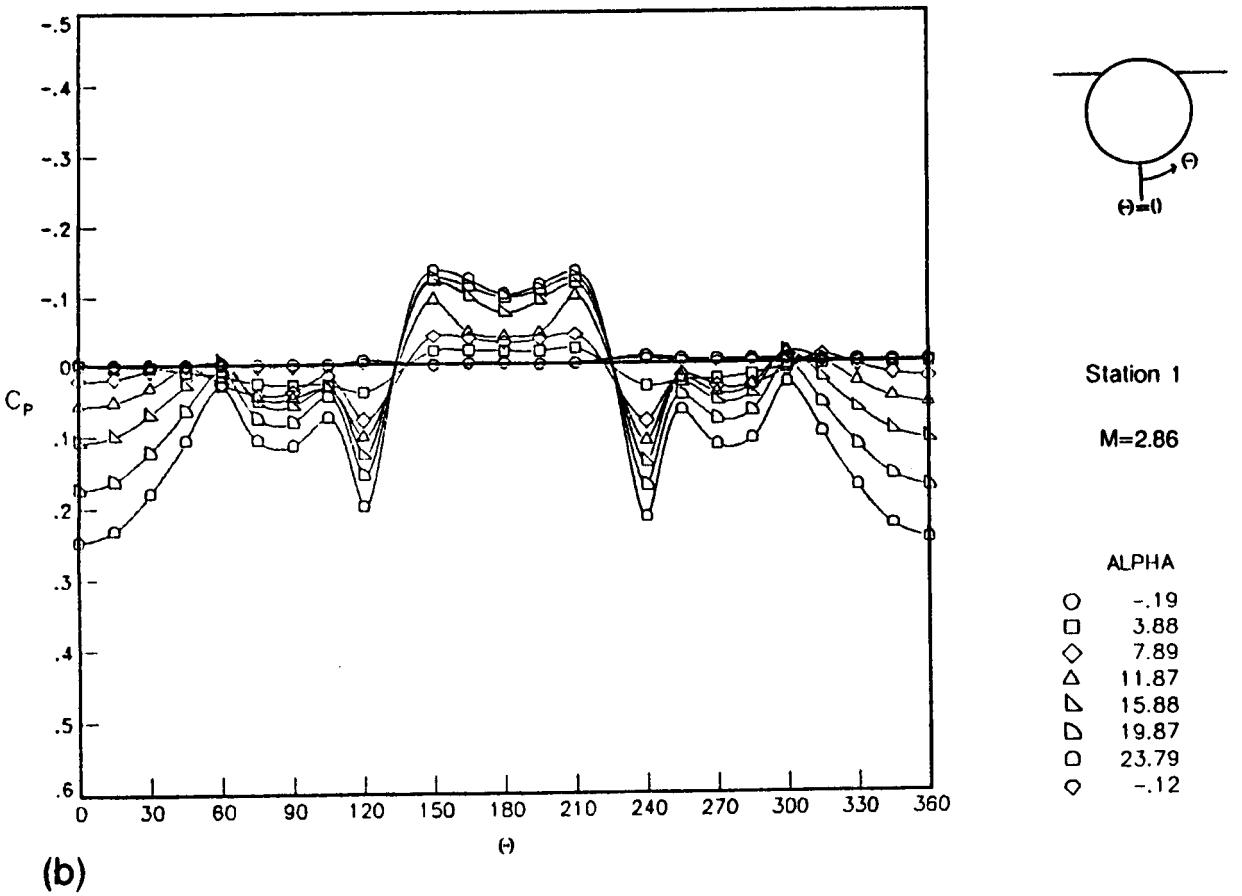

(b)

Figure 25.- Experimental Pressures for Intermediate High-Wing Configuration

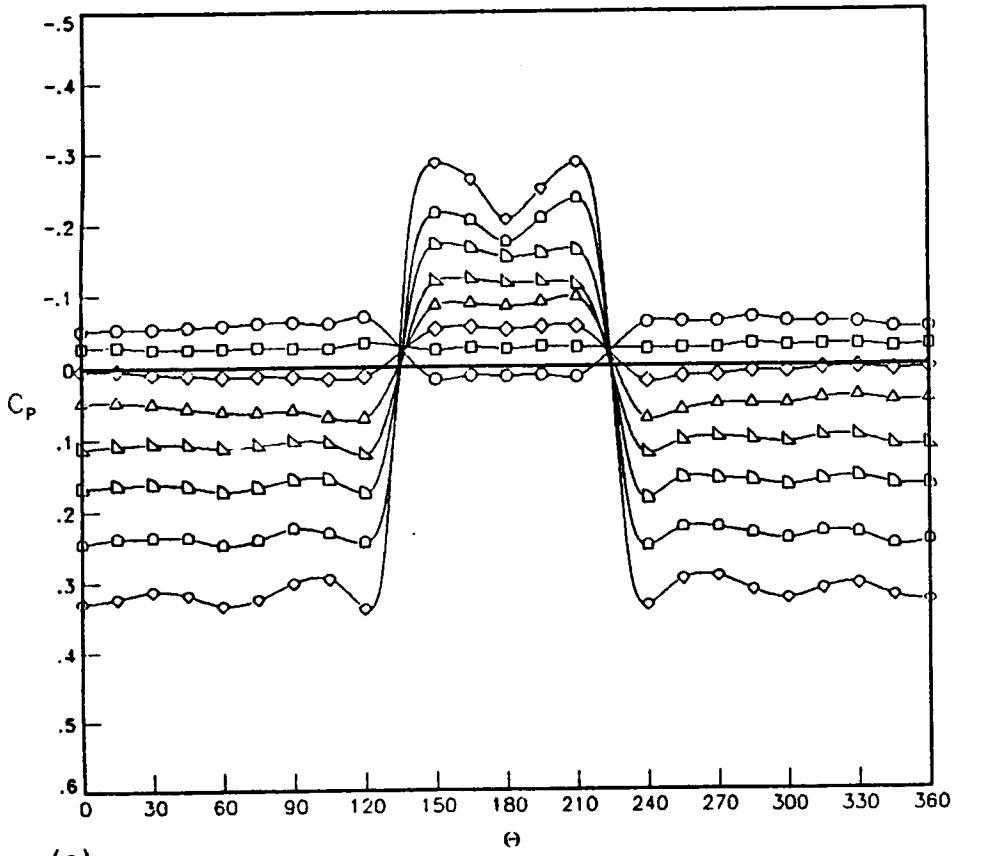

(c)

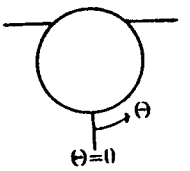

Station 2

M=1.70

ALPHA

○	-4.23
□	-.12
◇	3.82
△	7.86
◺	11.81
◺	15.85
◻	19.79
◇	23.92

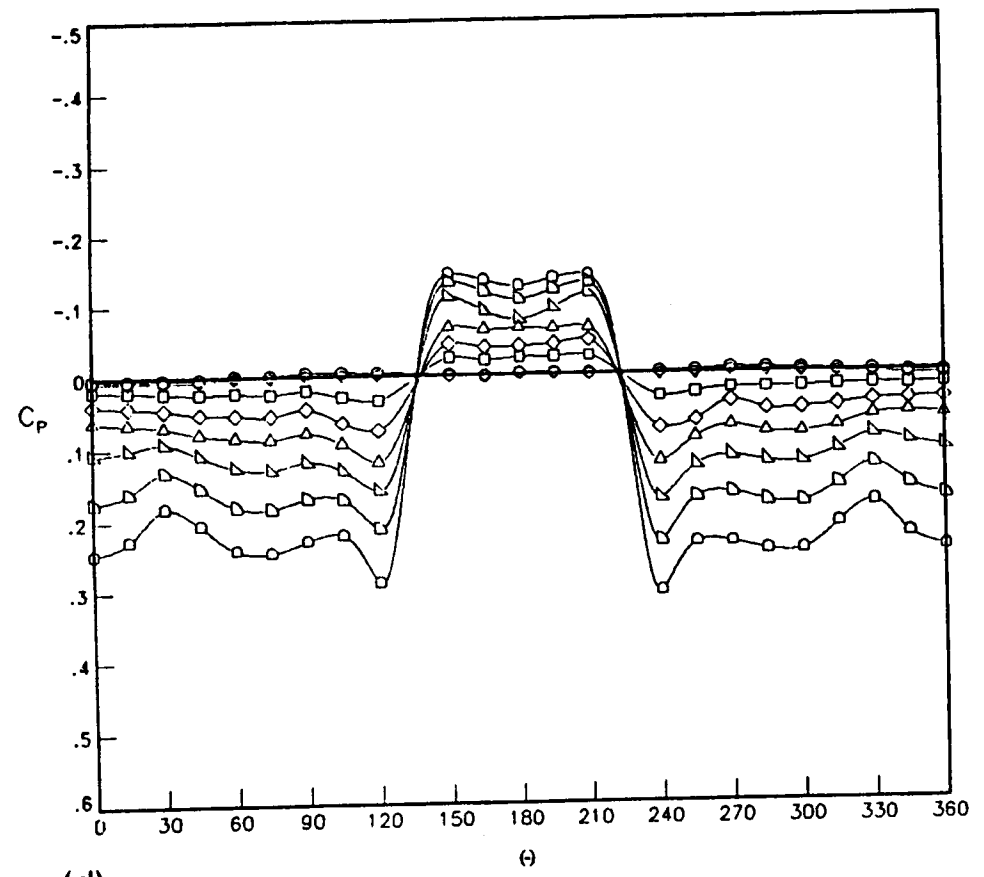

(d)

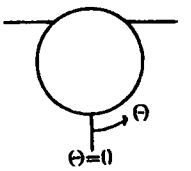

Station 2

M=2.86

ALPHA

○	-.19
□	3.88
◇	7.89
△	11.87
◺	15.88
◺	19.87
◻	23.79
◇	-.12

Figure 25.- Continued

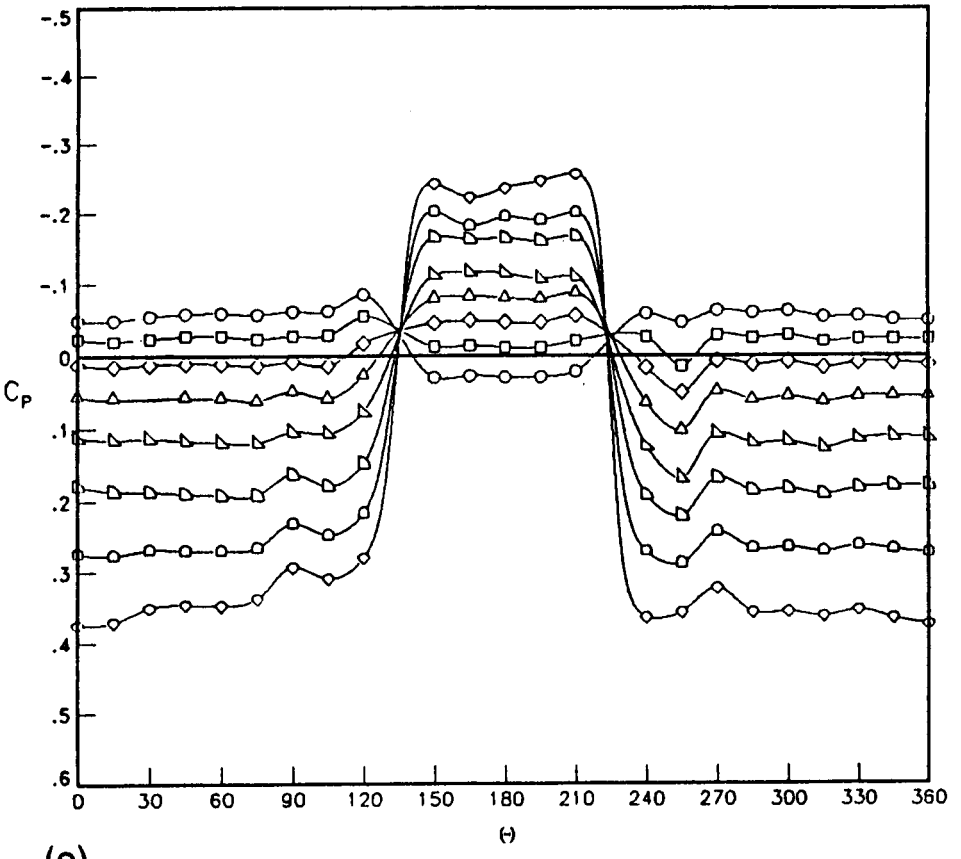

(e)

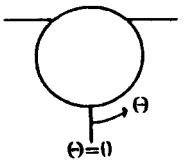

Station 3

M=1.70

ALPHA

○	-4.23
□	-.12
◇	3.82
△	7.86
◺	11.81
◺	15.85
◺	19.79
◇	23.92

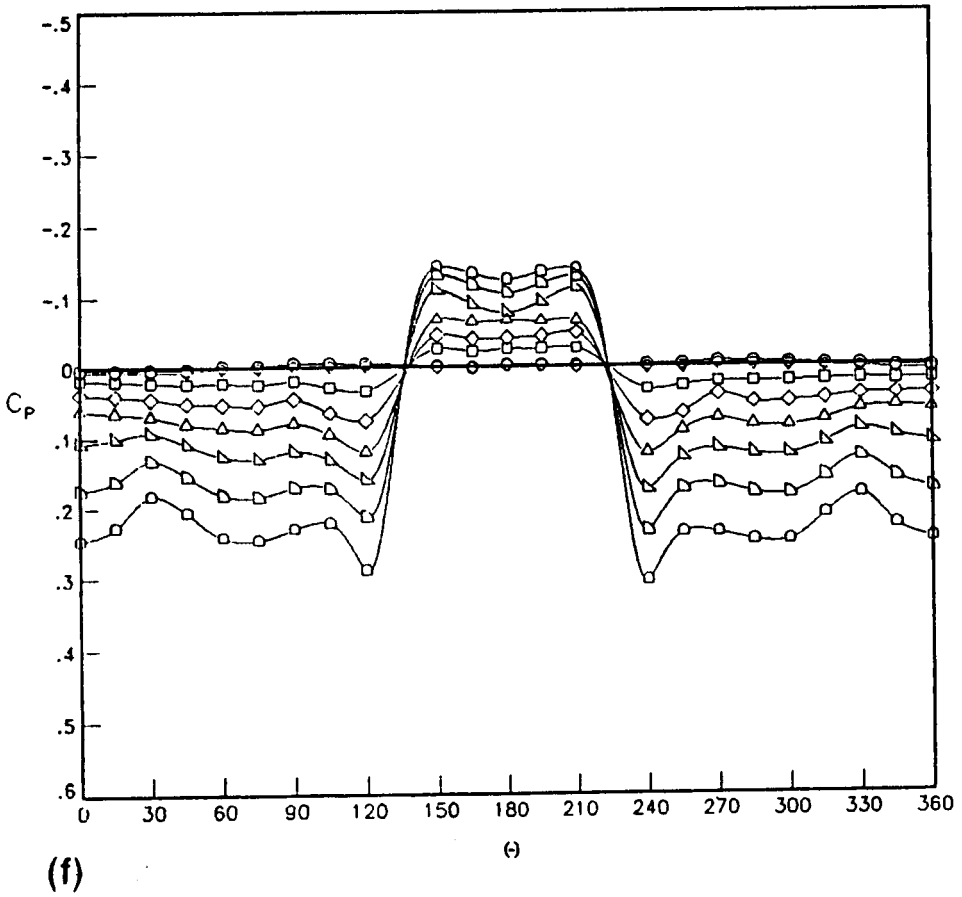

(f)

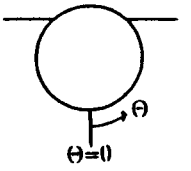

Station 3

M=2.86

ALPHA

○	-.19
□	3.88
◇	7.89
△	11.87
◺	15.88
◺	19.87
◺	23.79
◇	-.12

Figure 25.- Continued

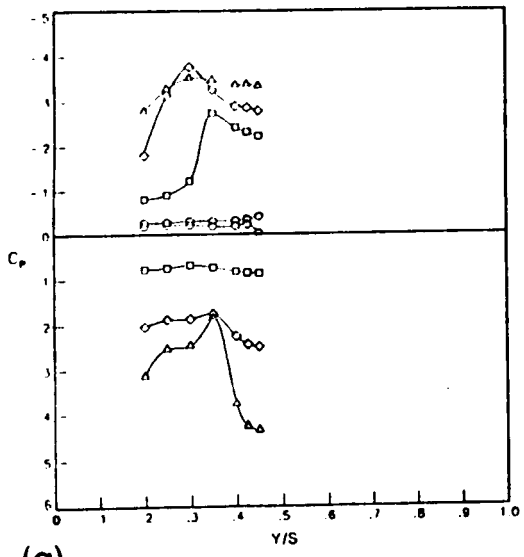

(g)

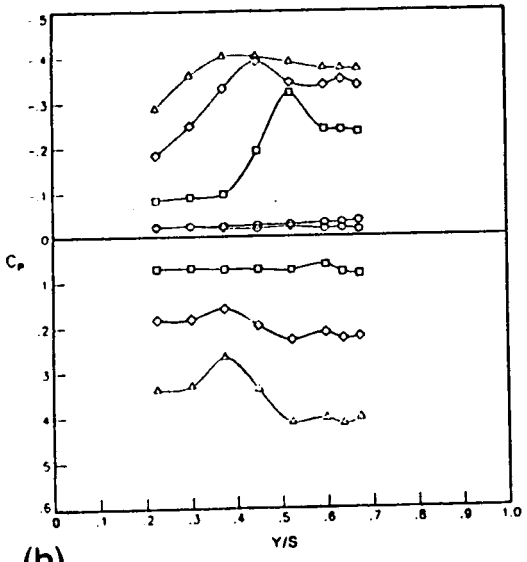

(h)

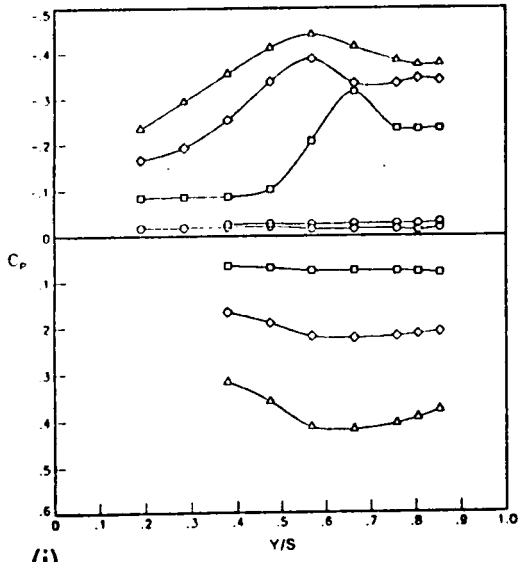

(i)

Figure 25.-Concluded

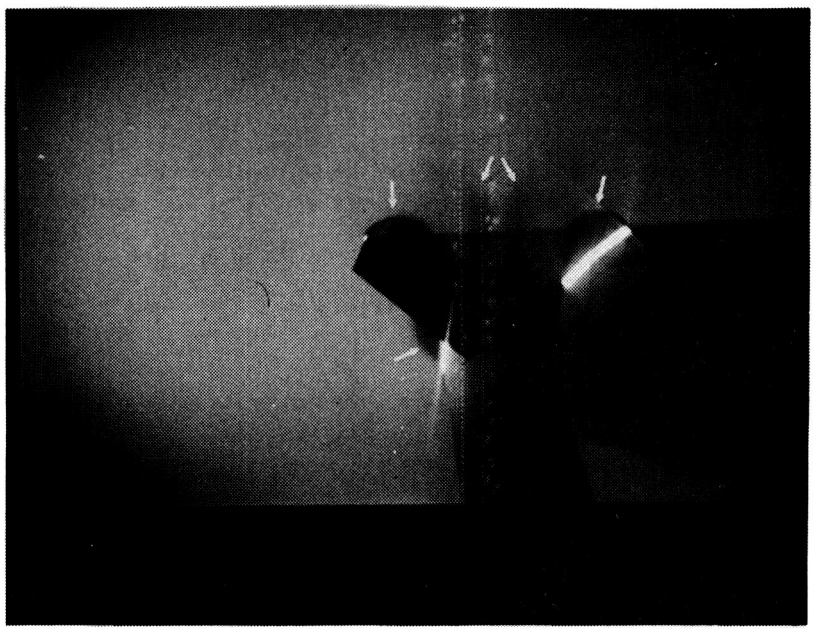

(a)

M=1.70
α=12°
Station 3

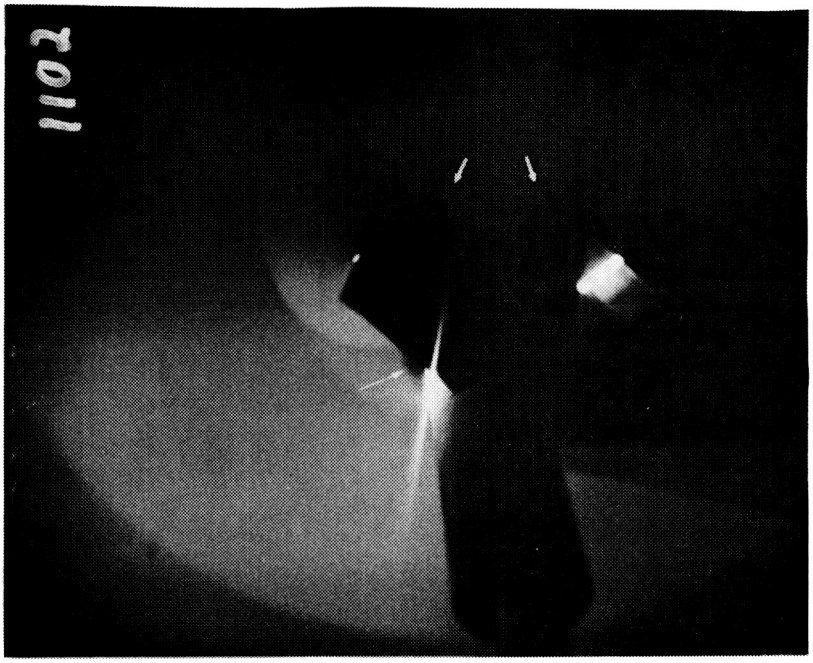

(b)

M=2.86
α=20°
Station 2

Figure 26.- Vapor Screens for Bent-Wing Configuration

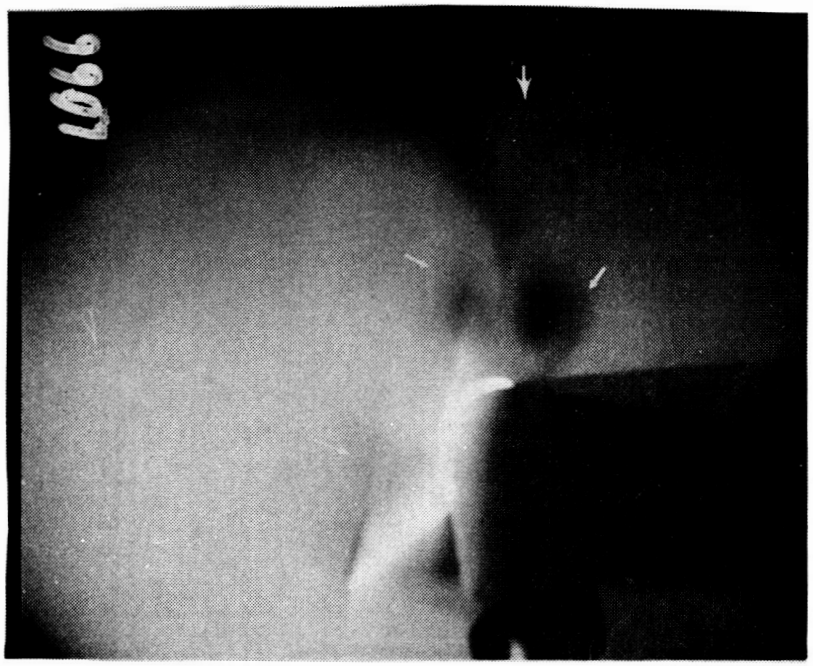

(a)

M=1.70
α=20°
Station 3

(b)

M=2.86
α=12°
Station 3

Figure 27.- Vapor Screens for Inverted Bent-Wing Configuration

(a)

M=1.70
α=12°
Station 1

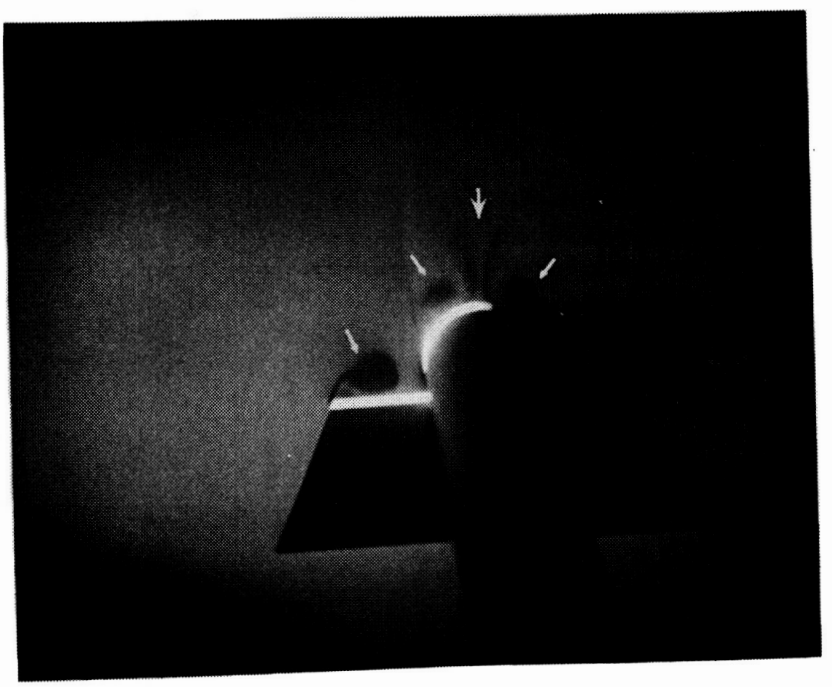

(b)

M=1.70
α=12°
Station 2

Figure 28.- Vapor Screens for Intermediate Low-Wing Configuration

(c)

M=1.70
α=12°
Station 3

(d)

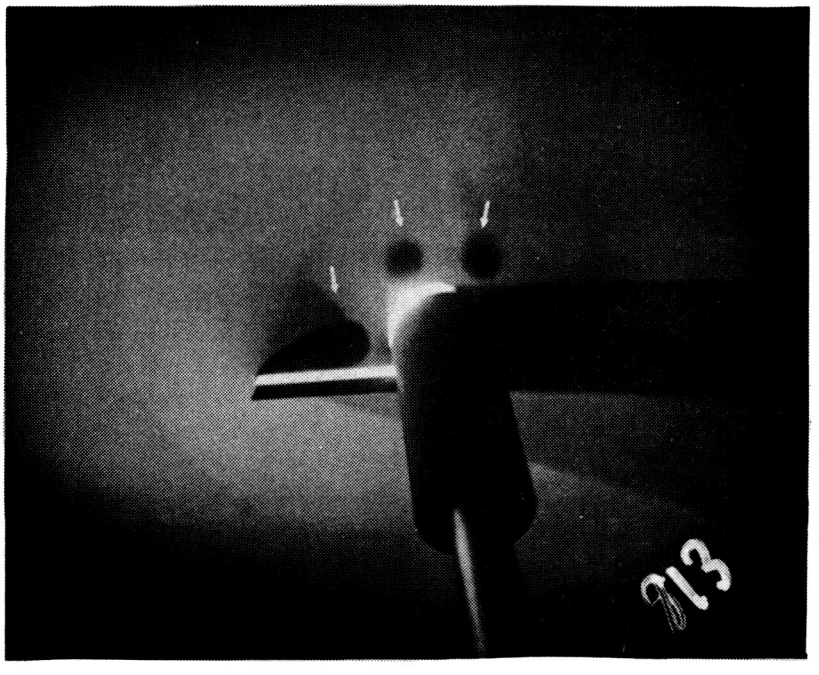

M=2.86
α=12°
Station 3

Figure 28.- Concluded

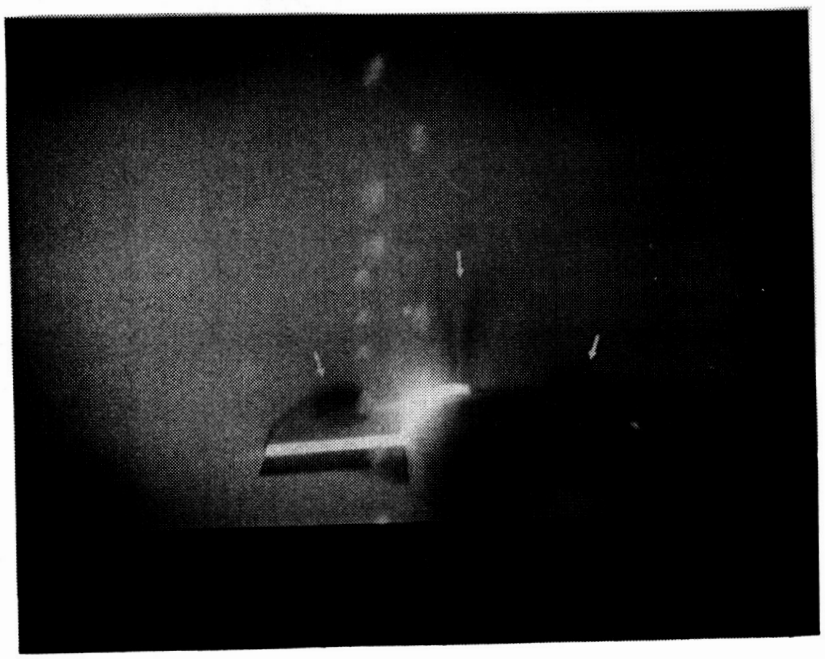

(a)

M=1.70
α=12°
Station 3

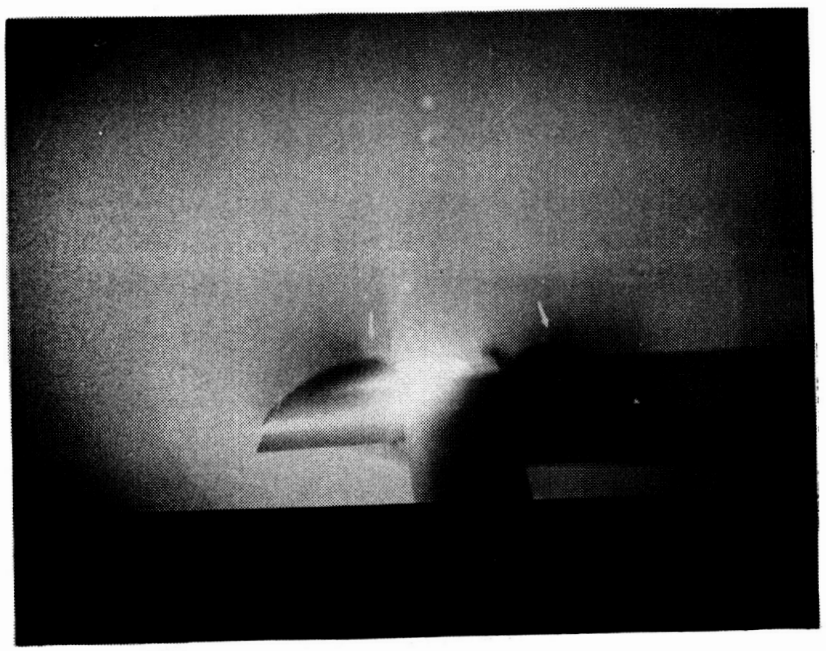

(b)

M=2.86
α=12°
Station 3

Figure 29.- Vapor Screens for Mid-Wing Configuration

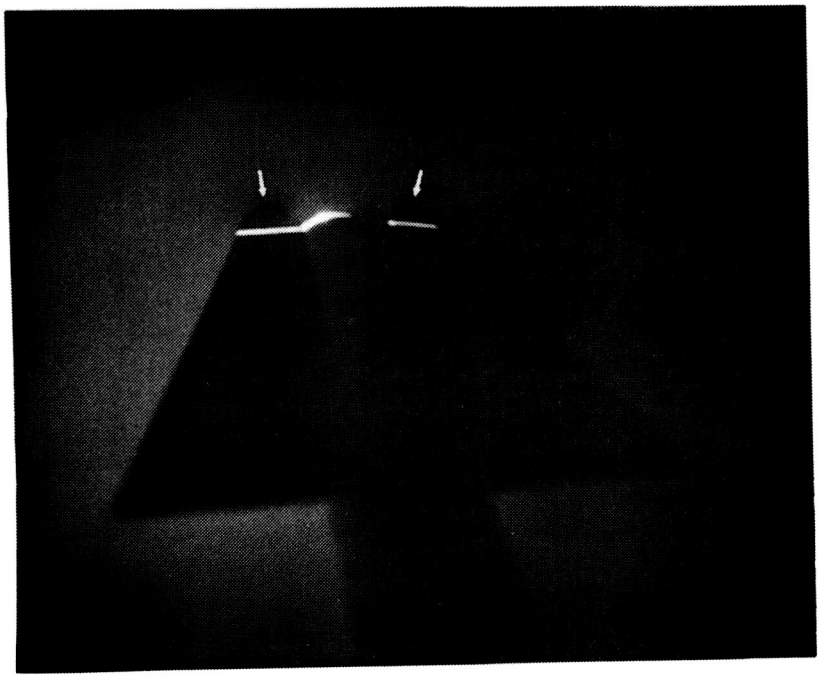

(a)

M=1.70
α=12°
Station 1

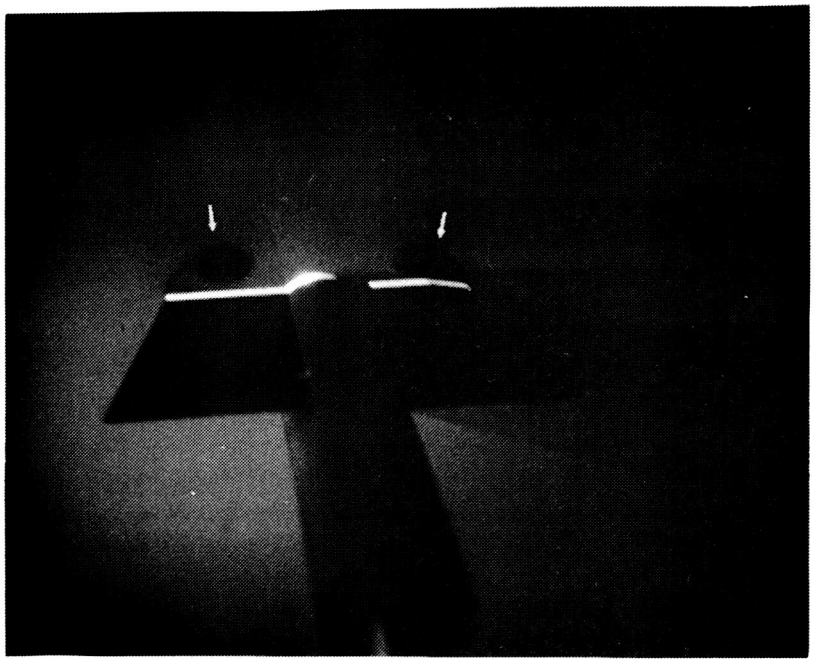

(b)

M=1.70
α=12°
Station 2

Figure 30.- Vapor Screens for Intermediate High-Wing Configuration

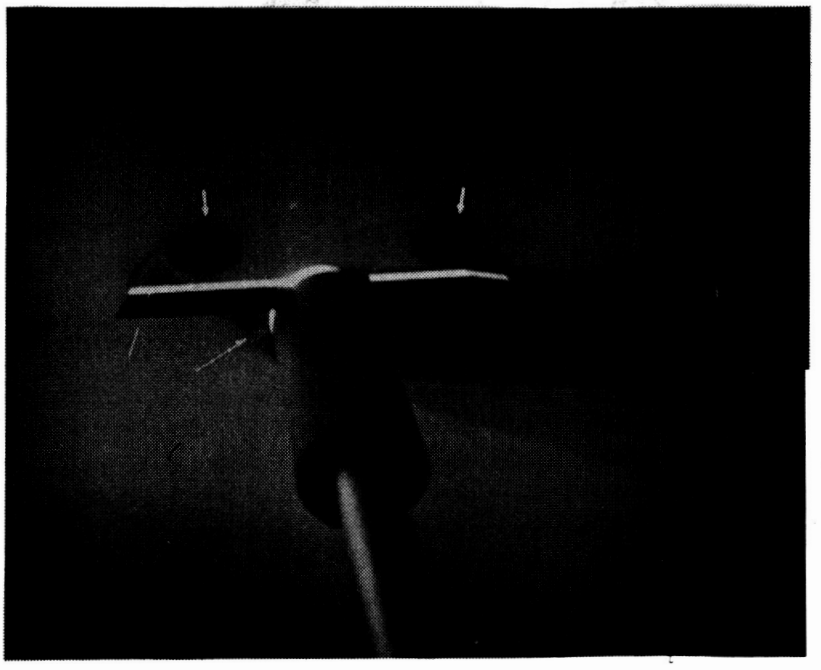

(c)

M=1.70
α=12°
Station 3

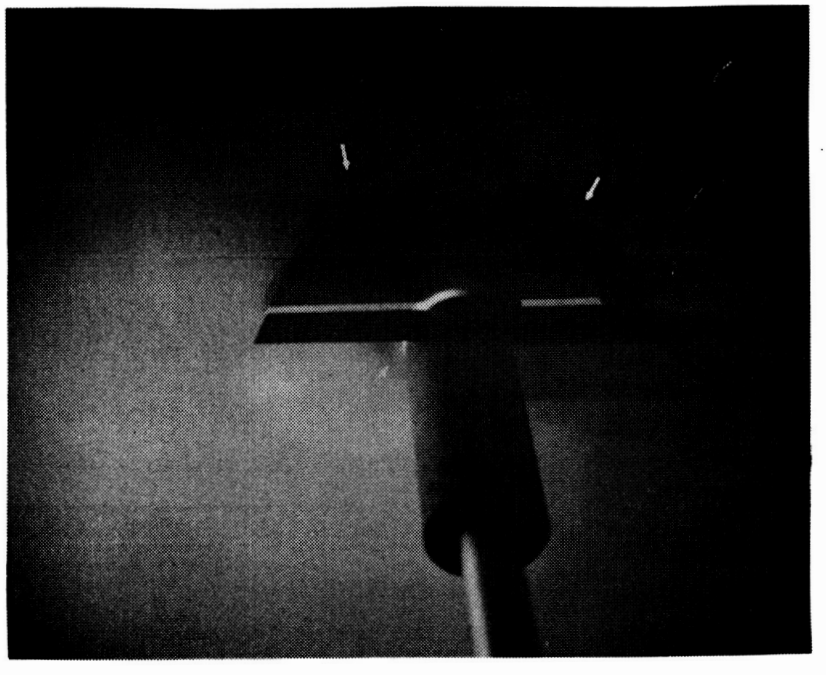

(d)

M=2.86
α=20°
Station 3

Figure 30.- Concluded

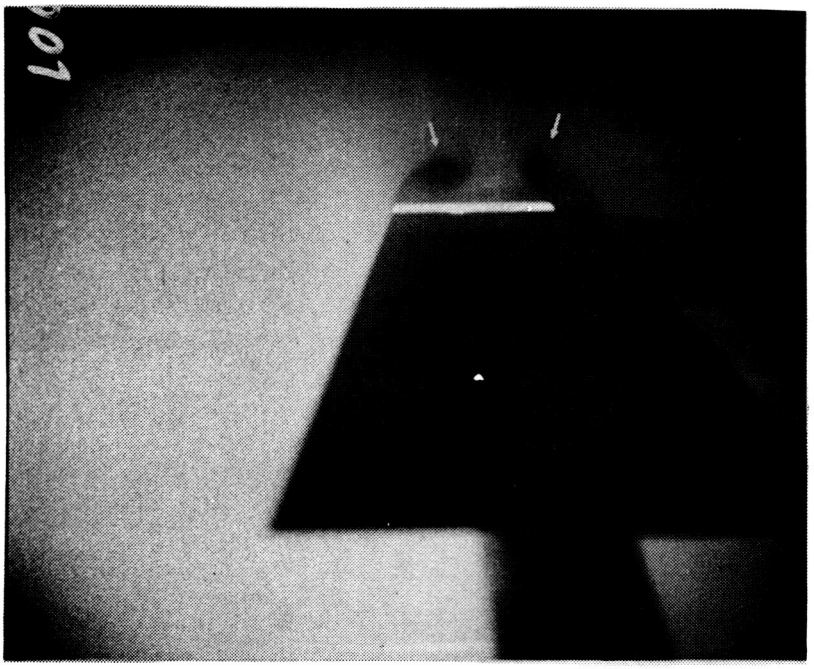

(a)

M=1.70
α=20°
Station 1

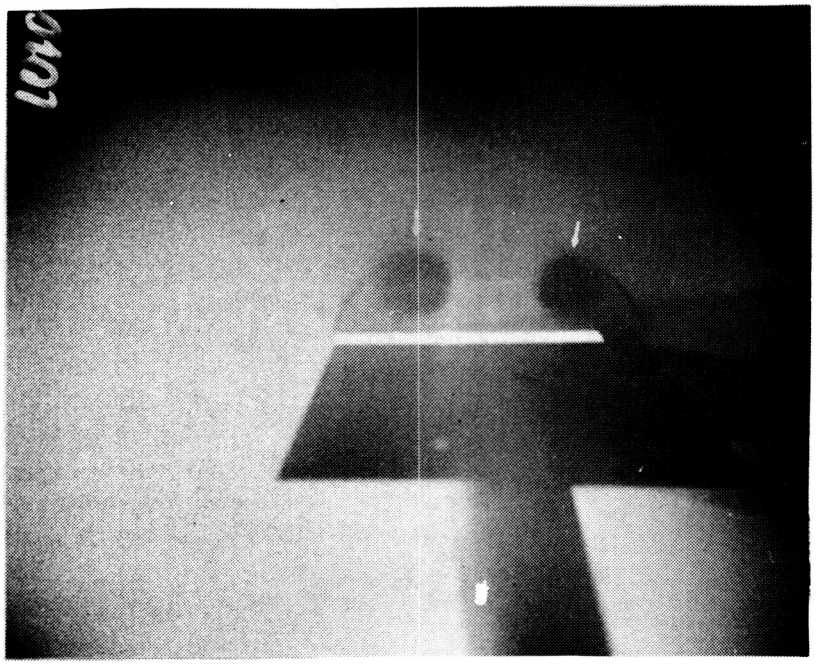

(b)

M=1.70
α=20°
Station 2

Figure 31.- Vapor Screens for High-Wing Configuration

(c)

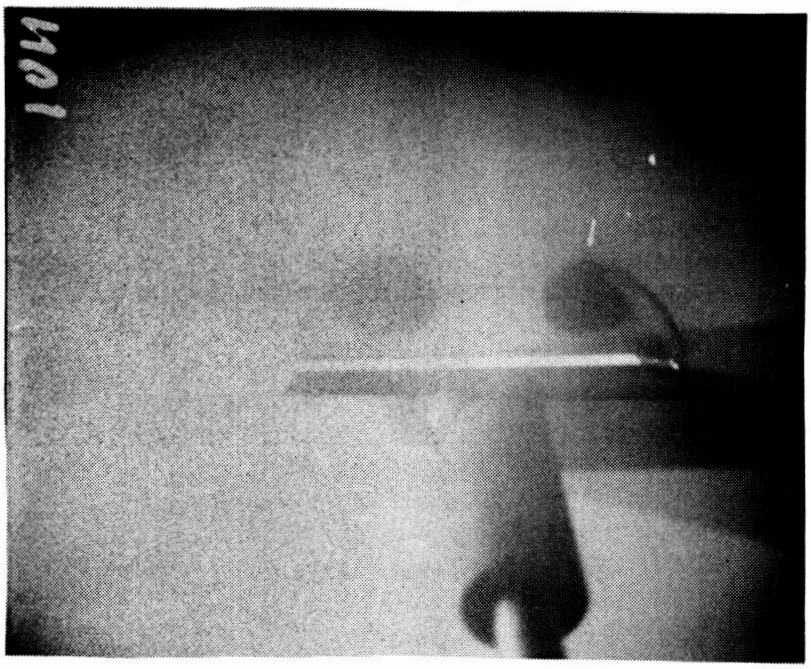

M=1.70
$\alpha=20^{\circ}$
Station 3

(d)

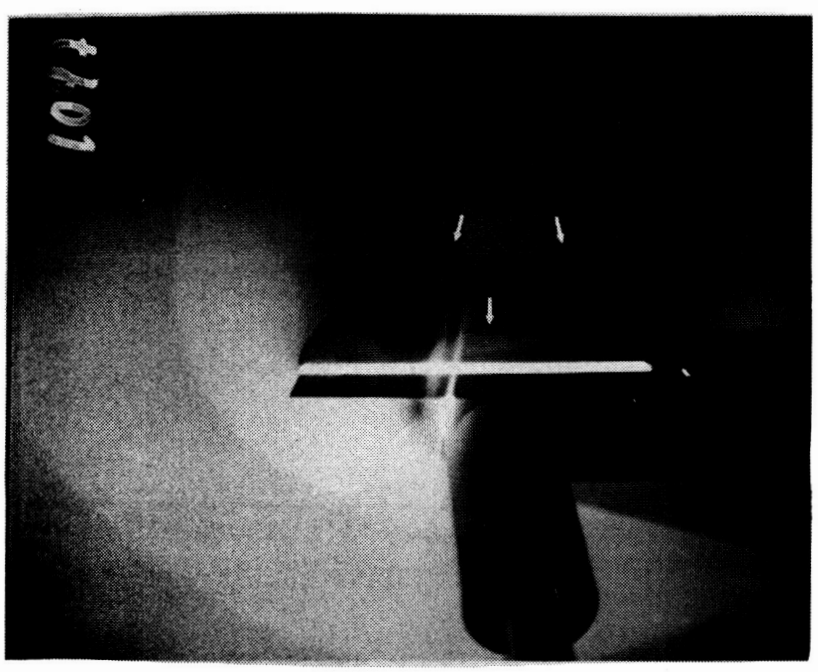

M=2.86
$\alpha=20^{\circ}$
Station 3

Figure 31.- Concluded

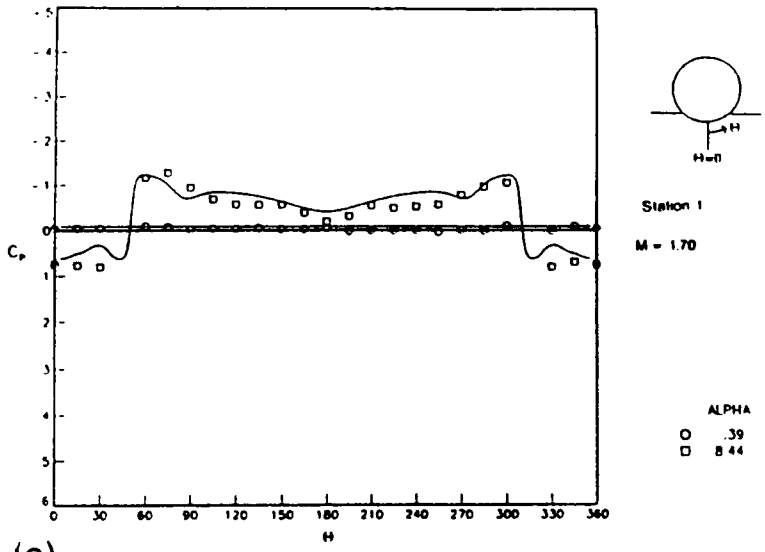

(a)

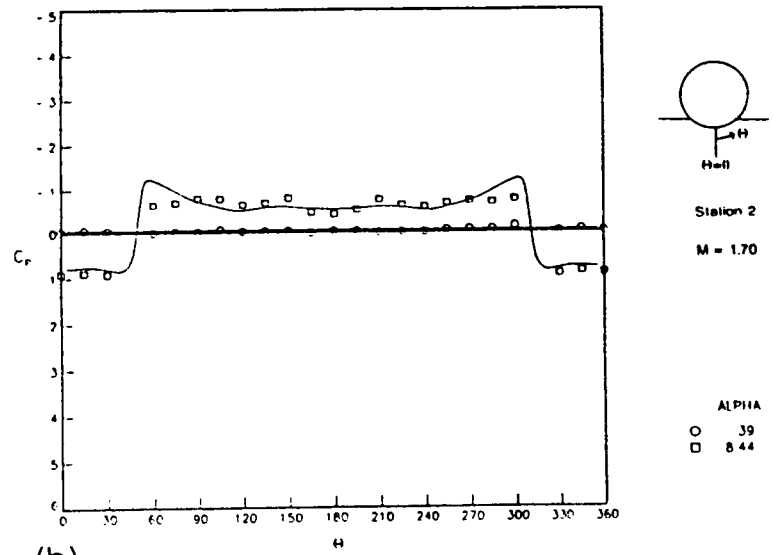

(b)

— theory

o data

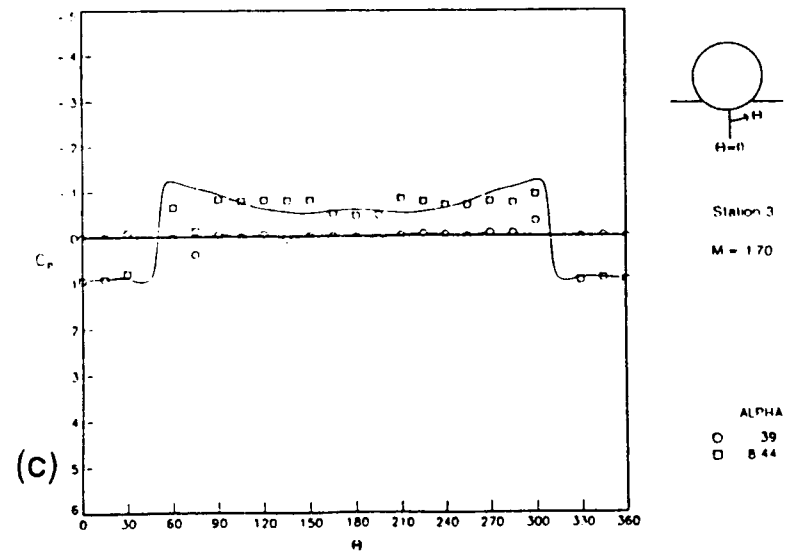

(c)

Figure 32.- Experimental/Theoretical Comparisons for Intermediate Low-Wing Configuration

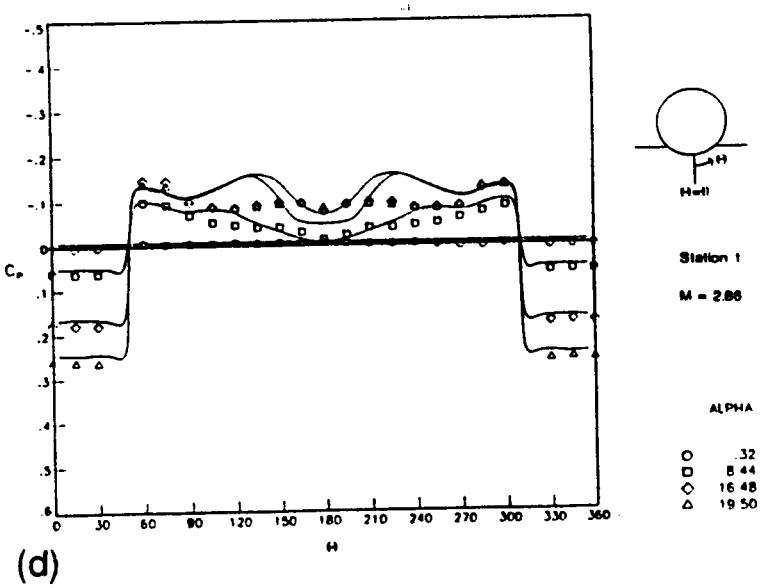

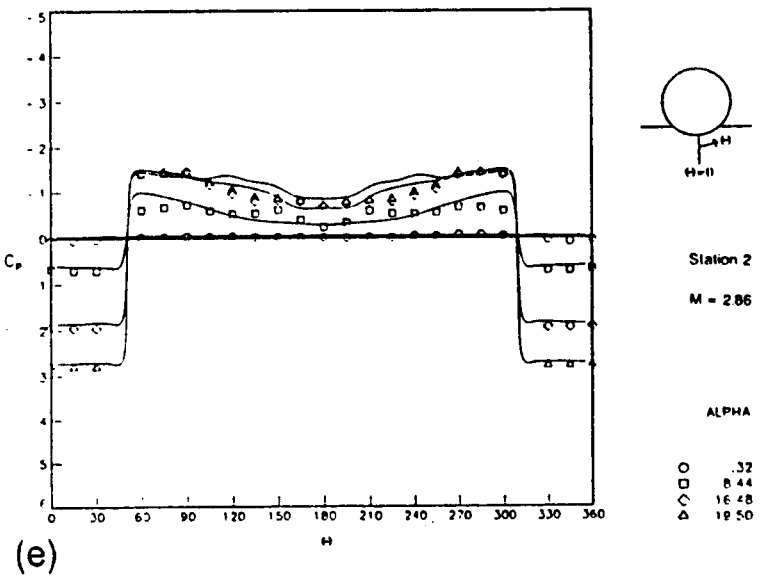

— theory
o data

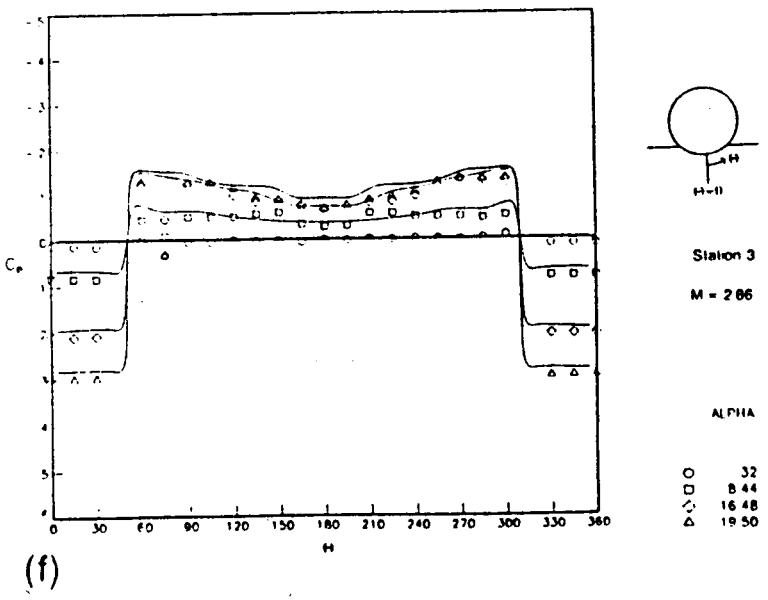

Figure 32.- Continued

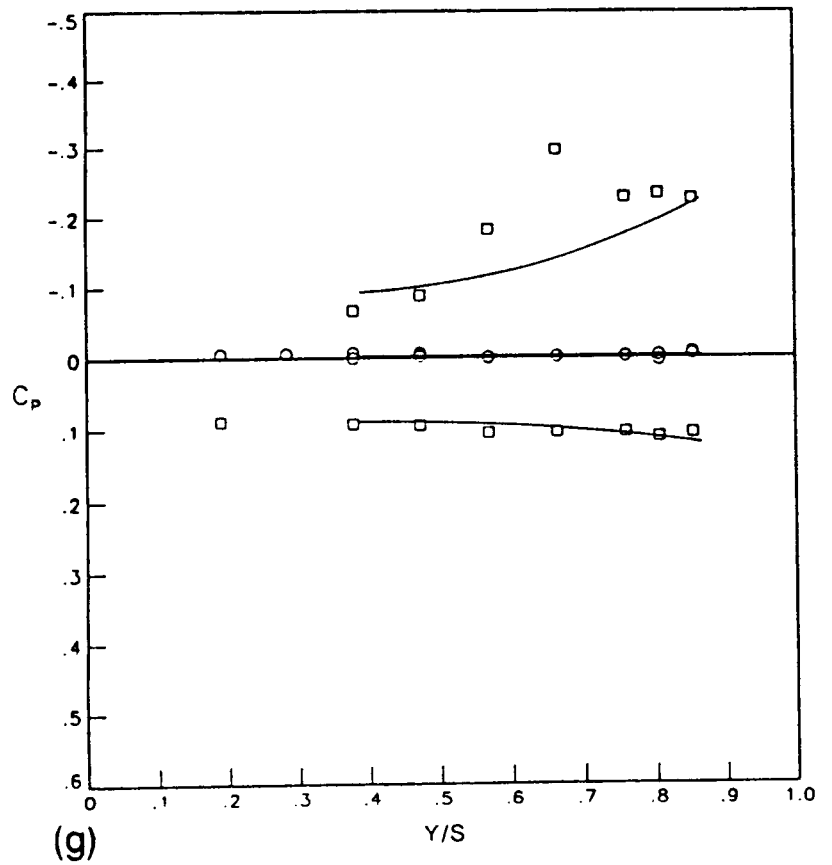

(g)

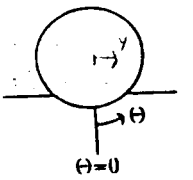

Station 3

M = 1.70

ALPHA

o .39

□ 8.44

— theory

o data

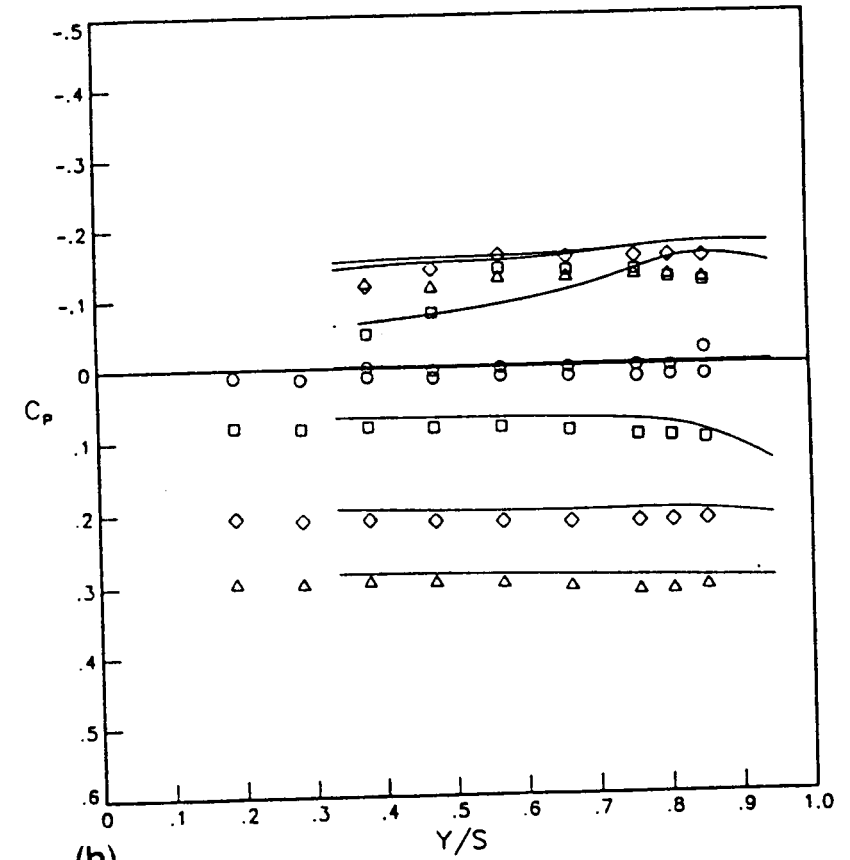

(h)

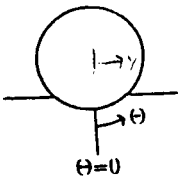

Station 3

M = 2.86

ALPHA

○ .32

□ 8.44

◇ 16.48

△ 19.50

Figure 32.- Concluded

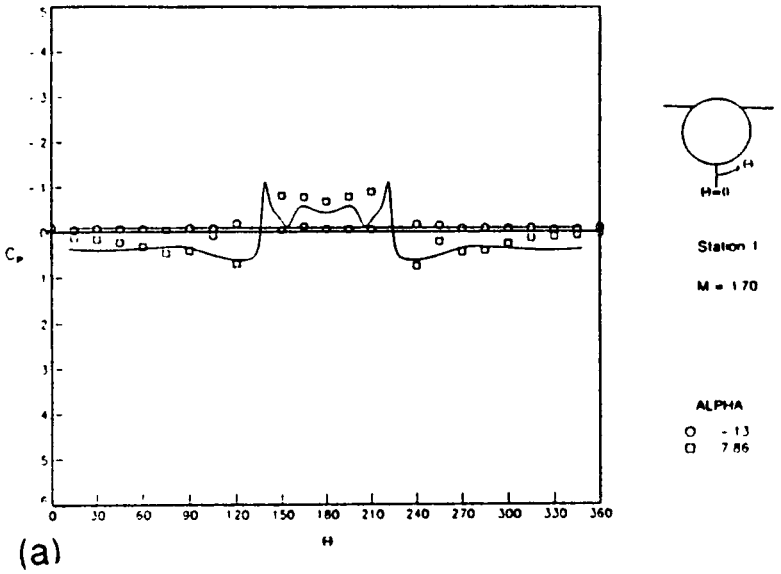

(a)

— theory
o data

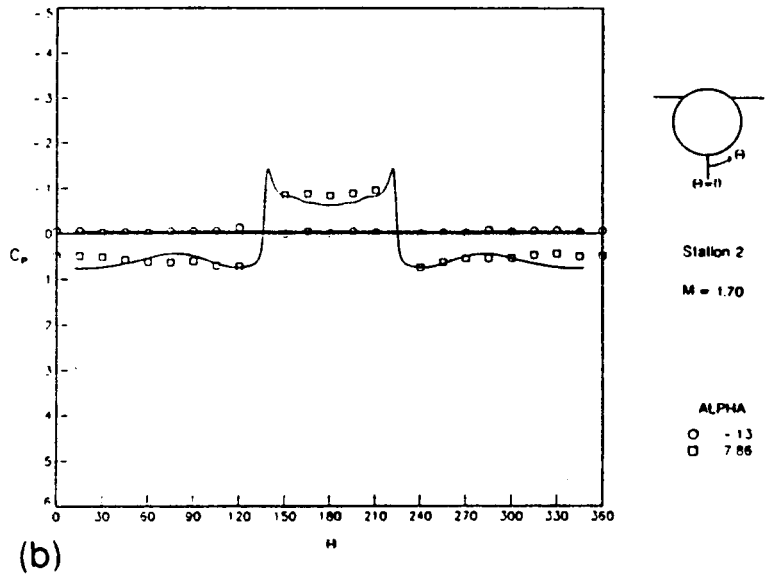

(b)

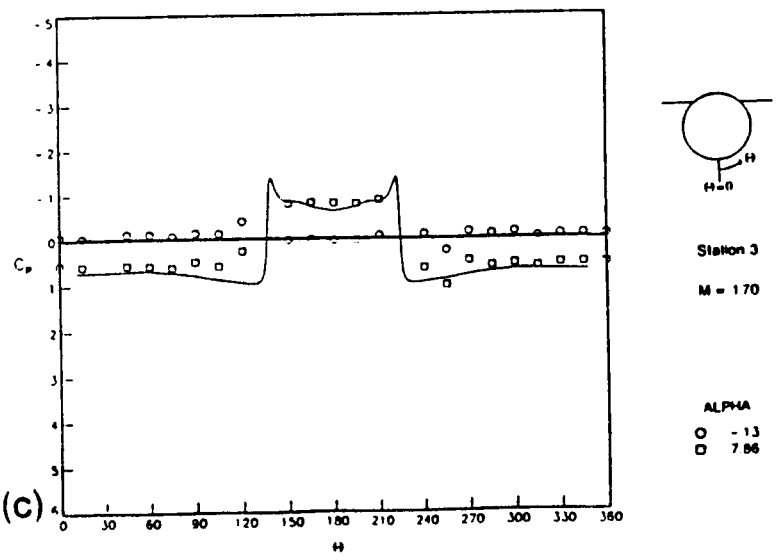

(c)

Figure 33.- Experimental/Theoretical Comparisons for Intermediate High-Wing Configuration

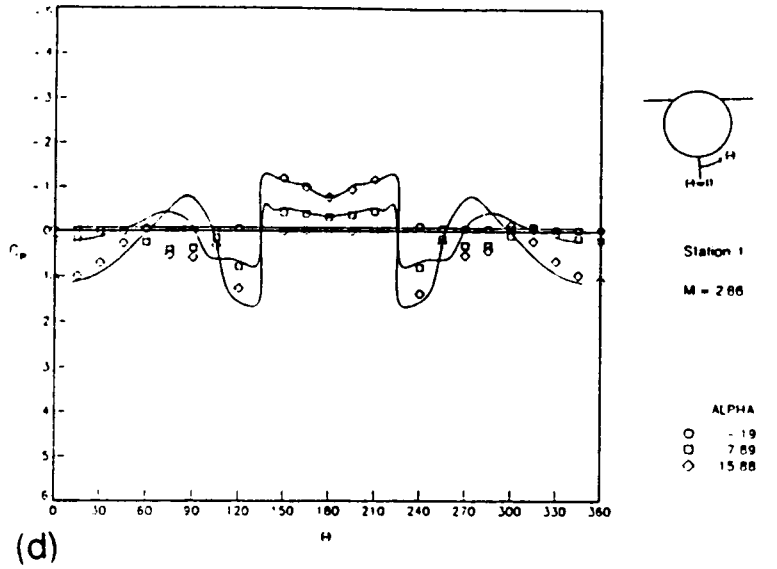

(d)

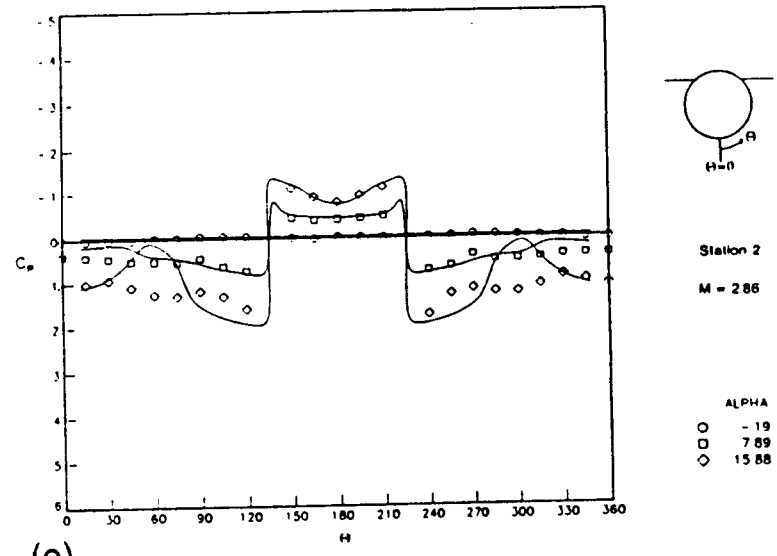

(e)

— theory
o data

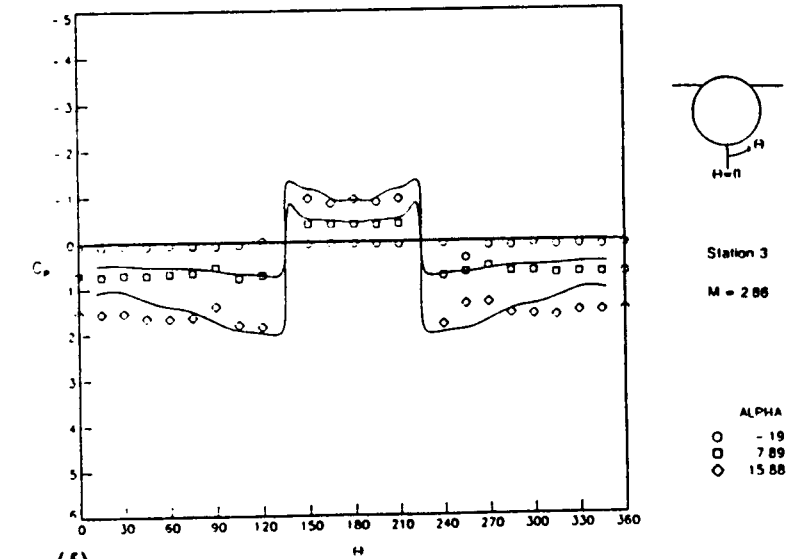

(f)

Figure 33.- Continued

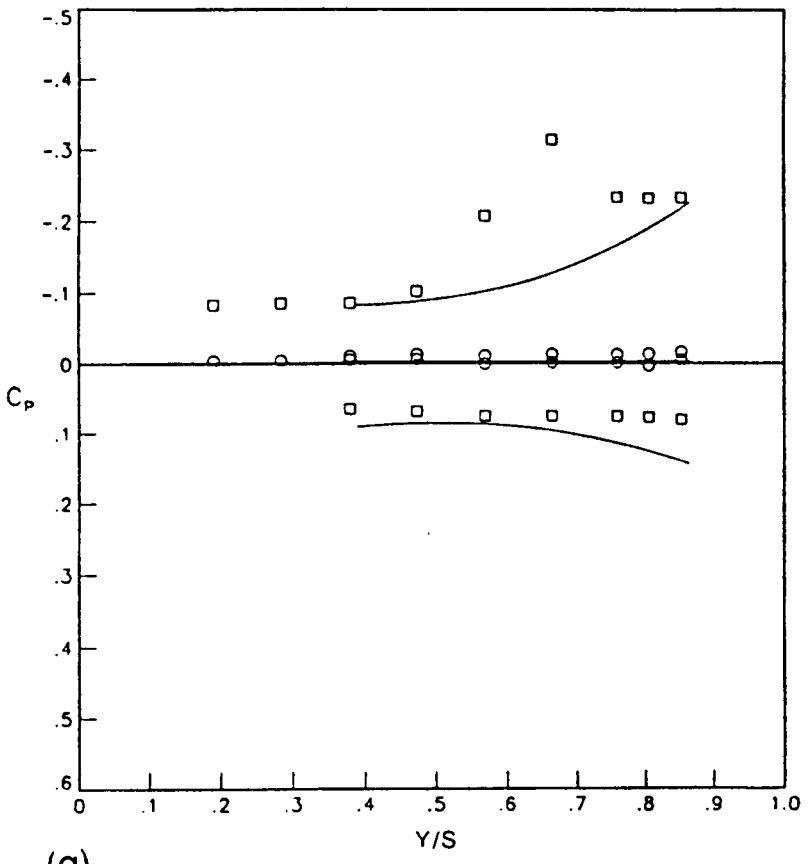

(g)

- theory
o data

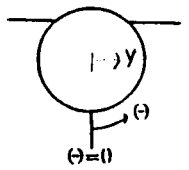

Station 3

M = 1.70

ALPHA

o -.12
□ 7.86

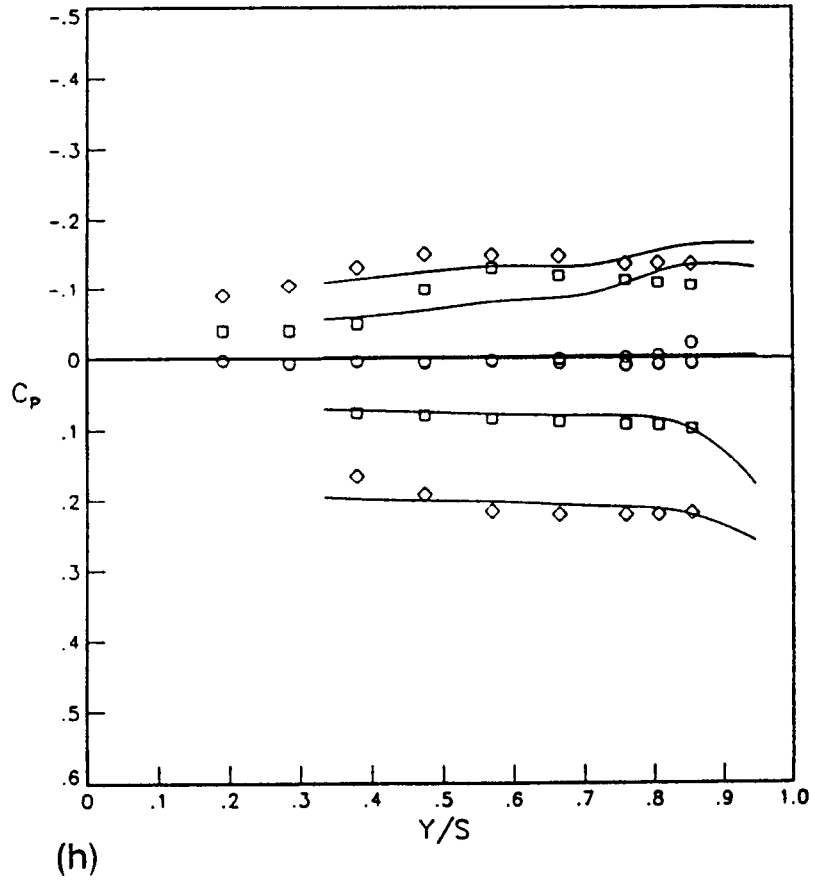

(h)

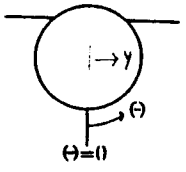

Station 3

M = 2.86

ALPHA

○ -.19
□ 7.89
◇ 15.88

Figure 33.- Concluded

Report Documentation Page

1. Report No.	2. Government Accession No.	3. Recipient's Catalog No.
NASA TM-101531		

4. Title and Subtitle	5. Report Date
Wind Tunnel Pressure Study and Euler Code Validation of a Missile Configuration with 77° Swept Delta Wings at Supersonic Speeds	November 1988
	6. Performing Organization Code
7. Author(s)	8. Performing Organization Report No.
Patsy S. Fulton	
	10. Work Unit No.
	505-61-71-01
9. Performing Organization Name and Address	11. Contract or Grant No.
NASA Langley Research Center Hampton, VA 23665-5225	
	13. Type of Report and Period Covered
12. Sponsoring Agency Name and Address	Technical Memorandum
National Aeronautics and Space Administration Washington, DC 20546	14. Sponsoring Agency Code

15. Supplementary Notes

Submitted to the School of Engineering and Applied Sciences of The George Washington University in partial fulfillment of the requirement for the degree of Master of Science.

16. Abstract

A wind-tunnel pressure study was conducted on an axisymmetric missile configuration in the Unitary Plan Wind Tunnel at NASA Langley Research Center. The Mach numbers ranged from 1.70 to 2.86 and the angles of attack ranged from -4° to 24°. The computational accuracy for limited conditions of a space-marching Euler code was assessed.

17. Key Words (Suggested by Author(s))	18. Distribution Statement
Supersonic Aerodynamics Pressure test Euler code	Unclassified-Unlimited Subject Category 02

19. Security Classif. (of this report)	20. Security Classif. (of this page)	21. No. of pages	22. Price
Unclassified	Unclassified	122	A06